

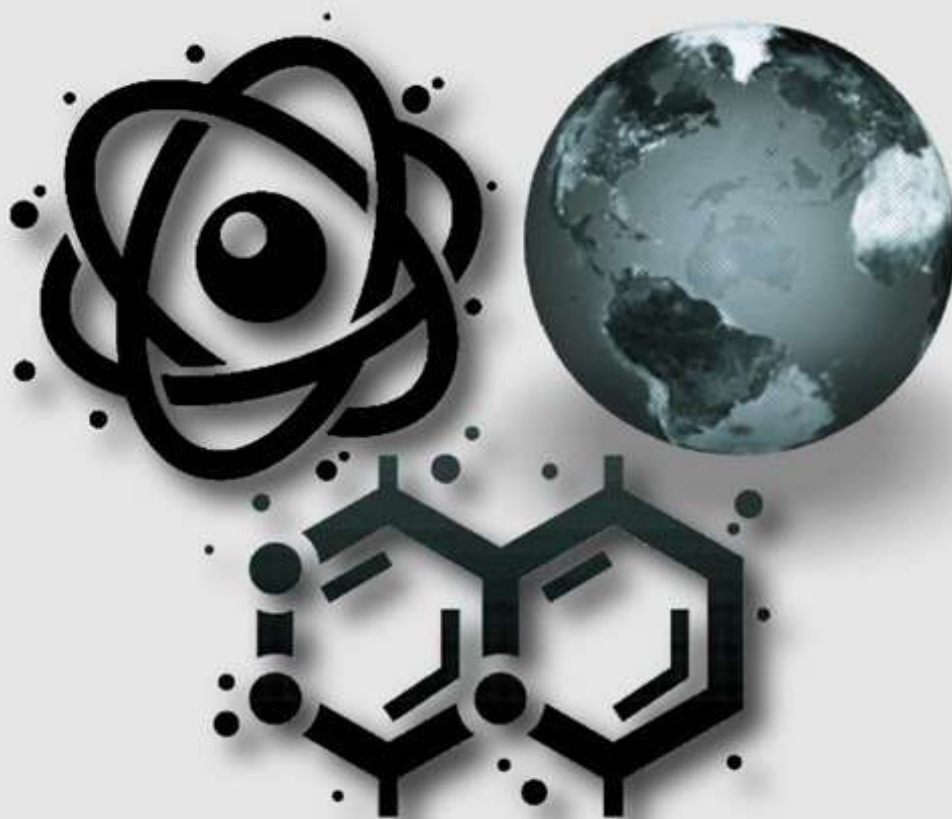
Vol. 5 No. 1 Tahun 2022

P-ISSN : 2621-0215

E-ISSN : 2621-489X

Al-Fiziya

Journal of Materials Science, Geophysics,
Instrumentation and Theoretical Physics



Published by
Program Studi Fisika
Fakultas Sains dan Teknologi
Universitas Islam Negeri Syarif Hidayatullah Jakarta

AL-FIZIYA:
Journal of Materials Science, Geophysics, Instrumentation,
and Theoretical Physics

Vol. 5, No. I, Tahun 2022

EDITORIAL IN CHIEF

Dr. Sitti Ahmiatri Saptari

MANAGING EDITOR

Muhammad Nafian, M.Si

REVIEWER

Dr. Sabar, M.Si

Duwi Hariyanto, M.Si

Rofiqul Umam, M.Si., Ph.D

Tri Wulan Sari, M.Si.

Fitri Indah Sari, Ph.D

Dr. Ahmad Zaenudin, S.Si., M.T

Dr. Rina Dwi Indriana, S.Si., M.Si

Dr. Adam Badra Cahaya

Wiji Raharjo, M.Si

Dr. Dwi Nanto, M.Si

Dr. Eng. Supriyanto, M.Si

SECTION EDITOR

Elvan Yuniarti, M.Si.

Anugrah Azhar, M.Si.

Saipudin, M.Si.

Biaunik Niski Kumila, M.Sc.

Nizar Septian, M.Si

LAYOUT EDITOR

Ryan Rizaldy, M.Si.

Alamat Redaksi

Gedung Fakultas Sains dan Teknologi Lt. 3

Jl. Ir. H Juanda No.95 Ciputat 15412 Tangerang

Telp. (6221)743731, (6221)7493315

Email: al-fiziya@uinjkt.ac.id

Published by

Program Studi Fisika, Fakultas Sains dan Teknologi
Universitas Islam Negeri Syarif Hidayatullah Jakarta

PENGANTAR REDAKSI

Assalamu'alaikum, Wr. Wb.

Puji Syukur kita panjatkan kehadiran Allah SWT, dengan terbitnya Al-Fiziya: Journal of Materials Science, Geophysics, Instrumentation, and Theoretical Physics Vol 5, No. I, Tahun 2022 dengan nomor ISSN: 2621-0215 dan E-ISSN: 2621-489X sebagai jurnal penelitian dan pengembangan ilmu fisika yang diterbitkan oleh Program Studi Fisika Fakultas Sains dan Teknologi UIN Syarif Hidayatullah Jakarta. Jurnal ini menyajikan artikel-artikel penelitian dan pengembangan terkini baik dalam Bahasa Indonesia maupun Bahasa Inggris di bidang fisika murni dan terapan, antara lain bidang fisika material, geofisika, fisika instrumentasi, dan fisika teori. Jurnal ini merupakan sarana publikasi bagi dosen dan para peneliti yang bergerak di bidang penelitian dan pengembangan ilmu fisika. Dengan demikian, melalui penerbitan jurnal ini kami memberikan kesempatan seluas-luasnya bagi siapapun yang ingi berpartisipasi dalam menyampaikan buah pikirannya melalui tulisan atau artikel yang akan kami muat pada edisi berikutnya.

Artikel yang masuk akan melalui proses seleksi oleh dewan editor dan *review* yang melibatkan mitra bestari baik dari para dosen ahli dibidangnya berdasarkan kesesuaian isi dan bobot karya ilmiah. Untuk informasi lengkap submit dan tata cara penulisan dalam Al-Fiziya: *Journal of Material Science, Geophysics, Instrumentation, and heoretical Physics* dapat dilihat pada pedoman penulisan artikel di halaman akhir penerbitan atau dapat mengakses website kami di <http://journal.uinjkt.ac.id/index.php/al-fiziya>. Atas nama dewan redaksi, kami mengucapkan terimakasih atas dukungan dan partisipasi dari semua pihak hingga terbitnya Al-Fiziya: *Journal of Materials Science, Geophysics, Instrumentation, and Theoretical Physics*.

Editorial in chief
SITTI AHMIATRI SAPTARI

Daftar Isi

Vol. 5, No. 1 Tahun 2022

Pengantar Redaksi	i
Daftar Isi	ii
Muhamad Fauzan Zarkashie, Elvan Yuniarti, Ryan Rizaldy. Portable Water Quality Measurement System for Sanitation	1 – 9
Nanda Ridki Permana, Belista Gunawan. Analysis of Subsurface Structure of Sembalun Geothermal Prospect Area, East Lombok with 2D and 3D Gravity Modeling.....	10 – 22
Rizal Indrawan. Effect of Temperature and Heating Resistant Time on Wear Properties of Molybdenum/Alumina Composites	23 – 32
Putri Sekar AyuNingsih, Sutrisno, Tati Zera, Egie Wijaksono Identification of Characteristics and Distribution of Subsurface Coal Using the 2D Geoelectric Method in Tanjung Palas Timur District, North Kalimantan	33 – 45
Salsabila Octara Sumaryanto, Nur Hidayat. Identification of Potential Waste Fluid Contamination with Geoelectric Method in Tebing Tinggi Subdistrict, West Tanjung Jabung Regency, Jambi	46 – 55
Wakid Ali Muntoha, Adam B. Cahaya, Azwar Manaf. Correlation between Scattering Matrix, Return Loss and Interface Reflection Loss in Nicolson Rose Wear Approximation	56 – 62
Eka Nurajanah Wulandar, Moh Iqbal Tawakal. Study Of Soil Vulnerability In East Java Using Horizontal And Vertical Spectrum Ratio (Hvsr) Method From Ambient Noise Waves	63 – 71
Praditiyo Riyadi, Arkanu Andaru. Evaluation Of Coal Distribution For Alternative Energy Using Seismic Spectral Decomposition	72 - 77

Portable Water Quality Measurement System for Sanitation

Muhamad Fauzan Zarkashie¹, Ryan Rizaldy¹, Elvan Yuniarti^{1,†}

¹Program Studi Fisika, Fakultas Sains dan Teknologi, Universitas Islam Negeri Syarif Hidayatullah Jakarta, Jalan. Ir. H. Djuanda No.95, Cempaka Putih, Ciputat, Kota Tangerang Selatan, Banten 15412, Indonesia

†elvan.yuniarti@uinjkt.ac.id

Submitted: February 2022; Revised: August 2022; Approved: September 2022; Available Online: October 2022

Abstract. Water is one of the essential needs that play an essential role in supporting life on earth. Water for sanitary hygiene purposes is used for several things to maintain individual hygiene, such as bathing and toothbrushes. Water is also for washing foodstuffs, tableware, and washing clothes. In addition, water for hygiene sanitation can be used as raw water for drinking water. This research designs a water quality measurement tool using parameters following water quality for sanitary hygiene purposes issued by the Ministry of Health. These parameters include turbidity, acidity (pH), temperature, and solids in water. The tool is designed to use Arduino Uno as a controller, sensors according to the parameters of photodiode sensors, pH, temperature, TDS (Total Dissolved Solids), and output systems using an LCD 20 × 4. This study concluded that the water quality detection system is running well, using photodiode sensors that can read each level of turbidity based on the value of ADC (Analog Digital Converter). The TDS sensor has an accuracy rate of 93.2% with a 6.8% error percentage. The pH sensor has an occurrence rate of 97.5% with a 2.5% error percentage, and a temperature sensor has an accuracy of 97.84% with a 2.16% error percentage.

Keywords: *Arduino Uno, Photodiode Sensor, pH sensor, Temperature Sensor, TDS Sensor.*

DOI : [10.15408/fiziya.v5i1.24708](https://doi.org/10.15408/fiziya.v5i1.24708)

INTRODUCTION

Water is one of the most important basic needs in living things on earth. Water is used for metabolic processes by living beings. In humans, the function of water is a necessity for industry, agriculture, transportation, and much more. There are three sources of water on this earth, namely groundwater, surface water, and rainwater. Groundwater is water that is in the soil layer at different depths. Humans usually use groundwater for life needs, for example, obtained through wells or water pumps [1]. The physical condition of clean water must be clear, odorless, and tasteless [2] in the Regulation of the Minister of Health of the Republic of Indonesia number 32 of 2017 Chapter II on the standard of environmental health quality standards for sanitary hygiene purposes. Environmental health quality standards for sanitation hygiene water include several physicals, biological and chemical parameters [3].

Murky water is a characteristic of unhealthy water. Turbidity is an optical property determined by light absorbed and emitted by the solution contained in water. Water can be said to be cloudy when the water has a particle charge of suspended material, thus sharing a muddy and dirty color or appearance. The materials that cause this turbidity include clay, mud, fine sand, and organic materials [5].

Acidity or pH of water is also very influential for our metabolism because if the water we consume to drink and processed foods have a low pH, the needs in our body don't meet to the maximum. Good water for consumption following the Regulation of the Minister of Health of the Republic of Indonesia Number 32 of 2017 has a pH value of 6.5 – 8.5. As for the water, the temperature should be cold (not hot), primarily so as not to occur dissolving chemicals can harm health. The temperature parameter for sanitary hygiene water is the air temperature ± 3 [3].

Total Dissolved Solids, often abbreviated to TDS, measure dissolved organic and non-organic, e.g., salts and the like contained in water, ionized or in the form of micro granules (collide soles) are trapped. TDS is used to guide water characteristics and as an aggregate parameter of the comprehensive measurement of chemical pollution [6]. The high value of solids or TDS is one of the considerations in determining water quality for use in households. Parameters in TDS measurement provided that the result does not exceed 1,000 mg/l [3]. In previous studies, a water quality detection device has been developed with three parameters, namely PH, TDS, and Water Temperature [4]. In this study, there are differences from the previous tool has four parameters, namely turbidity, PH, TDS, and water temperature. This article describes its application to several water sources in rivers. This tool can determine the quality of water for household needs

RESEARCH METHODOLOGY

Research Equipment

The equipment in this study used two types of devices, namely hardware, and software. Components and tools used in hardware include Silicon Photodiode Sensor [7][8][9], PH-4502C pH Sensor [10][11], Gravity Sensor TDS [14][15], DS18B20 Temperature Sensor [12][13], Arduino Shield Sensor, Arduino Uno, 4.7k resistor Ω , male-female cable, Project Board, Glass Cuvette, Liquid Crystal Display (LCD) 20 × 4, Laptop, Push Button and Plastic Box. While the software used is IDE Arduino and Fritzing. At the same time, the tool for calibration uses tools from the factory, such as TDS-3 and PH 009(I) A.

Stages and Flow of Research

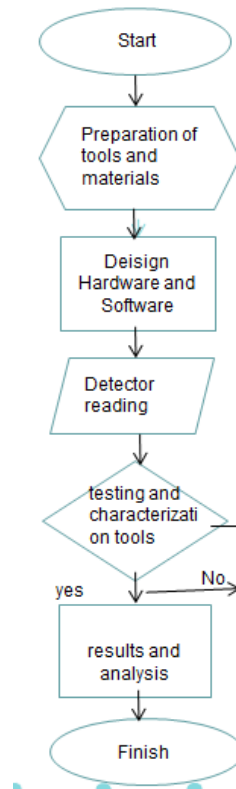


Figure 1 Stages and Flow of Research.

The hardware design of each water quality measuring instrument for sanitary hygiene purposes, each sensor is connected to the Arduino Uno control system. For turbidity measurement, added blue LED components can be seen in figure 2 Hardware Design.

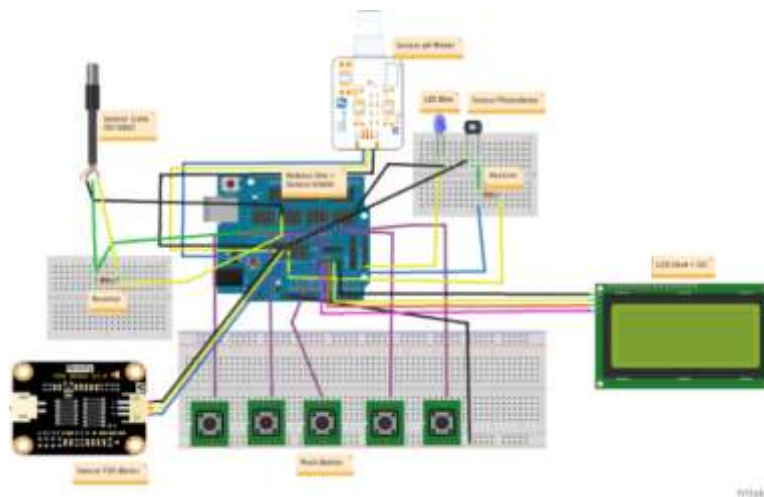


Figure 2 Hardware Design.

In Figure 2 of the Hardware Design, five pushbuttons are pressed to create a menu section inside the program displayed to the LCD output. Furthermore, use the Arduino shield sensor to reduce jumper cables on the circuit. Arduino IDE is the software

used for water quality measuring equipment for hygiene sanitation purposes. Arduino receives readings from Photodiode sensors, pH sensors, DS18B20 temperature sensors, and TDS sensors. Therefore Arduino must be filled with a program in the form of source code, then Arduino will process the reading results and output the results on the LCD 20×4 .

Data Retrieval

The data retrieval method is obtained by conducting two stages of testing, among others, sensor calibration testing by calibrating the tool with the factory output tool, then each sensor is set in the Arduino IDE for voltage output. After getting linear regression to go into the second stage. The second stage is testing the accuracy of each sensor with several sample options for each sensor.

Data Processing

The data obtained will be processed using the linear regression method, standard deviation, and percentage error value. The following are linear regression formulas and deviation standards:

$$\text{Linear Regression Formula is } y = bx + a \quad (1)$$

$$s = \sqrt{\frac{n\sum_{i=1}^n x_1^2 - (\sum_{i=1}^n x_1)^2}{n(n-1)}} \quad (2)$$

The formula of the percentage error value of the sanitary hygiene water quality measuring instrument is:

$$\% \text{ error} = \frac{| \text{test value} - \text{theoretical value} |}{\text{theoretical value}} \times 100 \quad (3)$$

River water data collection method

River water samples were taken from 6 different places. Three water samples were taken for each place. Each water sample contains 100 ml. Water sample testing carried out in the form of turbidity, TDS, PH and temperature.

In this study, testing was carried out in accordance with SNI 06-6989.11-2004. This method includes, how to test the degree of acidity (Ph) of water and wastewater using a pH meter. In addition, referring to SNI 06-6989.23-2005 the test is used to determine the temperature of water and wastewater using a mercury thermometer compared to the tool made.

RESULTS AND DISCUSSION

In designing sanitary hygiene water quality measuring instruments, researchers conducted two design stages, namely hardware and software. The following are the results of hardware and software design:



Figure 3 Design results (a) Outer view and (b) Inward view.

The results of hardware design in this study include the design of water quality measuring instruments for sanitary hygiene purposes using four parameters: turbidity, pH, TDS, and temperature. The output of each parameter is the turbidity shown by the division of levels in the Analog to Digital Converter (ADC) value that converts analog inputs into digital codes [16], for acidity or pH, the output value is pH, the output on the TDS is ppm, and the output for the temperature is °C. The value in the output successfully performs the software design by entering the source code by the Arduino IDE.



Figure 4 Output results on LCD.

Data Processing and Results

Accuracy testing is performed on several test samples at different levels of each parameter unit. Moreover, there are six samples from different locations for the tool test as a whole. Sensor accuracy testing compares factory output gauges with designed gauges controlled by Arduino Uno.

Table 1 Data processing to determine the level of turbidity in photodiode sensors

No	Turbidity Level	ADC Value
1	Clear	>155
2	A Little Murky	>120
3	Quite Murky	>90
4	Murky	>50
5	Very Murky	>5

In Table 1 of Data processing to determine the level of turbidity on photodiode sensors, the level of turbidity for clear is obtained if the ADC value is more than 155, for

a slightly cloudy if the ADC value is more than 120, for somewhat murky ADC values over 90, for murky ADC values over 50 and for very murky ADC values over 5.

Table 2 Processing of comparative value data between pH sensor and factory pH meter.

No.	Materials	Time Duration (minutes)	Average Sensors PH-4502C (pH)	PH-009(I)A (pH)	Standard Deviation	Percentage Error (%)
1	phosphoric acid	± 3	2.08	2.10	0.021	0.90
2	phosphoric acid	± 3	2.70	2.80	0.007	3.50
3	phosphoric acid	± 3	3.93	4.00	0.013	1.75
4	phosphoric acid	± 3	6.25	6.50	0.027	3.80
5	NaOH	± 3	7.53	7.80	0.011	3.40
6	NaOH	± 3	9.65	9.80	0.022	1.50
7	NaOH	± 3	10.10	10.40	0.176	2.70
8	NaOH	± 3	11.20	11.50	0.187	2.60
Average Standard Deviation					0.058	
Average Percentage Error					2.500	
Accuracy (100 % - Percentage Error)					97.500	

In processing pH sensor data, first, to determine the type of sample for the test, the sensor measurement is then carried out starting with an acid solution and then to the base and taken measurement using pH meter afterward. The results of the eight measurements of phosphoric acid and NaOH liquids, both of which were added, obtained an average percentage of errors of 2.5% and the accuracy value of the tool 97.5%. The standard deviation average is 0.058, as shown in Table 2 of the data processing of the comparison value between the pH sensor and the factory meter pH. This percentage of errors is caused by sensor sensitivity, reference pH, and ADC conversion.

Table 3 Data processing value comparison between TDS sensor with the factory TDS meter.

No.	Time Duration (seconds)	Average Sensors Gravity TDS (ppm)	TDS-3 (ppm)	Standard Deviation	Percentage Error (%)
1	± 5	0.00	0	0.00	0.00
2	± 5	16.40	18	2.30	8.80
3	± 5	21.40	24	2.07	10.80
4	± 5	30.80	34	1.60	9.40
5	± 5	39.20	45	1.30	12.80
6	± 5	43.40	49	2.90	11.40
7	± 5	69.20	72	0.44	3.80
8	± 5	140.20	146	0.44	3.90
9	± 5	206.40	208	0.54	0.70
Average Standard Deviation					1.3
Average Percentage Error					6.8
Accuracy (100 % - Percentage Error)					93.2

In processing TDS sensor data, first, to determine the type of sample for the test, the subsequent measurement of the TDS meter begins with mineral water coupled with kitchen vinegar. Furthermore, measurements are performed using the TDS sensor afterward. The eight measurements of mineral water liquid added with kitchen vinegar obtained an average percentage of errors of 6.8% and the accuracy value of the tool 93.2%. The standard deviation average is 1,303, as shown in table 3 data processing of the comparative value between the TDS sensor and the factory meter TDS. This percentage of errors is caused by sensor sensitivity, reference TDS meter, mineral location in water, and ADC conversion.

Table 4 Processing of comparative value data between the Temperature sensor and factory meter temperature

No.	Time Duration (seconds)	Average Sensors DS18B20 (temperature °C)	TDS-3 (temperature °C)	Standard Deviation	Percentage Error (%)
1	± 15	26.60	28	1.10	5.50
2	± 15	36.40	36	0.90	1.10
3	± 15	53.80	54	1.30	0.30
4	± 15	62.20	62	0.83	0.30
5	± 15	23.20	23	1.30	0.80
6	± 15	20.60	22	1.50	6.30
7	± 15	18.20	18	1.30	1.10
8	± 15	30.40	31	1.10	1.90
Average Standard Deviation				1.10	
Average Percentage Error				2.16	
Accuracy (100 % - Percentage Error)				97.84	

In the calibration test process of the temperature sensor, first to determine the type of sample for the test, then conducted temperature measurement with TDS meter starting with cold water, regular water, and hot water. Furthermore, measurements are performed using the temperature sensor afterward. The eight measurements obtained an average error percentage of 2.16% and a tool accuracy value of 97.84%. The average standard deviation is 1.1. This error percentage is caused by sensor sensitivity, reference meter TDS, probe position in the water, and ADC conversion.

Table 5 Overall test of tools with multiple locations

Location	Turbidity	TDS (ppm)	pH	Temperature (°C)
Jonggol, West Java	Clear	110	6.63	25.56
Cimande, West Java	Clear	47	7.41	25.25
Cikarang, Jababeka I	Clear	163	6.33	25.50
Cikarang, Jababeka II	Clear	134	6.45	25.69
Cimande River, West Java	Quite Murky	43	6.37	25.25
Chemical Plant Waste, Cikarang	Murky	348	5.95	25.31

The overall test results of the tool were obtained that the tool has worked in measuring the TDS, turbidity, pH, and temperature of various test samples. Measurement results in six locations showed TDS ranged from 43 ppm to 348 ppm, with all locations meeting the TDS parameter that does not exceed 1000 ppm. Location turbidity

measurement results in 5 and 6 are not eligible with parameters created using Analog-Digital Converter (ADC). The pH measurement results are only locations 1 and 2 that meet the 6.5 pH – 8.5 pH standard. Moreover, all locations meet the standard of clean water parameters for the temperature measurement results, i.e., air temperature ± 3 °C [3].

CONCLUSION

The Measurement System of Turbidity, Acidity Level (pH), Temperature, and number of Dissolved Solids in Water using a photodiode sensor, Analog pH Sensor PH-4502C, Temperature Sensor DS18B20 Waterproof and Gravity Analog TDS Sensor SKU: SEN0244 was successfully designed and built. The accuracy and calibration of each sensor showed the TDS sensor has an accuracy rate of 93.2% with a 6.8% error percentage, the pH sensor has an acceptance rate of 97.5% with a 2.5% error percentage, and a temperature sensor has an accuracy of 97.84% with a 2.16% error percentage. The test carried out proved that this tool has worked in measuring TDS, turbidity, pH, and temperature. Measurement results in six locations showed TDS ranged from 43 ppm to 348 ppm, with all locations meeting TDS parameters not exceeding 1000 ppm. Location turbidity measurement results in 5 and 6 are not eligible with parameters.

REFERENCE

- [1] A. Renaldo, "Analisis Kualitas Air Pemandian Di Desa Ulak Bandung Kecamatan Muara Sahung Kabupaten Kaur Provinsi Bengkulu," UIN Raden Intan Lampung, 2019.
- [2] R. I. Depker, "Peraturan Menteri Kesehatan RI No 416/Menkes," *Per/IX/1990, Jakarta*, 1990.
- [3] Menteri Kesehatan Republik Indonesia, "Peraturan Menteri Kesehatan Republik Indonesia Nomor 32 Tahun 2017 Tentang Standar Baku Mutu Kesehatan Lingkungan Dan Persyaratan Kesehatan Air Untuk Keperluan Higiene Sanitasi, Kolam Renang, Solus Per Aqua dan Pemandian Umum," *Peratur. Menteri Kesehat. Republik Indones.*, pp. 1–20, 2017.
- [4] Novempa, N. N. et al. (2020) 'Alat Pendeteksi Kualitas air Portable dengan parameter, pH , TDS', 09, pp. 85–92. [5] M. Kautsar, R. R. Isnanto, and E. D. Widiyanto, "Sistem Monitoring Digital Penggunaan dan Kualitas Kekeruhan Air PDAM Berbasis Mikrokontroler ATmega328 Menggunakan Sensor Aliran Air dan Sensor Fotodiode," *J. Teknol. dan Sist. Komput.*, vol. 3, no. 1, pp. 79–86, 2016, doi: 10.14710/JTSISKOM.3.1.2015.79-86.
- [6] T. T. Pairunan, O. Mellolo, and L. Nathaniel, "Desain Sistim Monitoring Jumlah Zat Padat Terlarut Dalam Limbah Cairan Industri Tepung Kelapa Provinsi Sulawesi utara," pp. 64–70, 2019.
- [7] S. Supatmi, "Dioda," 2010.
- [8] Y. P. Pratama, "Aplikasi Sensor Photodiode Sebagai Input Penggerak Motor Pada Coconut Milk Auto Machine." Politeknik Negeri Sriwijaya, 2015.
- [9] M. A. Katra Trisandi, "Rancang Bangun Sistem Parkir Valet otomatis Menggunakan Robot line Follower." universitas islam negri alauddin makassar, 2018.
- [10] G. A. Putera and D. Christian, "Perancangan Alat Ukur Kadar Padatan Terlarut, Kekeruhan dan pH Air Menggunakan Arduino Uno," *Skripsi Dep. Tek. Elektro Fak. Tek. Unhas*, 2017.
- [11] Z. B. Hasanuddin et al., "Perancangan pengukuran kadar kepadatan terlarut, kekeruhan dan ph air dengan menggunakan arduino," vol. 4, no. November, pp. 5–9, 2018.
- [12] F. Ramdani, "Perancangan Sistem Magnetik Stirrer Berbasis Android." Universitas Komputer Indonesia, 2018.
- [13] S. Alam, A. Alauddin, M. A. Kadir, and E. Elihami, "Sistem Otomatis Sirkulasi Udara Pada Tambak Udang," *Jutkel J. Telekomun. Kendali dan List.*, vol. 2, no. 1, pp. 1–10, 2020.

- [14] M. Martani and E. Endarko, "Perancangan dan Pembuatan Sensor TDS Pada Proses Pengendapan CaCO_3 Dalam Air Dengan Metode Pelucutan Elektron dan Medan Magnet," *Berk. Fis.*, vol. 17, no. 3, pp. 99–108.
- [15] A. Saputra, S. T. Umifadlilah, and M. Eng, "Pengukur Kadar Keasaman dan Kekeruhan Air Berbasis Arduino." Universitas Muhammadiyah Surakarta, 2016.
- [16] F. W. Kurniyanto and N. F. Madina, "Purwarupa KWH Meter Digital yang dilengkapi Data Logger sebagai Alat Bantu melakukan Audit Energi." Institut Technology Sepuluh Nopember, 2015.

Analysis of Subsurface Structure of Sembalun Geothermal Prospect Area, East Lombok with 2D and 3D Gravity Modeling

Nanda Ridki Permana¹, Belista Gunawan², Muhammad Nafian^{2,†}

¹PT. Minelog Service Indonesia, Industrial Area, BSD Serpong, South Tangerang City, Indonesia

²Physics Study Program, Faculty of Science and Technology, Syarif Hidayatullah State Islamic University Jakarta, Jalan. Ir. H. Djuanda No.95, Cempaka Putih, Ciputat, South Tangerang City, Banten 15412, Indonesia

[†]muhammad.nafian@uinjkt.ac.id

Submitted: February 2022; Revised: April 2022; Approved: August 2022; Available Online: October 2022

Abstract. The existence of Indonesian geothermal is estimated to be spread in 331 locations, one of which is Sembalun, East Lombok Regency. Therefore, this study was conducted to analyze the subsurface structure of geothermal prospect areas in the area using gravity methods. Gravity data used is satellite data as much as 4275 measurement points that have been corrected free air (FAA). The data processing stage resulted in a Complete Bouguer Anomaly (CBA) map with low anomaly values to be the target of research ranging from 58.9 – 115.7 mGal located in the east (Sembalun-Bumbung) and northeast (Sembalun-Lawang). The prospect of geothermal is controlled by Talaga fault and Pusuk fault on the caldera floor (Sembalun-Lawang). In addition, the Tanakiabang fault and the Orok fault are near the manifestation of Sebau Hot Springs and on the Caldera floor (Sembalun Bumbung). The results of 2D modeling correlated with 3D modeling conducted inversions showed geothermal sources are estimated to have a density of 2.68 gr/cc – 3 gr/cc consisting of hornblende andesite lava rocks with a depth of >2500, reservoir layer in the form of sand that has a density of 1.4 gr/cc - 1.72 gr/cc with a depth of 700 - 1200 m and a layer of hood in the form of alluvium rocks that have a density of 1.8 gr/cc - 2.2 gr/cc with a depth of 0 - 500 m.
Keywords: *gravity method, inversion method, geothermal.*

DOI : [10.15408/fiziya.v5i1.24943](https://doi.org/10.15408/fiziya.v5i1.24943)

INTRODUCTION

Indonesia is one of the three countries with the largest geothermal potential in the world. The existence of geothermal based on data from the Ministry of Energy and Mineral Resources in 2017 is found at 331 locations. The locations are scattered along volcanic paths ranging from Sumatra, Java, Bali, Nusa Tenggara and then veering to Maluku and Sulawesi. Geothermal sources in Indonesia are mostly produced from high and medium-temperature geothermal systems. The system is very suitable to be used as a source of power generation. The potential electricity generated for all these points is 28,579 MWe or equivalent to 14.47 % of all geothermal potential in the world. While its utilization has only reached 1,698.5 MW or about 5.94% of the potential nasional [1].

Sembalun Geothermal Prospects

West Nusa Tenggara becomes a volcanic path of geothermal resources with one of its location points is in Sembalun, East Lombok Regency. East Lombok regency is a regency located at the eastern end of Lombok Island. Geographically the district is located between 8° LS – 9° LS and 116° BT – 117° BT with an area of $2,679.88 \text{ km}^2$ consisting of $1,605.55 \text{ km}^2$ landmasses and $1,074.33 \text{ km}^2$ oceans [2].

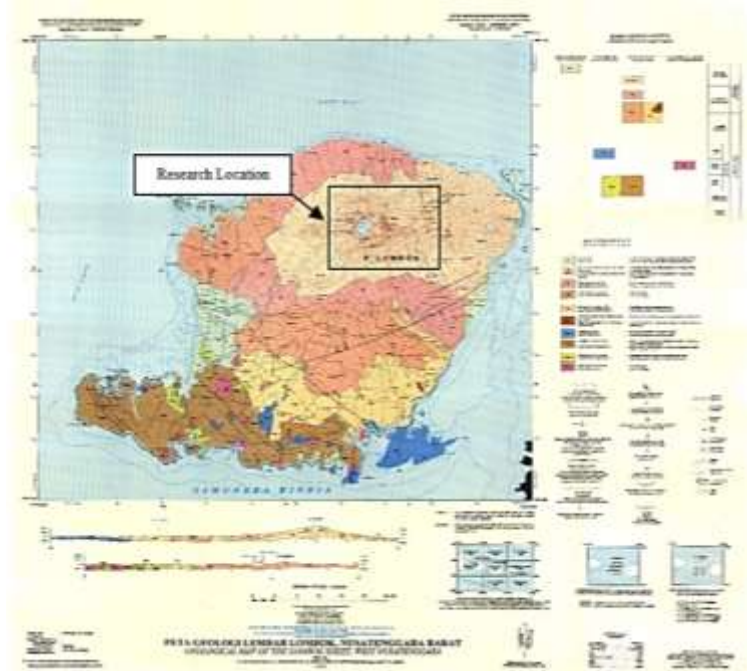


Figure 1. Geological Map of Lembar Lombok, West Nusa Tenggara [3].

In East Lombok area, there are several units of late Pleistocene to quarter volcano rocks composed by volcanic breccias, including Kalipalung formation, Kalibabak Formation, and Lekopiko Formation. Kalipalung Formation (TQp) consists of breccias gampingan and lava, Kalibabak Formation (TQb) consists of breccias and lava, while Lekopiko Formation (Qvl) consists of rocky tuf, lava breccias, and lava [4].

Sembalun area, East Lombok Regency located in the path of volcano is one of the areas that indicates the potential of geothermal with some symptoms of manifestations on the surface. The previous reference stated that in Sebau area there is an indication of geothermal potential in the form of hot springs and gas supply with a temperature of 36.50°C dengan pH of 8.4 [5]. This manifestation is due to the research area located in the northeast at the foot of Mount Rinjani which is the second highest active mountain in Indonesia.

Previous research on the investigation of geothermal areas Sembalun, East Lombok Regency, West Nusa Tenggara has been conducted by the Geological Resource Center in 2007 using geoelectric methods, and geomagnetic methods in the Proceedings International Conference on Science and Technology (ICST) in 2020. To find out more accurate information, therefore this study was conducted with the aim to analyze the subsurface structure of the geothermal prospect area of Sembalun, East Lombok using gravity methods.

Gravity Method

Gravity method is one of the geophysical methods that application by measuring the gravitational field and utilizing variations in density values that have been distributed below the earth's surface. Gravity methods are used in regional characterization of the earth, determining the structure of the Earth's crust, and identifying regions or regions for resource exploration [6].

The higher gravitational anomaly value of the surrounding area indicates a higher density as well. The method of gravity works based on Newton's Law of Gravity which states that the force working between two m-mass objects separated at a distance of r will be directly proportional to the multiplication of the mass of the two objects and inversely proportional to the squared distance of the two centers of mass of the object [7].

$$F = G \frac{M m}{r^2} \quad (1)$$

where F is the gravitational force (N), G is the universal gravitational constant ($6,672 \times 10^{-11} \text{ Nm}^2/\text{kg}^2$), M is the mass of particles or objects (kg), m is the mass of particles or objects (kg), and r is the distance between the two centers of mass (m).

The method of gravity is processed to produce the Complete Bouguer Anomaly (CBA) value, the gravitational anomaly data obtained from the satellite is the corrected gravitational anomaly data to free air correction (FAA), so that the correction required is only terrain correction and Bouguer correction that aims to reduce the mass of rocks in the Earth's crust that are between the spheroid plane and the measurement point.

Terrain Correction is performed due to irregular topographic conditions around the measuring point. Measurements in hilly areas will result in a different measuring value to measurements made in flat areas. The influence of topography with elevation differences such as data surfaces or valleys from the surroundings can be eliminated by terrain correction[8]. Field correction can be formulated as follows:

$$TC = \frac{2\pi G\rho}{n} (r_L - r_D) + (\sqrt{r_L^2 z^2}) - (\sqrt{r_D^2 z^2}) \text{ mGal} \quad (2)$$

where r_L and r_D are the outer radius and inner radius of the compartment, z is the difference in the average elevation of the compartment, and n is the number of segments in the zone.

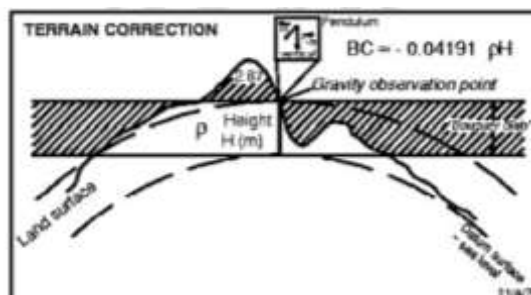


Figure 2. Correction of The Field against Gravity [8].

While Bouguer correction is taken into account because there is a pull effect of the rock mass located in the station and datum plane assuming it has infinite radius with

h (meter) thickness and density of ρ (gr/cc). Bouguer's correction value can be searched by equation [9]:

$$BC = 2\pi g \rho h \quad (3)$$

Inversion Modeling

Inversion modeling is often said to be the "opposite" of forward modeling because in inversion modeling is obtained directly from the data. Menke (1984) defines inversion theory as a whole of mathematical and statistical techniques or methods to obtain useful information about a physical system based on observations of the system. The physics system in question is a phenomenon that we review, the observation of the system is data while the information that wants to be obtained from the data is the model or parameters of the model [10].

In the process of inversion is usually done analysis of field data by matching curves (curve fittings) between field data and mathematical models. The purpose of the inversion method is to estimate the physic parameters of subsurface conditions that were not previously known. Inversion modeling techniques for gravitational anomaly data have been widely performed both against the corrected primary data of Earth's gravitational anomalies as well as to regional and residual gravitational anomaly data as well as complete Bouguer anomalous secondary data [11]. This is why this study used inversion methods to model it.

RESEARCH METHODS

The research location in the geothermal area of Sembalun is within the area of Suela and Aikmal Subdistricts, East Lombok Regency, West Nusa Tenggara Province. Located at coordinates between $116^{\circ} 30' 00'' - 116^{\circ} 35' 00''$ BT and $8^{\circ} 20' 30'' - 8^{\circ} 30' 00''$ LS (Figure 3). [12] The study, conducted on 1–6 July 2021, used gravity methods to analyze the subsurface structure of the geothermal prospect area.



Figure 3. Research Area Map.

The gravitational data used is satellite data from TOPEX as many as 4275 measurement points that have been corrected free air (FAA). Software used to support

the data processing stage include: Ms. Excel, Notepad, Google Earth Pro, Global Mapper, Surfer, Oasis Montaj, Voxler, Bloxer, ZondGM2D, and Grablox. From the ten software produced modeling images of the structure below the surface of geothermal in 2D and 3D by means of data processing that can be seen from the flow chart below.

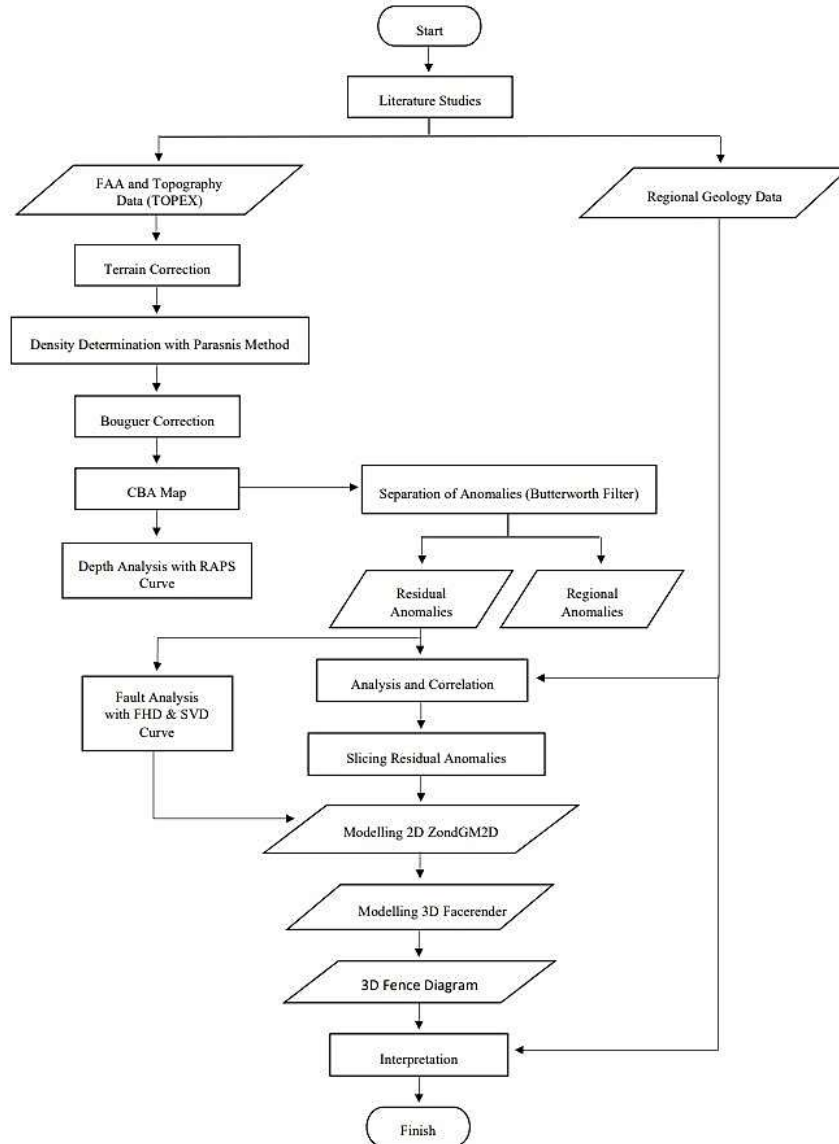


Figure 4. Research Flow Chart

RESULTS AND DISCUSSION

Complete Bouguer Anomaly (CBA)

After the FAA data is done correction Bouguer and field correction then obtained the results of Complete Bouguer Anomaly (CBA) which presents the distribution of gravitational anomalies and contrast of rock density in the research area that is Sembalun area due to differences in density below the surface (Figure 5).

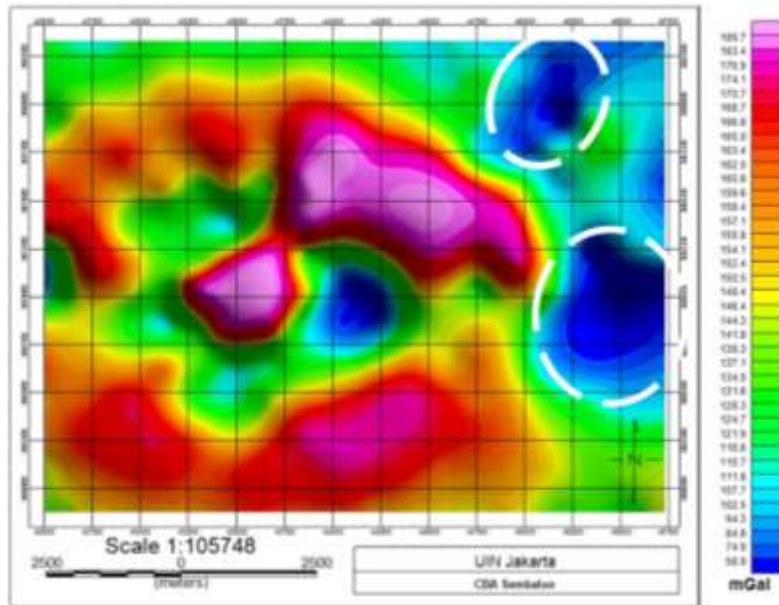


Figure 5. Map of Complete Bouguer Anomaly (CBA).

Can be seen on the CBA map, gravitational anomaly values in the research area ranged from 58.9 – 189.7 mGal, where the value of low anomaly (dark blue – light blue) ranges from 58.9 – 115.7 mGal, the medium anomaly value (dark green – yellow) ranges from 118.8 – 146.4 mGal and the high anomaly value (orange – purple) ranges from 148.4 – 189.7 mGal. From some literature, the low anomaly value on the CBA map in the east and northeast is thought to be the Sembalun geothermal prospect area. Low anomalies are associated with low density owned by geothermal fluids that are usually hot water, hot steam or a mixture of water and hot steam contained in reservoir rocks.



Figure 6. Map of Complete Bouguer Anomaly (CBA).

If overlay on regional geological map and CBA map (Figure 6) area that has geothermal prospects can be divided into two areas, first the area located in the northeast is Sembalun-Lawang area which is on the caldera floor and Mount Prigi area. Then the second area is in the Sembalun-Bumbung area which is on the caldera floor and around the Sebau hot spring manifestation area.

Topographic Map

On the topographic map, it appears that the height in the area of Mount Rinjani, Mount Anakdare, Mount Prigi and Caldera Sembalun (Figure 7).

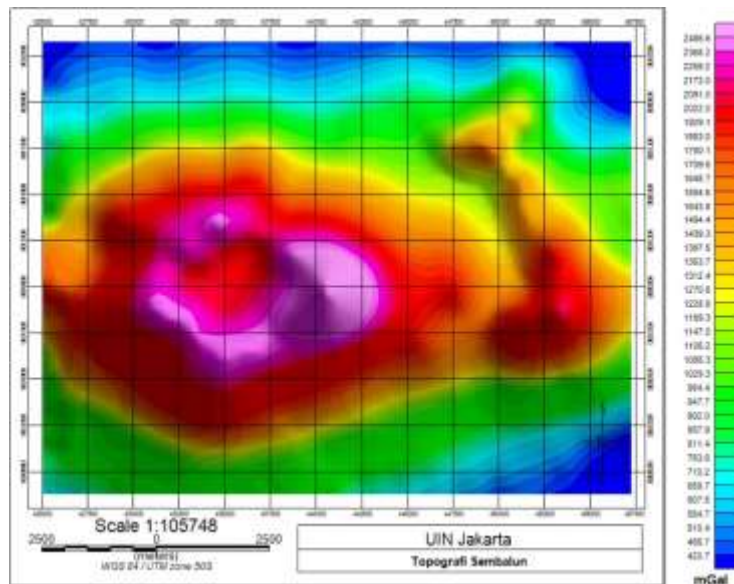
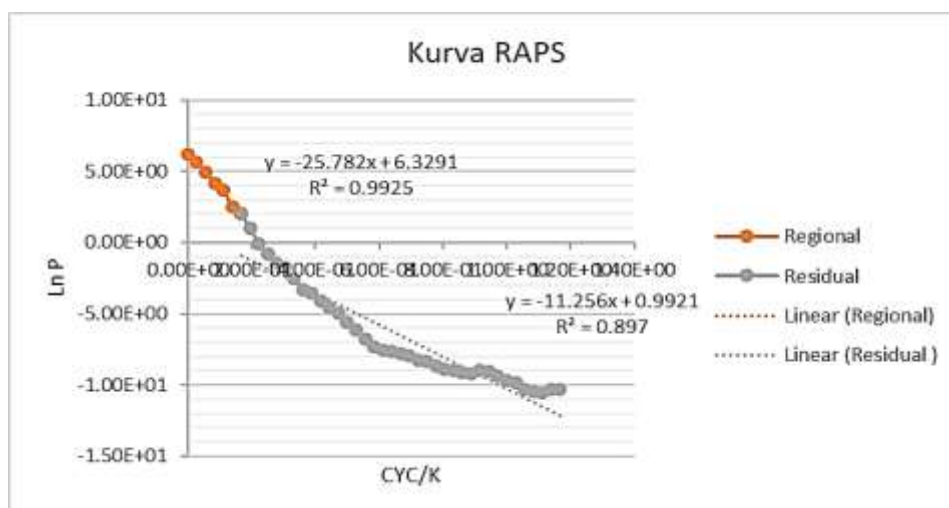


Figure 7. Topographic Map.

On the topographic map, the height of the research area varies with a value of about 420.7 – 2486.6 meters above sea level. Topographic maps have one function to validate whether the Complete Bouguer Anomaly value is true or not. In this study the value of Complete Bouguer Anomalies is valid because in the formulation of gravitational values, the value of height is inversely proportional to the value of gravitational acceleration, the higher the surface, the smaller the value of gravitational anomalies and vice versa.

Analisa Kurva Radially Average Power Spectrum (RAPS)

In the process of analyzing the RAPS curve aims to estimate the depth value of residual and regional anomalies which then this depth information will be used to create depth limits for both 2D and 3D conceptual models (Figure 8).



Gambar 8. Curve Radially Average Power Spectrum (RAPS).

From the RAPS curve, the gradient of residual zones and regional zones, residual and regional depths can be calculated by formulating gradient values divided by 4 times π (3.14), regional depth of 2.051666371 km and residual depth of 0.89572402 km. From

the depth of each of these zones can be concluded that the creation of a conceptual model has a depth of about 2.05 km from the ground.

Anomaly Separation (Butterworth Filter)

The anomalous separation is done using Butterworth filter, where the selection of cut off zone between zoa residual and regional zone is at 10800 in central wavelength filter and 8 on degree filter (Figure 9).

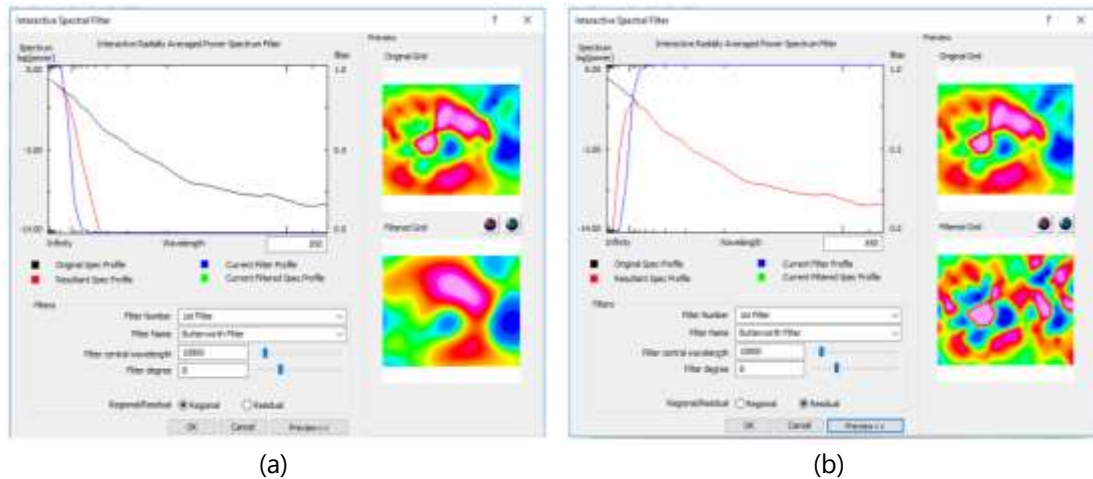


Figure 9. Determination of Cut Off Value of Butterworth Filter (a) Residual (b) Regional.

Regional Anomalies and Residual Anomalies

After the separation of anomalies using Butterworth filter will be produced residual anomalies (shallow anomalies) and regional anomalies (anomalies in) (Figure10).

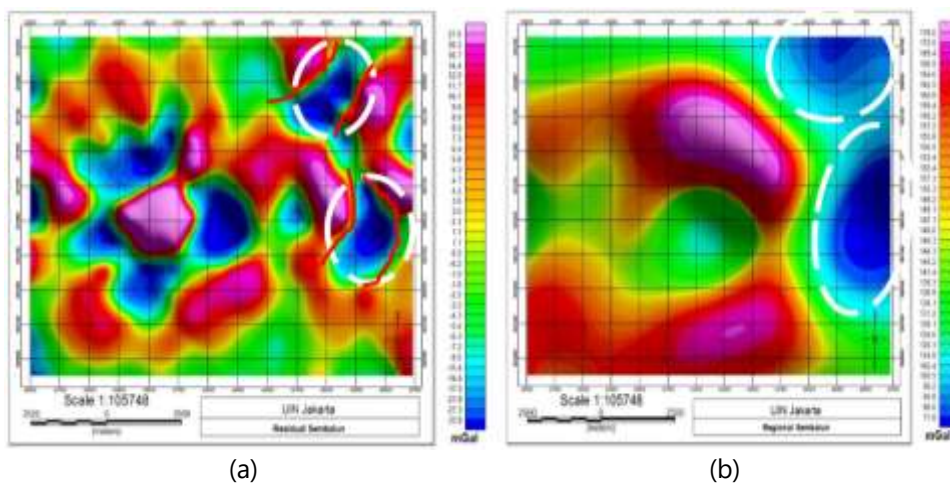


Figure 10. (a) Residual Anomalies, (b) Regional Anomalies

Can be seen on the map of residual anomalies (Figure 10.a), the distribution of gravitational anomalies is very visible heterogeneity on the surface because these anomalies are shallow caused by rocks or layers near the surface. Residual anomaly values in the research area ranged from -33.8 – 27 mGal, where low anomaly values ranged from -33.8 – (-7.2) mGal to target studies marked in blue. On the residual anomaly map it appears that the geothermal prospect area is controlled by minor faults found in areas

that have low anomalous values that are around Mount Prigi and the manifestation of Sebau Hot Springs.

However, when viewed on the regional anomaly map (Figure 10.b) it appears that the distribution of gravitational anomalies is very little heterogeneous on the surface because these anomalies are deep caused by rocks or layers deep within the earth's surface. Regional anomaly values in the research area ranged from 71.8 – 178 mGal, where low anomalous values ranged from 71.8 – 120.3 mGal to be the target of research marked in blue.

Validation Analysis and Fault Type

Validation analysis and type of fault is done to find out if in the research area there is a fault and what type of fault, this analysis is done using the method of correlation graph between First Horizontal Derivative (FHD) and Second Vertical Derivative (SVD) (Figure 12), FHD is done to determine the boundary of geological structure that causes anomalies and SVD is done to bring up the superficial effect of regional influence or to determine the type of fault in the research area.

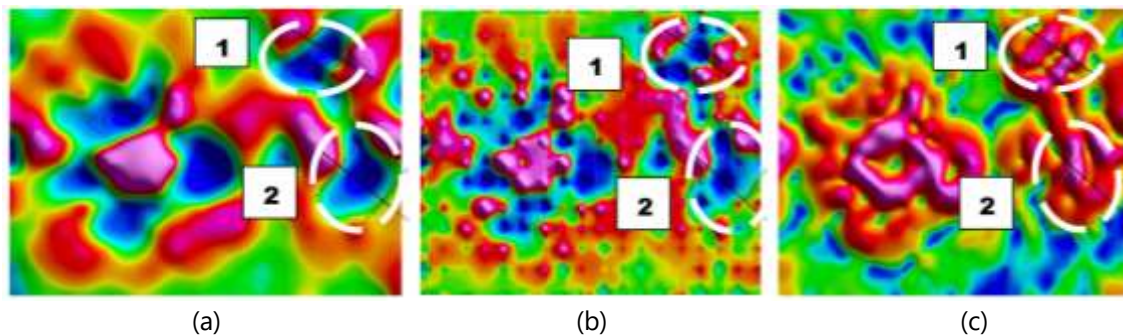


Figure 11. Fault Indication Area (a) Residual Anomaly, (b) SVD, (c) FHD

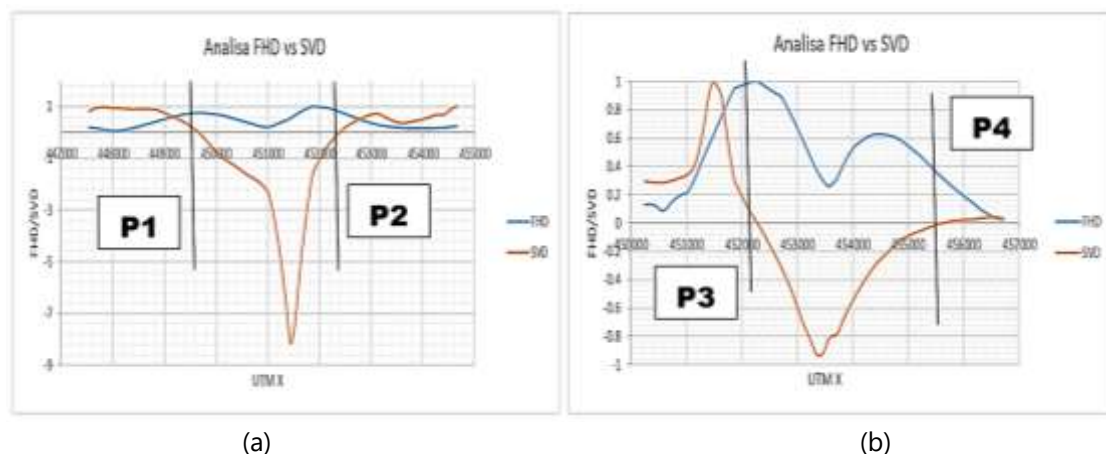


Figure 12. Graph Correlation Analysis FHD vs SVD (a) Region 1, (b) Region 2.

From the correlation between FHD and SVD graphs, it is seen that there are two faults in area 1 and two faults in area 2. According to the analysis of faults in area 1, the first fault (P1) has the characteristic of an up fault due to the value of SVD min > the svd max value where the SVD min value is -8.15 and the SVD max value is 0.875, this fault is the Talaga fault that is heading west to east which is near Mount Prigi. The second fault (P2) has the characteristic of an up fault due to the SVD min value > the SVD max value

where the SVD min value is -8.15 and the SVD max value is 0.7, the fault is the Pusuk fault, these two faults control the geothermal system located on the caldera floor (Sembalun-Lawang).

According to the analysis of faults in area 2, the third fault (P3) has normal fault characteristics because the value SVD min = SVD max value where the value of SVD min and SVD max is 1, this fault is a fault Tanakiabang heading southwest to northeast which is near the manifestation of Sebau Hot Springs. The fourth fault (P4) has the characteristic of an up fault due to the SVD min value > the SVD max value where the SVD min value is -1 and the SVD max value is 0.03, this fault is the Orok fault located near the manifestation of Sebau Hot Springs. These two faults control the geothermal system located near the manifestation of Sebau Hot Spring and on the caldera floor (Sembalun Bumbung).

2D Inversion Modeling

In this 2D inversion modeling, two slicings are performed on the residual anomalous map, the first slicing is directed from northwest to southeast (NW - SE) and the second slicing is northeast to southwest (NE - SW).

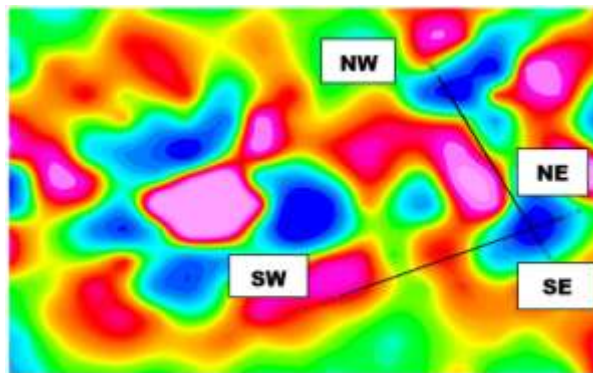


Figure13. Slicing On Residual Anomaly Map.

In the first slicing model directed from northwest to southeast (NW - SE) (Figure 14) it can be seen that the low anomaly (dark blue - light blue) which is thought to be a reservoir layer with a density value of about 1.4 gr/cc - 1.72 gr/cc which is estimated to be a layer of sand with high permeability controlled by 4 minor faults (black lines) which is the gap in the entry of meteoric water into the reservoir layer. This fault is close to Mount Prigi and near the manifestation of Sebau Hot Spring which has a depth of almost the same which is about 700 - 2500 m and a thickness of about 1800 m. In addition, this fault also controls the geothermal system located near the manifestation of Sebau Hot Spring and on the caldera floor (Sembalun Bumbung). Geothermal sources (white circles) in this cross-section are characterized by high anomalies (red - purple) with an estimated density of about 2.68 gr/cc - 3 gr/cc in the form of intrusion rocks of magma residual products that are young magma lava rocks that stretch along the caldera floor (Sembalun Lawang - Sembalun Bumbung) with a depth of > 2500 m. And the last layer is a thin layer of hood (red circle) which is suspected as an alluvium layer with a density value of about 1.8 gr/cc - 2.2 gr/cc with a depth of about 0 - 500 m.

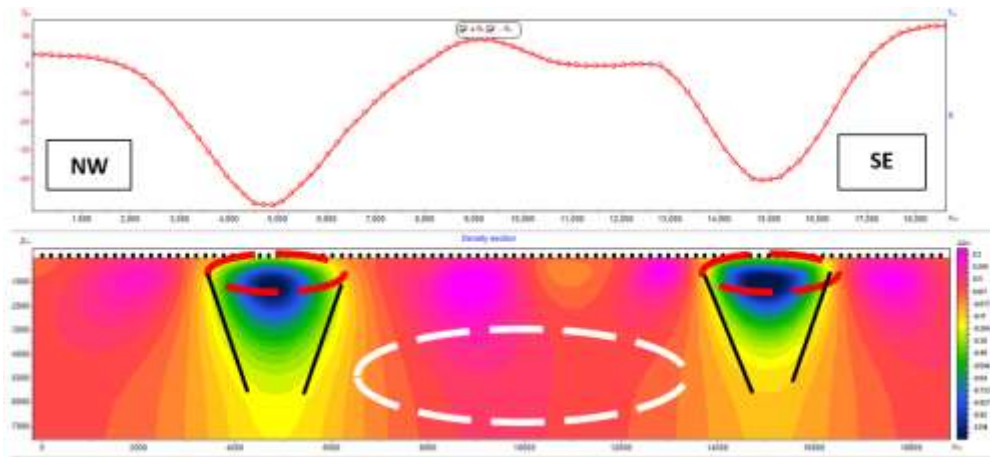


Figure 14. 2D Modeling Northwest to Southeast (NW - SE).

In the second slicing model directed northeast to southwest (NE - SW) (Figure 15) it can be seen that the low anomaly (dark blue - light blue) which is thought to be a reservoir layer with a density value of about 1.4 gr/cc – 1.72 gr/cc is estimated to be a layer of sand with high permeability controlled by 2 minor faults (black lines) which is a meteoric water gap into the reservoir layer. This fault is estimated to be near the manifestation of Sebau Hot Spring which has a depth of almost the same which is about 700 - 2500 m and a thickness of about 1800 m. Geothermal sources (white circles) in this cross-section are characterized by high anomalies (red - purple) with an estimated density of about 2.68 gr/cc - 3 gr/cc in the form of intrusion rocks magma residual products that are young andesite lava rocks hornblende, estimated to be near the caldera of Mount Rinjani which has a depth of > 2500 m. And the last layer is a thin layer of hood (red circle) which is suspected as an alluvium layer with a density value of about 1.8 gr/cc - 2.2 gr/cc with a depth of about 0 - 500 m.

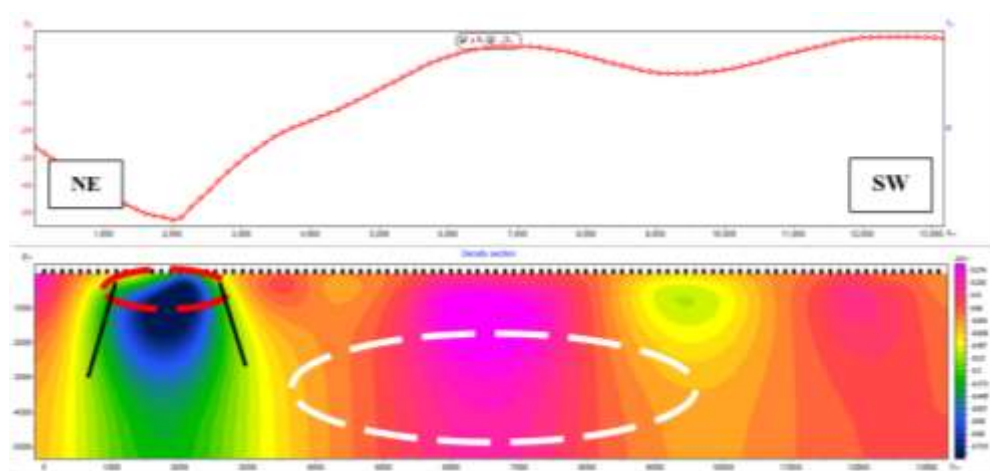


Figure 15. 2D Modeling Northeast to Southwest (NE - SW).

3D Inversion Modeling

In 3D inversion modeling, 3D fence diagrams and 3D face renders are created to be able to see the spread of subsurface density in 3D or evenly. On the 3D face render model can be seen 3D models below the surface solidly, it is seen that in 3D face render the result is correlated with the 2D inversion model (Figure 16), but in this 3D inversion is only done setting the depth up to 2 km in accordance with the analysis of the RAPS

curve. Can be seen intrusion rocks (white circles) namely hornblende andesite lava rocks clearly at a depth of 1 km - 2 km located along the caldera floor (Sembalun Lawang - Sembalun Bumbung).

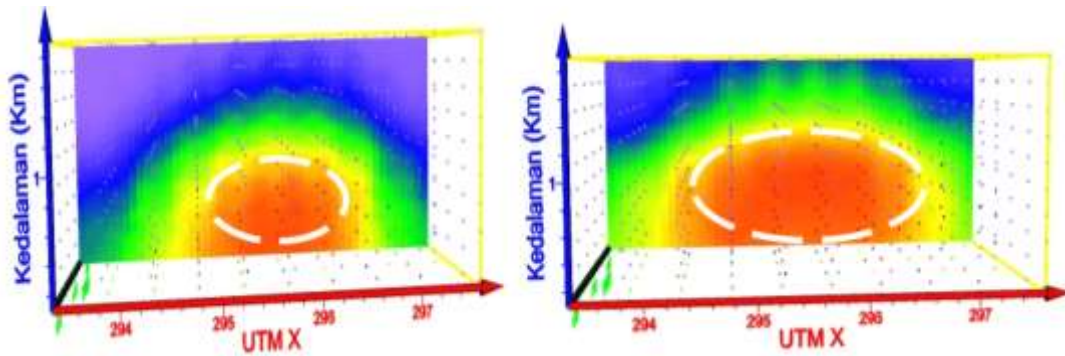


Figure 16. Face render 3D Modeling.

In the 3D fence diagram model can be seen subsurface 3D model in section, it appears that in 3D fence diagram the result is correlated with the 2D inversion model (Figure 17), but in this 3D inversion is only done setting depth up to 2 km in accordance with the analysis of the RAPS curve. Can be seen intrusion rocks (white circles) namely hornblende andesite lava rocks clearly at a depth of 1 km - 2 km located along the caldera floor (Sembalun Lawang - Sembalun Bumbung).

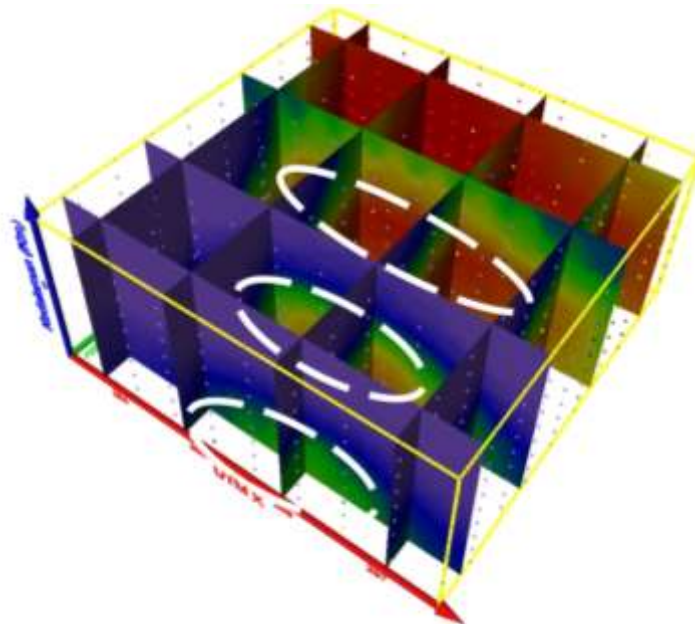


Figure 17. Modeling 3D Fence Diagram.

CONCLUSION

Based on the results of research conducted by gravity method in Sembalun area, East Lombok, West Nusa Tenggara, it can be concluded that:

1. Anomaly low value on the CBA map became the target of research as a geothermal prospect with a value between 58.9 – 115.7 mGal located in the east (Sembalun-Bumbung) and northeast (Sembalun-Lawang).

2. The prospect of geothermal Sembalun is controlled by the Talaga fault and Pusuk fault on the caldera floor (Sembalun-Lawang). Meanwhile, Tanakiabang fault and Orok fault that control the prospect of geothermal near the manifestation of Sebau Hot Spring and on the caldera floor (Sembalun Bumbung).
3. 2D modeling correlates with 3D modeling where geothermal sources are estimated to have a density of 2.68 gr/cc – 3 gr/cc consisting of hornblende andesite lava with a depth of > 2500 m, reservoir layer that is suspected sand layer has a density of 1.4 gr/cc - 1.72 gr/cc with a depth of 700 - 1200 m and a thin layer of hood that is suspected alluvium layer has a density of 1.8 gr/cc - 2.2 gr/cc with a depth of 0 - 500 m.

REFERENCE

- [1] M. Basuki Hadimuljono, et al. 2019. "Geothermal Economics Handbook in Indonesia". Yogyakarta: Anin.
- [2] Ministry of Public Works. "Medium Term Infrastructure Investment Development Plan – Profile of East Lombok Regency".
- [3] S. Andi Mangga. 1994. "Geological Map of Lombok Sheet, West Nusa Tenggara".
- [4] Maryanto, et al. 2009. "Mineralogy Matrix Breccias Volcano Pleistocene End – Quarter Based on Data XRD di East Lombok Region, West Nusa Tenggara". JSDG vol. 19 numb. 1.
- [5] Herry Sundhoro, et al. 2007. "Geological Research and Geochemical Geothermal Area Sembalun, East Lombok Regency – West Nusa Tenggara. Proceedings of Exposure of Field Activities dan Non Field". Geological Resources Center.
- [6] W. M. Telford, et al. 1990. "Applied Geophysics", Newyork: Cambridge University Press.
- [7] Marchdofayana Pane, dkk. "Modeling 2D dan 3D Subsurface Geological Structure in Magnetic Data in Flores Sea".
- [8] Ari Yuni Ani. 2011. "Analysis of Subsurface Structure in Surakarta Region Using Gravity Method. Surakarta: University of Eleven March".
- [9] A. Darma and A. Prasetyo. 2019. "Mathematical Analysis on Bouguer Correction and Correction of Topex Satellite Gravitational Data Field in Geological Condition Determination of Palu Koro Fault Case Study, Central Sulawesi". Journal of Geosciences, Vol. 5, Numb. 3, pp. 91-100.
- [10] Hendra Grandis. 2009. "Introduction to Geophysical Inversion Modeling". Bandung: CV. Bhumi Printing.
- [11] R. Lewerissa. "Design of Matlab-Based Non-Linear Inversion Modeling and Horizontal Gradient of Matlab-Based Earth Gravity Anomalies (Case Study: Semi-Infinite Horizontal Sheet and Faulted Vertical Sheet Models)". pp. 58-65.
- [12] M. Nur Hadi, dkk. 2007. "Geoelectric And Head-On Research of Sembalun Geothermal Area, East Lombok Regency – NTB. Proceedings of The Presentation of Field and Non-Field Activities Results". Geological Resources Center.

Effect of Temperature and Heating Resistant Time on Wear Properties of Molybdenum/Alumina Composites

Rizal Indrawan¹

¹Shipbuilding Institute of Polytechnic Surabaya, Teknik Kimia Street, Kampus ITS, Sukolilo, Surabaya, East Java, Indonesia

[†]rizal11307@ppns.ac.id

Submitted: January 2022; Revised: June 2022; Approved: June 2022; Available Online: October 2022

Abstract. The wear properties of metals are very important in manufacturing. This is evidenced in the many studies that analyze the wear properties of a metal. This study uses Metal Matrix Composites, where the manufacturing process uses metal as the matrix and ceramics as reinforcement with powder metallurgy manufacturing methods. Where the powder of the two composite materials is compacted and heated at a certain temperature to form a solid composite material. The purpose of this study is to ensure that the mechanical properties of the Mo/Al₂O₃ composite are greater than that of the constituent material. In this study, molybdenum powder was used as a matrix material and alumina as a reinforcing material. Mo has excellent mechanical properties, namely hardness and excellent wear resistance. Al₂O₃ has excellent wear resistance properties. Research variables include heating temperature of 900, 1000, 1100 °C and holding time of heating process for 0.5, 1, 1.5 hours with compaction pressure of 125 MPa and weight fraction of Mo by 80% and Al₂O₃ by 10%. Based on the test results, the highest sinter density was found at a sintering temperature of 1100°C and a sintering holding time of 1.5 hours at 6.831g/cm³. The value of porosity and wear rate is getting lower, namely 28.8% and the wear rate is 0.0012 mm/minute.

Keywords: wear properties, Mo/Al₂O₃ composite, temperature, heating holding time

DOI : [10.15408/fiziya.v5i1.24455](https://doi.org/10.15408/fiziya.v5i1.24455)

INTRODUCTION

Mo/Al₂O₃ composites were investigated with the hope that these materials have better mechanical properties than the natural mechanical properties of Mo and Al₂O₃ materials. This parameter depends on various factors. Including the type of powder material, particle size and shape, and the process of making the composite. In this study, Molybdenum (Mo) powder was used as a matrix material and Aluminum Oxide (Al₂O₃) as a reinforcing material. Mo has excellent mechanical properties, namely hardness, high modulus of elasticity, and excellent wear resistance. Meanwhile, Al₂O₃ material has high wear resistance.

Starting with the homogenization of the two powder materials using a planetarium ball mill, then the wet mixing process was carried out using a magnetic

stirrer. After that the cold compaction process with a pressure of 125 MPa. Then the sintering process is carried out at temperatures of 900, 1000, 1100 °C and the sintering process holding time is 0.5, 1, 1.5 hours in an argon atmosphere. The writing of this paper discusses the results of the wear-resistant properties of Mo/Al₂O₃ composite materials and the characterization of these materials.

METHODS

Molybdenum Powder Characterization

In the manufacture of Mo/Al₂O₃ composites, the Mo material is used as a matrix. Mo has a very high hardness and high elasticity value as well. Mo material is very resistant to high temperatures so it is very suitable to be used as a matrix in the manufacture of Mo/Al₂O₃ composites. The initial test on this Mo powder used SEM/EDX Testing. To analyze the Mo powder material using SEM. The following test results using SEM are shown in figure 1.

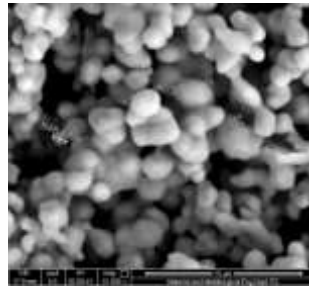


Figure 1. Mo Powder SEM Test Results.

In figure 1, it can be seen that the size of Mo powder is 0.9-3 μm at 15000× magnification, so there is no need for sieving because the grain size is considered homogeneous. And it can be seen that Mo powder has a dendritic shape and is macroscopically gray in color. To identify any elements contained in Mo powder, the EDX test was carried out. The results of the EDX test are shown in figure 2.

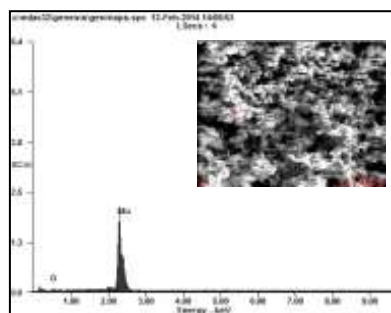


Figure 2. Test Results SEM-EDX Mo Powder.

Based on the results of the SEM - EDX test, it is known that the majority element content contained in the powder is Mo, which is 91%wt with 8.11%wt of O in it.

Table 1. Elemental Composition of Molybdenum.

Element	Wt%	At%
OK	08,11	34,6
MoL	91,89	65,4
Matrix	Correction	ZAF

Alumina Powder Characterization

In this research, alumina powder is used as a reinforcing material. Alumina has high wear resistance. Alumina is also resistant to high temperatures so it is very suitable as a reinforcement in the manufacture of Al_2O_3 composites. Therefore, Alumina material is used as a reinforcement in Al_2O_3 composites. To analyze the Al_2O_3 powder material using SEM. The following test results using SEM are shown in figure 3.

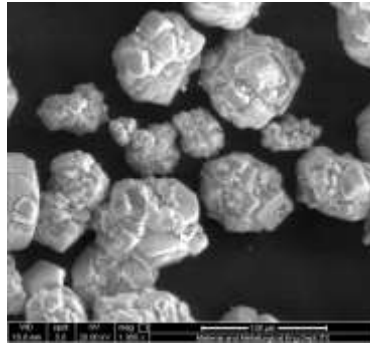


Figure 3. Alumina Powder SEM Test Results.

In figure 3 it can be seen that the size of the alumina powder is 40 - 90 m at 1000 \times magnification, so it is necessary to enrich it so that the grain size can be homogeneous. And it can be seen that the alumina powder has a polygonal shape and is macroscopically white in color. To identify what elements are contained in alumina powder, the EDX test is carried out. The results of the EDX test are shown in figure 4.

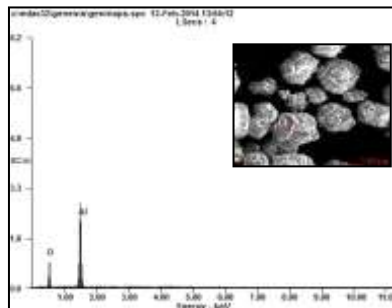


Figure 4. Test Results SEM-EDX Alumina Powder.

Based on the results of the SEM - EDX test, it is known that the majority element content contained in the powder is Al which is 56.67%wt with 43.33%wt of O in it.

Table 2. Elemental Composition of Alumina.

Element	Wt%	At%
OK	43,33	56,32
AlK	56,67	43,68
Matrix	Correction	ZAF

Mo/ Al_2O_3 Composite Manufacturing Process with Powder Metallurgy

In the process of making the Mo/ Al_2O_3 composite, the first step is to characterize each powder, namely molybdenum powder and alumina powder. The size of the molybdenum powder is smaller, namely 0.9-3 μ m compared to the size of the alumina

powder which has a size of 40-90 μ m. Therefore, a vibrator sieving process was carried out on alumina powder in order to obtain a smaller powder size. After that, the two powders were mixed using the wet mixing method and then a cold compaction process was carried out with a pressure of 125 MPa. After that, the heating process is carried out with variations in heating temperatures of 900, 1000, 1100 $^{\circ}$ C and variations in the holding time of the heating process for 0.5, 1, 1.5 hours. Then the testing phase was carried out on the Mo/Al₂O₃ composite

RESULTS AND DISCUSSIONS

Mo/Al₂O₃ Composite Characterization

At the beginning of the heating process there is a rearrangement of the particles that are in contact so that the contact area between the particles will be better. Neck growth begins to occur in the contact area between particles. Furthermore, at the grain growth stage the porosity structure becomes finer, but remains interconnected until the end of heating. The growing grains will press against each other, causing the empty space for porosity to shrink. And at this final stage, the closed porosity will shrink as a result of the diffusion process. Parameters that affect the heating process include temperature and heating holding time. After the heating process is carried out, the composite is weighed and its mass calculated, then using the Archimedes principle, the density of sinter is obtained.

Table 3. Sintered Density Mo/Al₂O₃.

Temperatur ($^{\circ}$ C)	Holding Time (h)		
	0.5	1	1.5
900	6.529	6.633	6.714
1000	6.725	6.738	6.759
1100	6.799	6.819	6.831

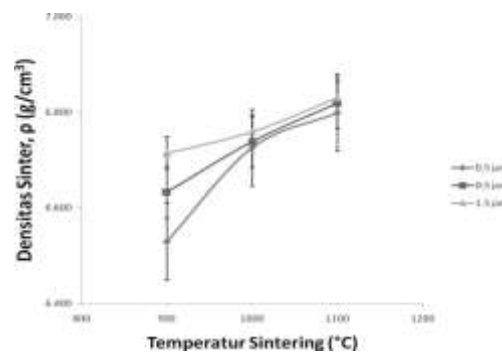


Figure 5. Graph of Relationship between Sintering temperature and Sintered Density of Mo/Al₂O₃ Composite.

Figure 5 shows the effect of the sintering temperature on the sintered density value. The highest density was shown by the Mo/Al₂O₃ composite which was heated at a temperature of 1100 $^{\circ}$ C for 1.5 hours, which was 6.831 g/cm³. As the sintering temperature increases, the sinter density will increase the heating holding time also affects the density of the sintered composite, where the highest density is found in the

heating holding time for 1.5 hours with a temperature of 1100 °C. The relationship between heating resistance time and sinter density can be illustrated in figure 6.

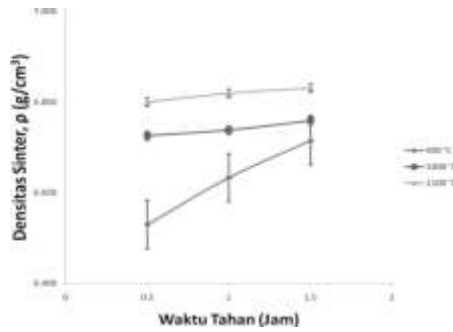


Figure 6. Graph of Relationship between Sintering Resistant Time to Sintered Density of Mo/Al₂O₃ Composite.

From figure 6, it can be seen that there is a relationship between the heating resistance time and the sinter density where the longer the heating holding time, the relative sinter density shows an increase.

In general, the effect of temperature and heating holding time on the sinter density can be seen in Figures 5 and 6 where the higher the heating temperature and time, the higher the sinter density. The results obtained are in line with the theory. The higher the heating temperature, the higher the activation energy, so that the driving force for grain growth is greater. Then as the holding time increases in the heating process, the greater the density of the sinter. This is due to the higher grain growth and coarsening. A long heating time will increase the heating rate. Shrinkage is based on the change in sample dimensions after heating. During heating, the bulk transport process will cause changes in the distance between particles due to neck growth. This causes shrinkage in the compacted powder

Table 4. Mo/Al₂O₃ Composite Shrinkage.

Temperature (°C)	Holding Time (Hour)	
	0.5	0.5
900	3.85	900 3.85
1000	4.85	1000 4.85
1100	5.71	1100 5.71



Figure 7. Graph of Relationship between Sintering Temperature and Shrinkage of Mo/Al₂O₃ Composites.

Figure 7 shows the effect of heating temperature on the percentage of sample shrinkage after undergoing the heating process. The highest percentage of shrinkage was shown by the Mo/Al₂O₃ composite which underwent a heating process at a temperature of 1100 °C for 1.5 hours, which was 7.26%. As the heating temperature increases, the shrinkage percentage will increase. This increase can be seen in samples that have a heating holding time of 1.5 hours. At a temperature of 900 °C the percentage of shrinkage is only 3.85%, but at a temperature of 1100 °C it reaches 7.26%.

The heating resistance time also affects the shrinkage of the composite dimensions, where the highest percentage of shrinkage is found in the heating holding time for 1.5 hours with a temperature of 1100 °C, which is 7.26%. The relationship between heating resistance time and shrinkage percentage can be illustrated in figure 8.



Figure 8. Graph of Relationship between Sintering Resistant Time and Shrinkage of Mo/Al₂O₃ Composites.

From figure 8, it can be seen that there is a relationship between the heating resistance time and the shrinkage percentage where the longer the heating holding time, the relative shrinkage percentage shows an increase. This increase can be seen in the samples that have undergone a heating process at a temperature of 900 °C. However, the increase due to the effect of heating holding time is not so significant when compared to the effect of temperature. At a temperature of 900 °C with a heating holding time of 0.5 hours the percentage of shrinkage is only 3.85%, while with a heating holding time of 1.5 hours it only reaches 4.81%. It can be seen in Figure 7 and Figure 8 that the effect of temperature plays a greater role in shrinkage. The higher the heating temperature, the faster the heating rate.

Porosity is an incoherent part after the composite has undergone a heating process, in the form of a void filled with gas or lubricant. The manufacture of composites by powder metallurgy method can allow the occurrence of porosity. Porosity is also related to the value of the sintered density. The higher the porosity contained in the composite, the lower the sinter density.

So, then the relationship between temperature and heating resistance time on the level of porosity in the Mo/Al₂O₃ composite can be described in Figure 9 below:

Table 5. Mo/Al₂O₃ Composite Porosity Value.

Temperature (°C)	Holding Time (Hour)	
	0.5	0.5
900	0.320	900 0.320
1000	0.299	1000 0.299
1100	0.292	1100 0.292

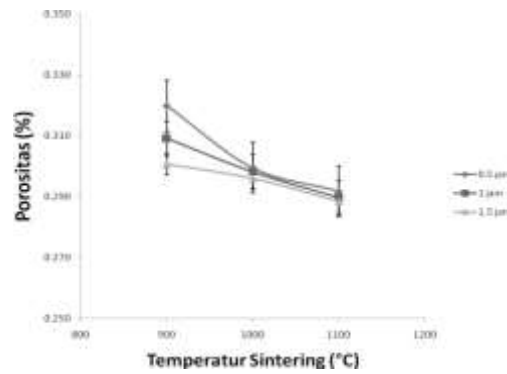


Figure 9. Graph of Relationship between Sintering Temperature and Porosity of Mo/Al₂O₃ Composite.

From figure 9 it can be seen that the lowest porosity is indicated by the Mo/Al₂O₃ composite which is heated at a temperature of 1100 °C for 1.5 hours, which is 28.8%. Then the porosity decreases with increasing heating temperature. Heating resistance time also affects the porosity level of the Mo/Al₂O₃ composite. The effect of heating resistance time on the porosity of the Mo/Al₂O₃ composite is shown in figure 10.

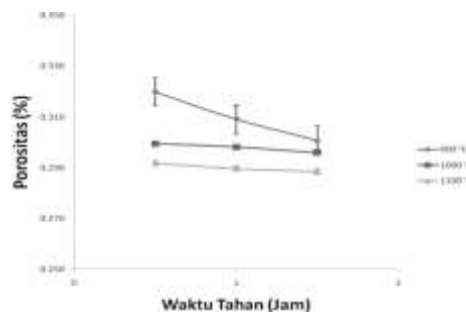


Figure 10. Graph of Relationship between Sintering Resistant Time and Porosity of Mo/Al₂O₃ Composites.

Based on figure 10, it can be seen that the highest porosity is found in the heating holding time for 0.5 hours with a heating temperature of 900 °C, which is 32%. From Figure 10 it can also be seen that the longer the heating holding time, the lower the level of porosity contained in the Mo/Al₂O₃ composite.

Mechanical Properties of Mo/Al₂O₃ Composites

The mechanical properties of a composite can be determined by providing a mechanical test. In this study, the mechanical test used is the Wear Test. Wear can be defined by how quickly a material is damaged during use. By using this wear test tool can provide information on the age of a material how long it can last and be used.

After the wear resistance test was carried out, the wear value was obtained from the influence of temperature and heating resistance time on the wear value of the Mo/Al₂O₃ composite. This relationship can be seen in figure 11.

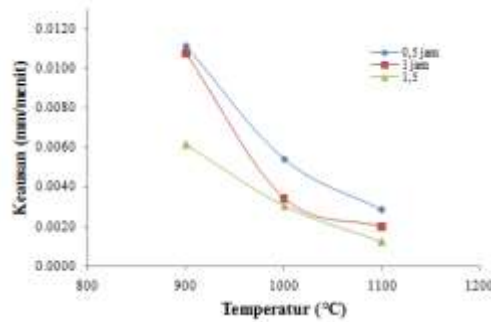


Figure. 11 Graph of Relationship between Sintering Temperature and Wear Value of Composite Mo/Al₂O₃.

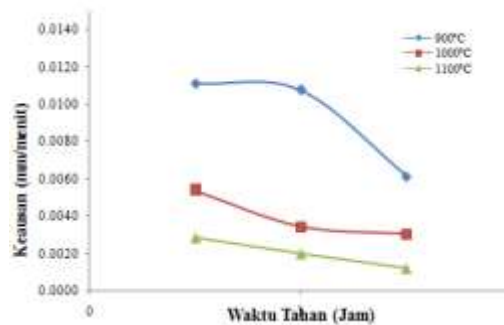


Figure 12. Graph of Relationship between Sintering Resistance Time and Hardness of Mo/Al₂O₃ Composites.

Figure 11 and figure 12 show the wear value of the Mo/Al₂O₃ composite, where the highest wear value is found at a heating temperature of 900 °C with a heating holding time of 0.5 hours, which is 0.0111 mm/minute. While the lowest wear value is found in the Mo/ Al₂O₃ composite which is heated at a temperature of 1100 °C and a heating holding time of 1.5 hours is 0.0012 mm/minute. From Figure 12 it can also be seen that the greater the heating temperature, the lower the wear resistance of the Mo/ Al₂O₃ composite.

Interface Analysis on Mo/Al₂O₃ Composites

Composites are closely related to the quality of the bond between the matrix and the reinforcement. The interface area is an area that can be identified by the presence of bonds between the matrix and reinforcement after the heating process, so that it can show differences in the interface area in the composite. Figure 13 shows the interfacial bonding of the composite at a sintering temperature of 900 °C with a sintering time of 0.5 hours.



Figure 13. Results of SEM Observations in the Mo/Al₂O₃ Composite Interface with a Sintering Temperature of 900 °C and a Hold Time of 0.5 Hours.

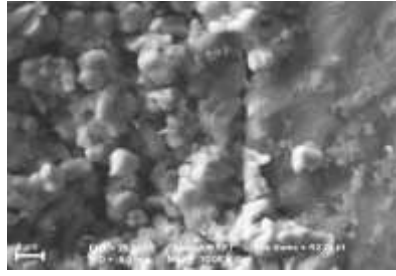


Figure 14. SEM Observation Results in the Mo/Al₂O₃ Composite Interface with Sintering Temperature 1000 °C and Holding Time for 1 Hour.

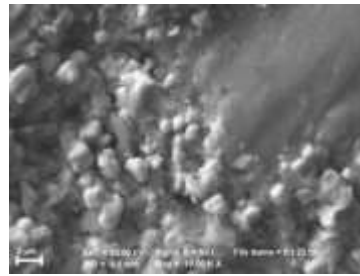


Figure 15. Results of SEM Observations in the Mo/Al₂O₃ Composite Interface with a Sintering Temperature of 1100 °C and a Hold Time of 1.5 Hours.

On SEM observations as shown in figure 13, it can be seen that the interphase surface has not yet formed tightly. The grains do not seem to blend with one another. When the heating temperature is increased as shown in figure 14 by 1000 °C and the holding time is added for 1 hour, it starts to appear that there are parts that are fused but still not tight. And when the heating temperature is 1100 °C and the holding time is 1.5 hours, it can be seen that the interphase surfaces have begun to form tightly and begin to coalesce as shown in figure 15. This is because the increase in heating temperature and the holding time of the heating process greatly affects the bond between powders. Mo and Al₂O₃ powder.

CONCLUSIONS

From the test results in this study, it can be concluded that:

1. The lowest wear value is at a heating temperature of 1100 °C with a heating holding time of 1.5 hours, which is 0.0012 mm/minute.
2. The highest wear value is found in the Mo/Al₂O₃ composite which is sintered at a temperature of 900 °C and a heating holding time of 0.5 hours, which is 0.011 mm/minute.
3. The density of the sintered composite Mo/Al₂O₃ shows that the higher the temperature and heating resistance time, the density of the sinter will increase. This is because the higher the heating temperature, the higher the activation energy, so that the driving force for grain growth is greater.
4. In SEM observation, it is known that the most perfect interfacial bond is in the sintering process of 1100 °C and the sintering holding time is 1.5 hours.

REFERENCES

- [1] U. A. Siagian, *PENGARUH PENAMBAHAN MOLIBDENUM TERHADAP STRUKTUR DAN KETAHANAN OKSIDASI PADUAN FeCrAlSi*. 2018.
- [2] S. E. E. Profile, "Multilayer Al₂O₃ / Mo composites," no. February, 2020.
- [3] K. Suarsana, I. M. Astika, and L. Suprpto, "Pengaruh Penguat Hibrid SiCw / Al₂O₃ Pada Komposit Aluminium Matrik Terhadap Sifat Konduktivitas Termal," *J. Ilm. Tek. DESAIN Mek.*, vol. 6, no. 1, pp. 147–151, 2017.
- [4] A. Alhamidi, S. Suryana, and S. Husein, "Sintesa dan Karakterisasi Material Ceramic Metal Composite (Ti_{1-x}Mox)C-NiCr melalui Proses Pemaduan Mekanik dengan Variasi Komposisi Molibdenum," *Tek. J. Sains dan Teknol.*, vol. 11, no. 1, p. 11, 2015, doi: 10.36055/tjst.v11i1.6968.
- [5] M. Terhadap, S. Mekanik, D. A. N. Struktur, M. Pada, B. Tahan, and K. Tipe, "Pengaruh penambahan unsur MOLIBDENUM (Mo) TERHADAP SIFAT MEKANIK DAN STRUKTUR MIKRO PADA BAJA TAHAN KARAT TIPE AISI 410," vol. 2, no. 1, pp. 43–50, 2019.
- [6] J. Zygmuntowicz, A. Łukasiak, P. Piotrkiewicz, and W. Kaszuwara, "Al₂O₃-cu-mo hybrid composites: Fabrication, microstructure, properties," *Compos. Theory Pract.*, vol. 19, no. 2, pp. 43–49, 2019.
- [7] A. I. Nafili, S. M. B. Respati, and B. Santoso, "Pengaruh kandungan alumina terhadap kekasaran permukaan dan foto mikro permesinan pada komposit Al-Al₂O₃," *J. Tek. Mesin Indones.*, vol. 12, no. 2, p. 94, 2018, doi: 10.36289/jtmi.v12i2.79.
- [8] I. W. L. Suprpto, K. Suarsana, and N. Santhiarsa, "EFEK KOMPOSISI DAN PERLAKUAN SINTERING PADA KOMPOSIT Al/(SiCw+Al₂O₃) TERHADAP SIFAT FISIK DAN KEAUSAN," *J. Muara Sains, Teknol. Kedokt. dan Ilmu Kesehat.*, vol. 1, no. 1, pp. 124–131, 2017.

Identification of Characteristics and Distribution of Subsurface Coal Using the 2D Geoelectric Method in Tanjung Palas Timur District, North Kalimantan

Putri Sekar Ayu Ningsih^{1,†}, Sutrisno¹, Tati Zera¹, Egie Wijaksono²

¹Physics Study Program, Faculty of Science and Technology, State Islamic University Syarif Hidayatullah Jakarta, Ir. H. Djuanda Rd. No.95, Cempaka Putih, Ciputat, South Tangerang City, Banten 15412, Indonesia.

² Center for Disaster Risk Reduction Technology (PTRRB)-Agency for the Assessment and Application of Technology (BPPT), Building 820, PUSPIPTEK, South Tangerang City, Banten 15314, Indonesia.

[†putri.sekar17@mhs.uinjkt.ac.id](mailto:putri.sekar17@mhs.uinjkt.ac.id)

Submitted: November 2021; Revised: April 2022; Approved: June 2022; Available Online: October 2022

Abstract. *Based on regional geology, Tanjung Palas Timur Subdistrict is included in the only formation, which includes coal seams. The depletion of oil and gas energy sources in Indonesia results in the need for other alternative energy sources, one of which is coal. This study aims to determine the characteristics of coal in the study area. This research was conducted in Tanjung Palas Timur Subdistrict, North Kalimantan using the geoelectric resistivity method with a pole-pole configuration and 8 tracks which are divided into 2 track blocks. The resistivity geoelectric method is used because it is very suitable for mining exploration. Data processing was done in 2D using Res2dinv software and 3D using Rockworks15 software. The results of the geoelectric data processing of line 1 to 8 show that the coal seam in the study area has a resistivity of 10-30 Ωm with a thickness varying from 17.22 m - 60 m as a type of lignite coal. In addition, the research area is also dominated by layers of clay and sandstones. The continuity of the coal seam is also seen in block 1 from line 3 in the southwest direction to line 1 in the northeast direction.*

Keywords: Coal, Geoelectric Resistivity, Pole-Pole Configuration, Res2dinv, Rockworks15

DOI: [10.15408/fiziya.v5i1.23106](https://doi.org/10.15408/fiziya.v5i1.23106)

INTRODUCTION

Oil and gas are natural resources that are mostly used to meet daily needs and as a contributor to the country's foreign exchange. However, as human needs increase in their daily activities, the consumption of oil and gas energy increases. Meanwhile, the energy sources needed are dwindling due to uncontrolled energy exploitation. Therefore, alternative energy is needed as a substitute for fuel oil and gas, one of which is coal.

Coal potential in Indonesia is spread over 4 regions that have the largest pockets of coal reserves, namely South Sumatra, South Kalimantan, Central Kalimantan and East Kalimantan based on the Ministry of Energy and Mineral Resources 2020 sources and North Kalimantan is ranked 9th province with the largest coal reserves. Coal has played

an important role for a long time, creating electric power and being the basic fuel for steel and concrete manufacture and other industrial activities. Coal is also the fastest growing source of fuel compared to oil, gas, nuclear, or other alternative energy [1]. Several studies using the resistivity geoelectric method to determine the distribution of coal include Sugeng and Widodo conducted research on coal prospects in the Muara Muntai area using the Schlumberger configuration modeled by manual curve matching [2], Hamid Umar conducted research on the potential of coal so that he could calculate the amount of coal reserves in the Massenrengpulu area [3], Elvira Azizah conducted a study that aims to determine the distribution of coal using the Wenner configuration in Tulungagung Regency [4], and M. Zainul he studied the distribution of coal using the geoelectric method of induced polarization in the Klatak area [5]. Meanwhile, this study aims to determine the characteristics and distribution of coal using geoelectric resistivity with a pole-pole configuration in order to obtain a deeper depth of coal.

Based on the regional geological sheet of Tanjung Redeb, the Tanah Kuning area has a sajaw formation. The sajaw formation includes interspersed clay, silt, sandstone, conglomerate, interspersed with coal seams. The presence of coal in the Tanah Kuning area, North Kalimantan is a potential to develop power plants or other industrial materials. One of the surveys that can be used to understand the potential distribution of coal below the surface is a geophysical survey using the geoelectrical resistivity method. Basically, the geoelectric method is based on Ohm's Law which considers a single current-carrying cylinder.

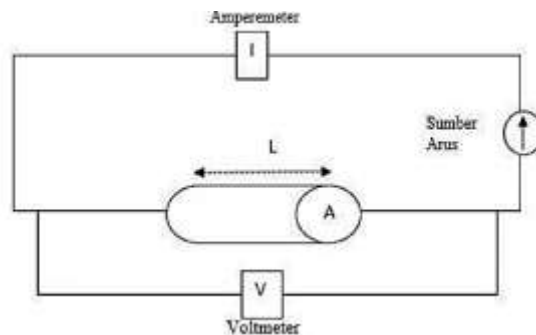


Figure 1. Parameters used in determining resistivity [6].

From figure 1, it can be seen that the electric current I flowing in a cylindrical material with a potential difference at both ends ΔV will be proportional to the cross-sectional area A and inversely proportional to the length L :

$$\rho = R \frac{A}{L} \quad (1)$$

Where ρ is the resistivity (Ωm), L is the length of the conductor cylinder (m), A is the cross-sectional area of the conductor cylinder (m^2), and R is the resistance (Ω). Meanwhile, according to Ohm's law, resistance R is formulated as follows:

$$R = \frac{V}{I} \quad (2)$$

R is resistance (Ω), V is potential difference (Volts), and I is current (Amperes). If equation 2 is substituted into equation 1, the resistivity value is:

$$\rho = \frac{VA}{IL} \tag{3}$$

In geoelectrical measurements, the subsurface medium is assumed to be homogeneous isotropically so that the generated electric current will spread throughout the medium with the same value. If an electric current meets a certain rock layer, there will be a deviation from the ideal condition, because each rock layer has a certain resistivity value. So that the quantity ρ_a can be formulated by

$$\rho_a = K \frac{\Delta v}{I} \tag{4}$$

where K is the geometry factor of the electrode configuration used. In field measurements, this research uses a pole-pole configuration.

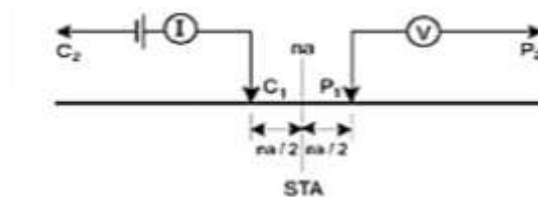


Figure 2. Pole-pole configuration electrode arrangement [7].

The apparent resistivity value obtained from this pole-pole configuration is expressed by the following equation:

$$\rho = 2\pi aR \tag{5}$$

where ρ is the apparent resistivity, a is the electrode spacing, which is the space between the C1 and P1 electrodes, and R is the resistivity measured in the field. The geometric factor of the configuration of the poles above is $2\pi a$.

To determine the value of the resistivity of coal, it is necessary to interpret the 2d modeling that has been processed by referring to the following references.

Table 1. Rock and mineral resistivity values [8].

Types of Rocks and Minerals	Resisivity (Ωm)
Clay	1 – 100
Silt	10 – 100
Sandstone	50 – 500
Conglomerat	$2 \times 10^3 - 10^4$
Breccia	75 – 200
Bituminous Coal	$0.6 - 10^5$
Anthracite	$10^{-3} - 2 \times 10^4$
Lignit	9 – 200
Granite	$5 \times 10^3 - 10^6$
Groundwater	0.5 - 300

METHODS

The research location is in Tanjung Palas Timur District, Bulungan Regency, North Kalimantan. The research started from December 2020 to March 2021. The data used was in the form of secondary geoelectric resistivity data belonging to the Center for Disaster Risk Reduction Technology (PTRRB), the Agency for the Assessment and Application of Technology (BPPT).

The resistivity geoelectric method is a method that can see or get a mine layer that has a resistivity difference with the surrounding layer. This method is used with the principle of injecting electric current through two current electrodes which is then measured the value of the resulting potential difference according to the arrangement of the electrodes used, then the apparent resistivity value will be obtained.

In this study using the geoelectric resistivity method. The resistivity geoelectric method is one of the geophysical methods that can be used to see the subsurface structure of the earth. This research uses geoelectric resistivity Pole-pole configuration method. The Pole-pole configuration is used because of its very wide horizontal coverage and its very deep depth investigation [9].

The research map shows that there are 2 blocks where block 1 consists of track 1 Ety, track 2 Ety, track 3 Ety, track 7 Yati and track 8 Yati. While in block 2, there are paths of Merana, namely trajectories of 4 Merana, trajectories of 5 Merana, and trajectories of 6 Merana. On each track has a length of 710 m with an electrode spacing of 10 m. Data processing is done using Res2dinv software to produce 2d modeling in order to identify subsurface rock types in the research area by looking at the resistivity value range and Rockworks 15 software is used in 3d modeling to see the distribution and continuity of coal and its total reserves.



Figure 3. Measuring trajectory point.

RESULT AND DISCUSSION

The results of data processing resulted in 8 tracks with each track length of 710 m and electrode spacing of 10. The results of the 2D cross-section obtained from the Res2dinv software were correlated with regional geological data and resistivity tables or other supporting data to obtain an accurate interpretation. The following is the result of a 2D cross-section of each track:

Track 1 Ety

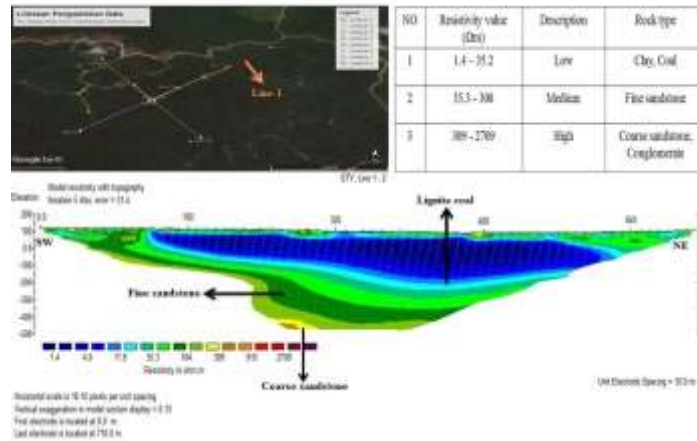


Figure 4. Cross section of the inversion of the path 1 Ety.

In this path, low resistivity values are shown in dark blue to light blue with resistivity ranging from 1.4 – 11.9 Ωm. This layer is thought to contain lignite type coal inserts because of its low resistivity value which is embedded in the clay layer. Coal was found at electrode 125 at a depth of 66.43 m to 113.44 m with a thickness ranging from 29 m. While the light green to dark green color has moderate resistivity values ranging from 36.3 Ωm to 104 Ωm which is suspected as a layer of fine sandstone. This fine sandstone layer is below the coal seam at electrode 40 at a depth of ±80.6 m which is spread evenly up to electrode 475. And for high resistivity values with yellow to red colors, resistivity from 309 Ωm to 2709 Ωm is deposited in the lowest layer of the surface with depth of 518 m at electrodes 270 – 325 m is suspected to be coarse sandstone. So, it can be seen that on the track 1 ety there are coal deposit which are summarized in table 2.

Table 2. Distribution of lignite coal.

Place the electrodes	Depth (m)	Resistivity (Ωm)
125	66.43 – 113.44	11.9 – 35.2

Track 2 Ety

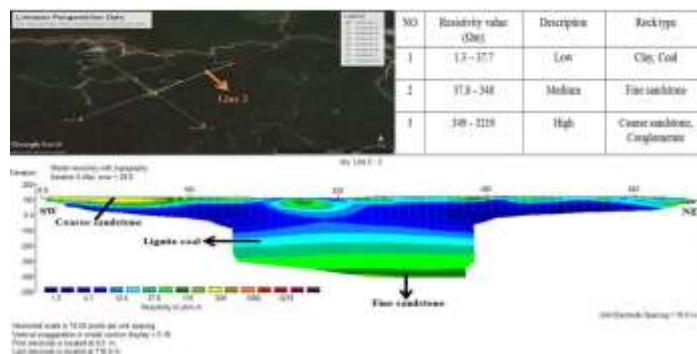


Figure 5. Cross section of the inversion of the path 2 Ety.

This path is dominated by low resistivity values indicated by dark blue to light blue with resistivity ranging from 1.3 Ωm – 12.4 Ωm . This layer contains inserts of lignite type coal at a depth of 293 – 331 m spread over 250 – 455 electrodes and a thickness of $\pm 30\text{m}$. While the light green to dark green color has a moderate resistivity value ranging from 37.8 m to 115 m which is still occupied by a layer of sandstone. A layer of sandstone is spread on the subsurface from the electrodes 220 – 460 m with a depth of 417 – 464 m. And for high resistivity values with yellow to red colors having resistivity from 349 Ωm to 3219 Ωm which are on the west side of the track with a depth of 4.2 m at electrodes 0 – 120 m, it is suspected as coarse sandstone.

Table 3. Distribution of lignite coal.

Place the electrodes	Depth (m)	Resistivity (Ωm)
250	293	4.1 - 12.4
455	331	12.5 – 37.7

Track 3 Ety

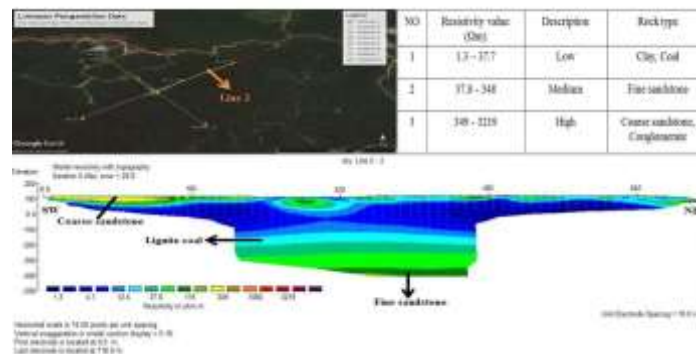


Figure 6. Cross section of the inversion of the path 3 Ety.

In the cross-section of the resistivity of the 3 ety path, it can be seen that the distribution of the layers is still the same as in the previous path. The upper layer consists of a layer that has a low resistivity value of 1.3 – 12.5 Ωm as a layer containing lignite coal because it is located around the clay layer. This coal seam starts from electrode 5 at a depth of 4.2 - 21.42 m with a layer thickness of $\pm 25\text{ m}$. Then in the layer below the coal which is the base, it is suspected to be sandstone which has a resistivity of 117 - 356 Ωm which is located at the 195 electrodes at a depth of $\pm 255\text{ m}$ and crosses from the west to the east of the track. Furthermore, in the third layer, namely the lowest layer with a depth of ± 470 , coarse sandstone is deposited with a resistivity of 1089 Ωm .

Table 4. Distribution of lignite coal.

Place the electrodes	Depth (m)	Resistivity (Ωm)
5	4.2 – 21.42	12.5 – 38.1

Track 4 Merana

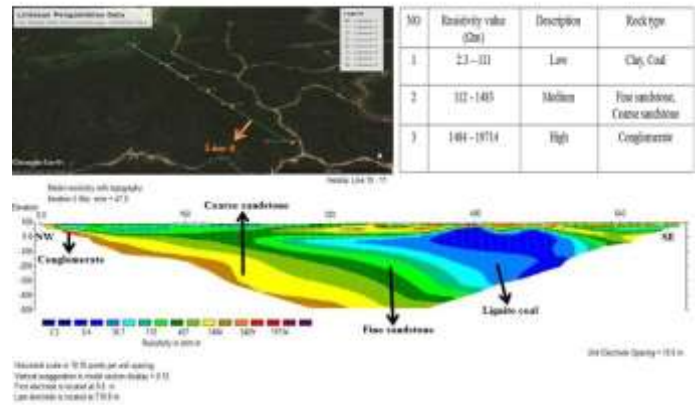


Figure 7. Cross section of the inversion of the path 4 Merana.

The picture above shows a yellow to brown color pattern with a high resistivity between 1484 Ωm – 5409Ω m which is interpreted as a rock layer containing coarse sandstone. This layer is at the electrodes with 31 m to 518 m. Dark green to light green color which has a resistivity of 112 Ωm – 407 Ωm is interpreted as a fine sandstone layer. The sandstone layer is between the coarse sandstone layer and the coal seam. Furthermore, the dark blue to light blue color with a resistivity of 30.7 Ωm is interpreted as containing coal seams. The coal seam is at a depth of 113 m at electrodes 395 to 545 electrodes with a layer thickness of ±39 m.

Table 5. Distribution of lignite coal.

Place the electrodes	Depth (m)	Resistivity (Ωm)
395 - 545	113	9 – 30.7

Track 5 Merana

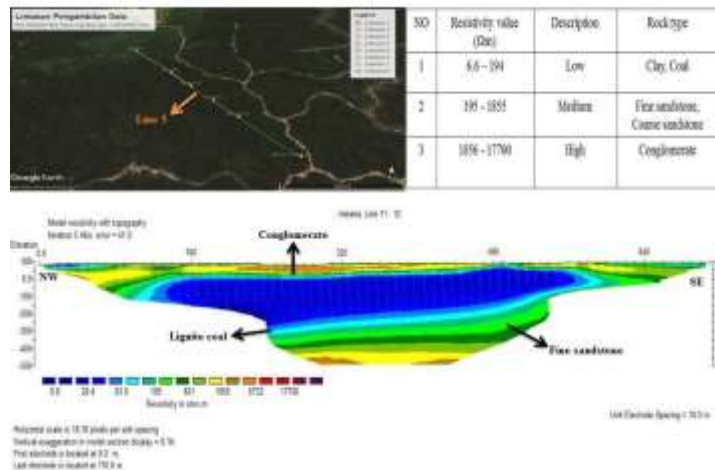


Figure 8. Cross section of the inversion of the path 5 Merana.

On track 5 Merana, the penetration depth reaches ± 520 m. From the cross section, there are at least 3 rock layers with low, medium, and high resistivity. The first layer in this cross-section has a high resistivity between 1586– 5732 Ω m (yellow to brown), this layer is probably a layer of conglomerate rock that has been weathered so that it is above the surface of the electrodes 150 – 460 m which crosses from northwest to southeast at depth of 4.2 m. The second layer is with a low resistivity between 6.61 – 20.4 Ω m (dark blue to light blue) which allows the presence of coal types starting at electrodes 135 to 535 at a depth of 153.14 m and the thickness of coal in this layer reaches ± 60 m. And the third layer is a layer with a medium resistivity of 195 - 601 Ω m (light green to dark green) at a depth of 415 m from the ground surface. This layer is probably a sandstone layer.

Table 6. Distribution of lignite coal.

Place the electrodes	Depth (m)	Resistivity (Ω m)
135 - 535	153.14	6.61 – 20.4

Track 6 Merana

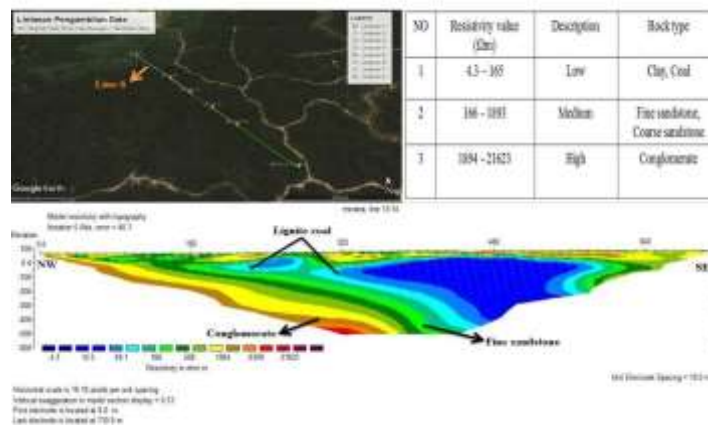


Figure 9. Cross section of the inversion of the path 6 Merana.

From the 2D cross-section above, a yellow to brown color pattern can be seen on the left side of the track with a resistivity of 1894– 6399 Ω m which is interpreted as conglomerate rock. Dark blue to light blue color with low resistivity of 14.5– 49.1 Ω m which is interpreted to contain coal seams. Coal seams were found at electrodes 240 and 335 - 535 m at a depth of 132.35 m with a thickness of coal in this layer reaching ± 60 m. Furthermore, between the conglomerate and coal layers there is a moderate resistivity between 166 - 560 Ω m which is interpreted as a sandstone layer. This sandstone layer is widely spread from near the surface to the subsurface.

Table 7. Distribution of lignite coal.

Place the electrodes	Depth (m)	Resistivity (Ω m)
240	100 – 132.35	30.5 - 49.1
335 - 535	132.3	49.1

Track 7 Yati

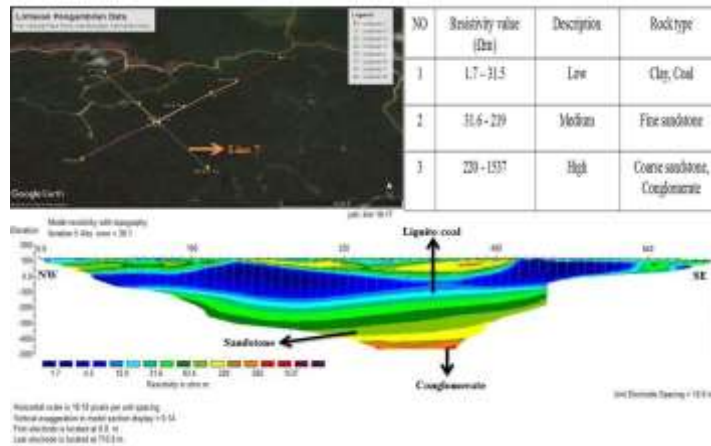


Figure 10. Cross section of the inversion of the path 7 Yati.

From the picture above it can be seen that it consists of 3 layers, the first layer of light blue color with a low resistivity of $\sim 12 \Omega\text{m}$ at electrodes 55 to 505 m at a depth of 96.26 m is interpreted as coal seam. This layer has a thickness of ± 17.22 m and is located in a layer of clay so that it has a low resistivity value. The second layer is a layer which is interpreted as a fine sandstone layer having a resistivity of $> 83.4 \Omega\text{m}$ at a depth of 113.44 m at electrodes 55 to 455 m which is spread under the coal seam and above the clay layer. And the third layer is at a depth of ± 518 m with a resistivity of $\sim 1060 \Omega\text{m}$ which is interpreted as a conglomerate layer.

Table 8. Distribution of lignite coal.

Place the electrodes	Depth (m)	Resistivity (Ωm)
55 - 505	96.26	12 - 30

Track 8 Yati

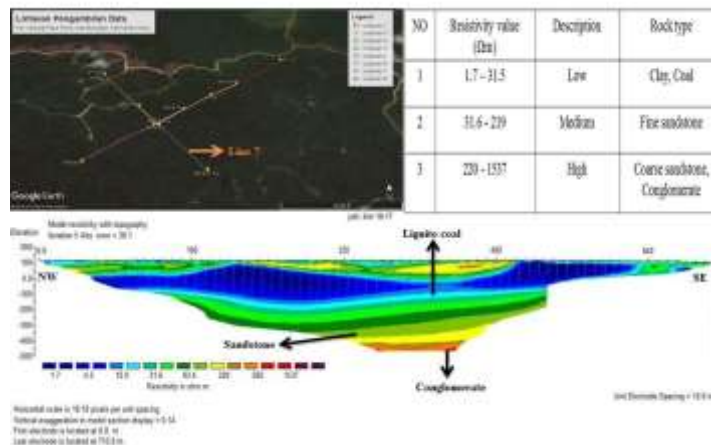


Figure 11. Cross section of the inversion of the path 8 Yati.

From the cross-sectional image above, it can be seen that at the bottom layer there is a high resistivity ranging from $1569 \Omega\text{m}$ (red color) at a depth of 518 m which is

interpreted as conglomerate rock. Then on the top layer of the conglomerate, there is a medium resistivity layer with a resistivity of $\sim 200 \Omega\text{m}$ (yellow color) which is interpreted as a sandstone layer at a depth of $\pm 420 \text{ m}$. After that, the layer with a resistivity $> 10 \Omega\text{m}$ is interpreted as a low type coal seam at electrodes 145 to 445 m with a depth of 21.42 m and a thickness of $\pm 20 \text{ m}$.

Table 9. Distribution of lignite coal.

Place the electrodes	Depth (m)	Resistivity (Ωm)
145 - 445	21.42	10.1 - 27

Based on the interpretation of each path above, it can be seen that there are variations in the resistivity values of rocks in the study area as shown in table 10.

Table 10. Interpretation of the resistivity value of the research area.

Resistivity value (Ωm)	Information	Rock type
10 – 30	Low	Lignit Coal
104 – 1506	Middle	Fine sandstone and coarse sandstone
1506 - 6400	High	Conglomerat

From the results above, it can be seen that the geoelectric resistivity pole-pole configuration method can be used to determine the distribution of coal with a depth of up to 300 m compared to using the induced polarization geoelectric method which reaches a depth of 30 m [5].

Coal Distribution Analysis

After interpreting the results of the 2d resistivity inversion on each track, it can be seen the estimation of the distribution pattern of coal in the research location based on the xyz data from the Res2dinv inversion using the Rockworks 15 Software. Rockworks 15 software is software that can be used to estimate mineral reserves from point data drill used [10]. In making 3d modeling at Rockworks this research uses Res2dinv inversion xyz data which has been interpreted according to regional geology and made into drill point data.

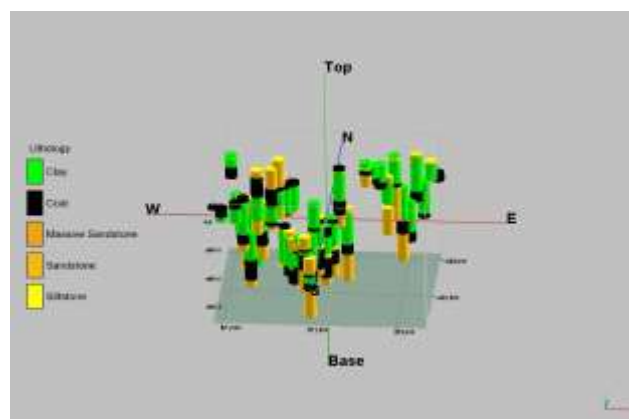


Figure 12. 3D block drill points cross section 1.

This modeling uses 44 drill point data with a drill point distance of 50 meters which is composed of clay, coal, sandstone and silt lithology. From the results of the modeling of the block 1 lithology section above, it is known that the dominant lithology in the study area is clay by 38% with a volume of 419,000,000 tons and coal lithology as the research target of 25% with a volume of 270,600,000 tons of the total existing lithology.

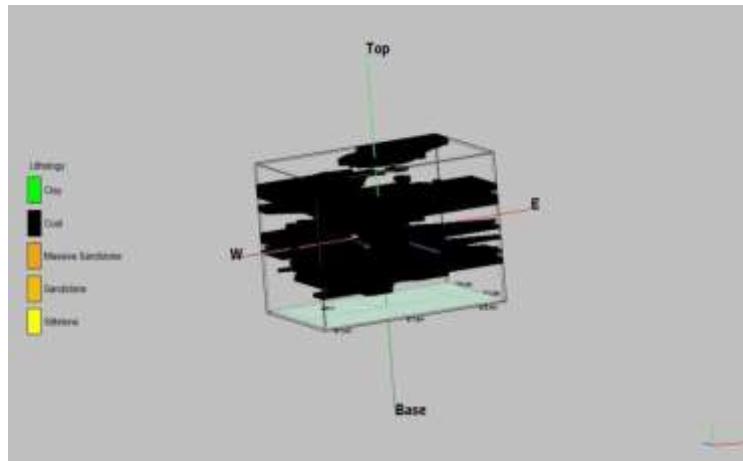


Figure 13. 3D cross-section of coal lithology block 1.

The image above is the distribution of coal obtained from 3D modeling of block 1 at Rockworks. It can be seen that the direction of the distribution of coal is from west to east to north to south. In the section above, the coal depth starts from a depth of 4.2 m at drill point LE2-405 and ends at drill point LY8-445 at a depth of 329 m. From the picture above, it can also be seen that the distribution of coal in the study area is actually only found in the upper and lower layers of coal. Below is a modeling image of the top layer of coal in block 1.

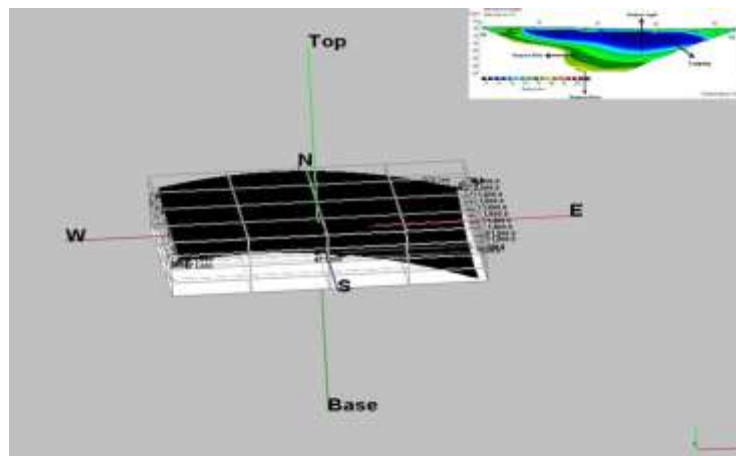


Figure 14. Block top layer coal seam.

Coal Seam Continuity

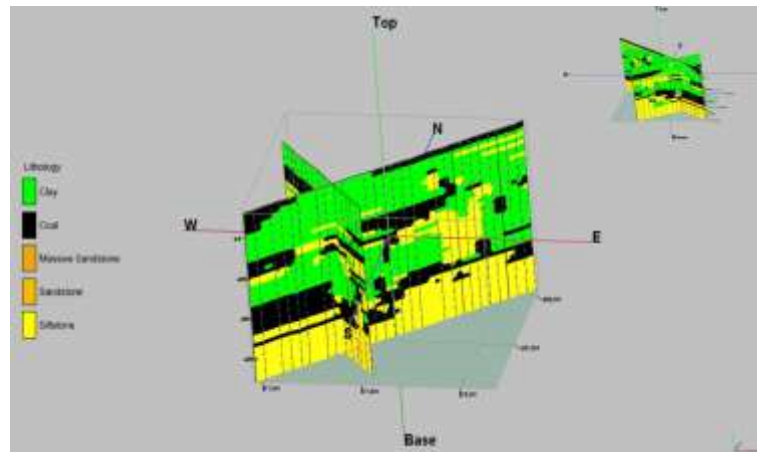


Figure 15. Block lithology continuity display.

The picture above is a combination of paths 1, 2, 3 which intersect with paths 7, 8 in block 1. Based on the image above, it can be seen the continuity of the intersection of each path. The point of intersection is on track 3 and line 7, the coal seam can be seen continuing from the southwest to track 1 which is in the northeast. The continuity of this coal seam is only found at the bottom of the coal layer which is at a depth of 258 m.

CONCLUSION

Based on the interpretation results that have been carried out in the previous chapter by correlating resistivity data and geological data in the Tanjung Palas Timur District, North Kalimantan Province, in general it can be concluded as follows:

1. Characteristics of the coal seam identified in the Tanjung Palas Timur District, North Kalimantan Province, which has a low resistivity value because it is flanked by clay rocks above and sandstones below. So, when viewed from the classification of coal types, the type of coal in this research area is included in the type of lignite coal.
2. The resistivity value of the coal in the study area as seen from the 2D cross-section that has been correlated with regional geology, rock resistivity tables, and the resistivity values of previous studies were obtained from track 1 with a range of 1.4 m – 11.9 m, track 2 ety 1.3 m - 12.4 m, track 2 3 ety 1.3 m - 12.5 m, track 7 yati 1.7 m - 12 m, track 8 yati 1.3 m - 10.1 m which is incorporated in block 1, while track 4 languishes from 2.3 m - 30.7 m, track 5 languishes 6.6 m - 20.4 m, track 6 languishes 4.3 m - 49.1 m which is incorporated in block 2. It is concluded that block 1 has a coal resistivity value of 10 m - 12.5 m with a depth ranging from 4.2 m to 293 m and a thickness of 17.22 m to 30 m, while block 2 has a resistivity value of 20.4 m - 49 m with a depth of 113 m to 153 m and a thickness of 39 m to 60 m
3. Based on the 3D modeling of the coal distribution pattern using Rockworks Software, we can see continuity in block 1 of the research area. This continuity can be seen from the southwest on track 3 to the northeast on track 1 which is in the bottom layer of coal at a depth of 258 m.

REFERENCES

- [1] Anonim, *Sumber Daya Batubara (Tinjauan Lengkap Mengenai Batu Bara)*. World Coal Institute, 2005.
- [2] T. Y. dan S. Widodo, "Identifikasi Penyebaran Dan Ketebalan Batubara Menggunakan Metode Geolistrik Resistivitas (Studi Kasus Daerah X Kabupaten Kutai Kertanegara Kalimantan Timur)," *Berk. Fis.*, vol. 11, no. 2, pp. 59–66, 2008.
- [3] Hamid Umar, "Analisis Potensi dan Cadangan Batubara dengan Metode Geolistrik Resistivity di Daerah Massenrengpulu Kecamatan Lamuru Kab.Bone, Prov.Sulawesi Selatan," vol. 6, pp. 978–979, 2012.
- [4] E. Azizah and A. Basid, "Aplikasi Metode Geolistrik untuk Mengetahui Sebaran Batubara di Kabupaten Tulungagung Jawa Timur," vol. 2, no. 1, pp. 51–58, 2020.
- [5] M. Z. Muhlisin, "Identifikasi Sebaran Batubara Menggunakan Metode Geolistrik Polarisasi Terinduksi (IP) (Studi Kasus Daerah Klatak Kecamatan Besuki Kabupaten Tulungagung)," 2019.
- [6] J. M.Reynolds, *An Introduction to Applied and Environmental Geophysics*. John Wiley & Sons Ltd, 1997.
- [7] M. . Loke, *Tutorial: 2-D and 3-D electrical imaging surveys By*. 2004.
- [8] W. M. Telford, *Applied Geophysics, Second Edition*, 1990th ed. Cambridge University Press.
- [9] P. Kearey, *An Introduction to Geophysical Exploration*, 3rd ed. Blackwell Science, 2002.
- [10] D. Adrian and B. S. Mulyatno, "Identifikasi Dan Estimasi Sumber Daya Batubara Menggunakan Metode Poligon Berdasarkan Intepretasi Data Logging Pada Lapangan "Ada", Sumatera Selatan," *J. Geofis. Eksplor.*, vol. 4, no. 1, pp. 94–111, 2020, doi: 10.23960/jge.v4i1.8.

Identification of Potential Waste Fluid Contamination with Geoelectric Method in Tebing Tinggi Subdistrict, West Tanjung Jabung Regency, Jambi

Salsabila Octara Sumaryanto^{1,†}, Nur Hidayat²

¹Physics Study Program, Faculty of Sciences and Technology, State Islamic University Syarif Hidayatullah Jakarta, Ir. H. Juanda Rd, No. 95, Cempaka Putih, Ciputat, South Tangerang, Banten 15412, Indonesia

²Center of Technology for Disaster Risk Reduction, Agency for the Assessment and Application of Technology (BPPT), Geotech Building 820, PUSPIPTEK Area, Serpong, South Tangerang, Banten 15314, Indonesia

†octarasalsabila@gmail.com

Submitted: December 2021; Revised: April 2022; Approved: June 2022; Available Online: October 2022

Abstract. In the study area of Tebing Tinggi Subdistrict, Tanjung Jabung Barat Regency, Jambi Province, there are several companies engaged in the manufacturing, agriculture, and plantation industries. This company uses the Pengabuan River for transportation. Therefore, the study area has the potential to be contaminated by the waste fluid produced by the company. In this study, the Wenner array resistivity geoelectric method was used because this array can detect potential pollution in shallow subsurface. Data processing is done by inversion process using Res2Dinv software to get 2D modelling and Voxler to get 3D modelling. Based on the 2D modelling, it is identified that the contamination is on lines 1, 2, and 4 with a resistivity range of ± 0.059 -2 Ω m. Also, in the study area, it is identified that there are alternating tuffaceous claystone, claystone, tuffaceous sandstone, sandstone, and shallow aquifer. Based on the 3D modelling, it is identified that there is a potential continuity of contamination between line 3 and line 4, which is at a distance of 0-8 m to the east from line 4 to line 3.

Keywords: *Geoelectric Resistivity Method, Pengabuan River, Tebing Tinggi Subdistrict, Waste Fluid Contamination, Wenner Array*

DOI: [10.15408/fiziya.v5i1.23647](https://doi.org/10.15408/fiziya.v5i1.23647)

INTRODUCTION

Water contamination can occur if foreign substances seep into the soil surface entering through the soil pores. This results in causing the soil to become saturated and will cause disturbances to groundwater. In Tebing Tinggi Subdistrict there are several companies engaged in the manufacturing, plantation, and forestry industries. In the transportation route, this company uses the Pengabuan River which is located close to the company's location as one of the transportation routes to transport industrial raw materials [1]. In this case, it is necessary to carry out an investigation to determine the potential for contamination by waste fluid below the ground surface. One of the

geophysics method to determine the contamination of waste fluid is the geoelectric resistivity method.

The geoelectric resistivity method uses a current source that is injected into the ground through an electrode. Several studies using the geoelectric resistivity method have been studied for surveys of contamination by waste, namely Suhendra (2006), Sri et al (2007), Rahmatun et al (2019). Suhendra (2006) conducted a study in the laboratory by injecting waste into clay, Sri et al (2007) conducted a study in the MIPA Basic Laboratory area, Rahmatun et al (2019) in their study conducted a study in a village located in Mojokerto which is surrounded by several industry companies. Therefore, in this study, the geoelectric resistivity method with the Wenner array is used to determine the potential for contamination by waste fluid which is characterized by the presence of subsurface material anomalies in Tebing Tinggi Subdistrict area.

Regional Geological of the Study Area

Tebing Tinggi Subdistrict is located in West Tanjung Jabung Regency, Jambi. Based on regional geology, Tebing Tinggi Subdistrict is known to have three formations, namely Alluvium (Qa) which is composed of boulders, gravel, sand, and mud with plant remains where the composition is Holocene in age. Then the Swamp Sediment (Qs) which is composed of silt, mud, clay, sand, and plant remains where the composition is Holocene in age. Furthermore, there is the Kasai Formation (Qtk) which is composed of tuffaceous sandstone, quartz sandstone, tuffaceous claystone, conglomerate of various materials, tuff, gravel, crushed wood where this formation is Pleistocene-Pliocene age [2].

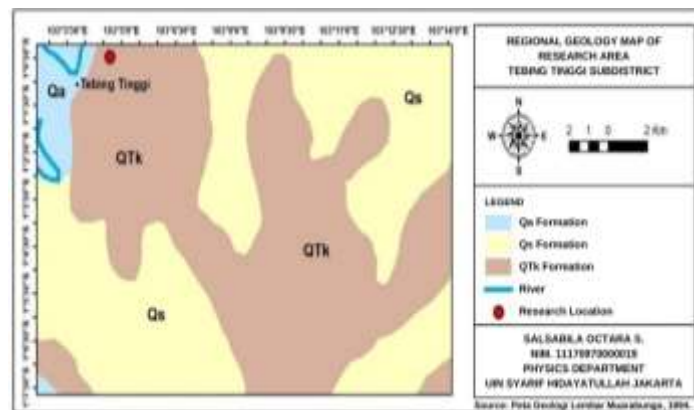


Figure 1. Regional Geological Map of Tebing Tinggi Subdistrict [2].

Waste Contamination

Waste contamination can occur if foreign substances (waste) enter the soil and contaminate the soil. According to [3], liquid waste can be divided into 3, namely industrial liquid waste, domestic liquid waste, and wastewater mixed with groundwater. Industrial liquid waste is liquid waste generated from industrial activities. Domestic liquid waste is liquid waste generated due to daily activities. Meanwhile, wastewater mixed with groundwater can occur if it rains, and then rainwater seeps into the ground and becomes groundwater, then the groundwater meets wastewater which causes groundwater to mix with waste.

The contamination that is not visible below the surface can be investigated by geophysical methods. One of the good geophysical methods used for the investigation of contamination by waste fluid at the subsurface is the geoelectric resistivity method.

Geoelectric Resistivity Method

In the resistivity method, electric current is used which is injected under the surface using an electrode where a potential difference will be generated which will be measured on the surface. The anomaly of the measured potential difference will illustrate the subsurface conditions [4].

Based on the resistivity method, the earth is considered homogeneous isotropic, which means that the flow of electric current in the earth is the same in all directions and each layer of the earth has the same resistivity. In fact, the earth has layers with different resistivities, so the measured resistivity is not the true resistivity, but the apparent resistivity (ρ_a) [5]. The apparent resistivity can be formulated by:

$$\rho_a = K \frac{\Delta V}{I} \tag{2}$$

Where K is the geometric factor of the electrode array used, ΔV (Volt) is the measured potential difference, and I (A) is the measured current.

Table 1. Resistivity of Some Rocks.

Rocks	Resistivity (Ωm)
Sea water	0.2
Groundwater	0.5 - 300
Clays	1 - 100
Alluvium	10 - 800
Sands	1 - 1000
Gravel	100 - 600
Sandstones	200 - 8×10^3

In the resistivity method, there are several electrode arrays, namely Wenner array, Schlumberger array, Dipole-dipole array, Pole-dipole array, and Pole-pole array. Wenner array is good for subsurface investigation for contamination by waste fluid because the Wenner array is good for shallow subsurface surveys and can map shallow subsurface materials well.

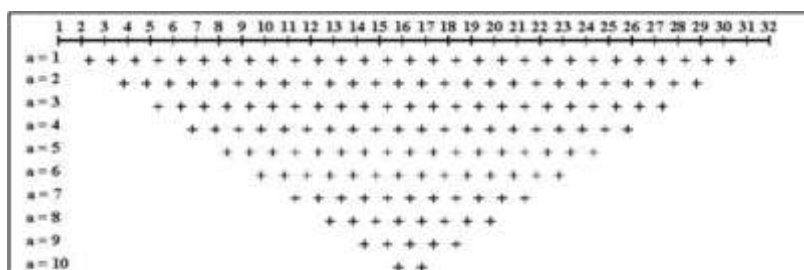


Figure 2. Wenner Array Data Distribution [8].

METHOD

The study was conducted in Tebing Tinggi Subdistrict, West Tanjung Jabung Regency, Jambi using the geoelectric resistivity method. The data used is secondary data belonging to the Center of Technology for Disaster Risk Reduction (PTRRB), Agency for

the Assessment and Application of Technology (BPPT) in the form of apparent resistivity and topography data. Secondary data processing starts from January-March 2021.

Data processing was carried out using Res2Dinv software in 2D modelling to determine subsurface conditions and identify subsurface materials in the study area that indicated being contaminated by waste fluid. Meanwhile, to determine the potential for continuous contamination by waste fluid, 3D modelling using Voxler software was carried out on two parallel lines.

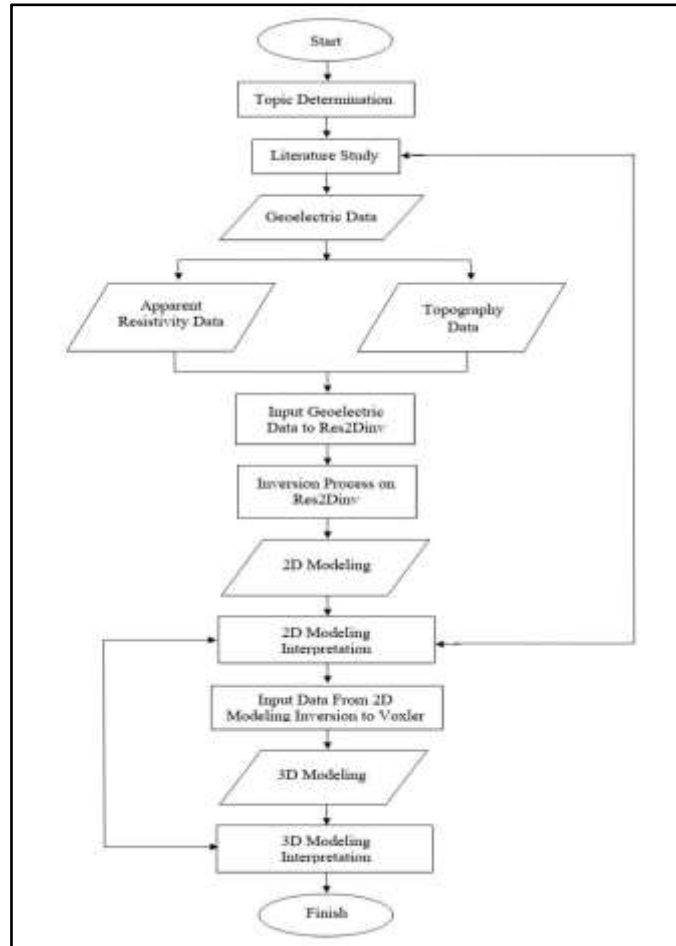


Figure 3. Flowchart of Study Stages.

RESULT AND DISCUSSIONS

This study was conducted in Tebing Tinggi Subdistrict, Tanjung Jabung Barat Regency, Jambi with 5 lines, namely with a length of line 1 and line 2 along 47 m with an electrode spacing of 1 m, and line 3 to line 5 along 24 m with electrode spacing of 0.5 m. In interpreting the results of the subsurface modelling to determine the distribution of contamination, calibrations were carried out using the results of 2D modelling, rock resistivity tables, regional geological maps of the study area, and previous studies.



Figure 4. Measurement Line Location.

2D Modeling Results

The subsurface material generated in the 2D resistivity modelling, shows the area that contaminated will have a low resistivity.

Line 1

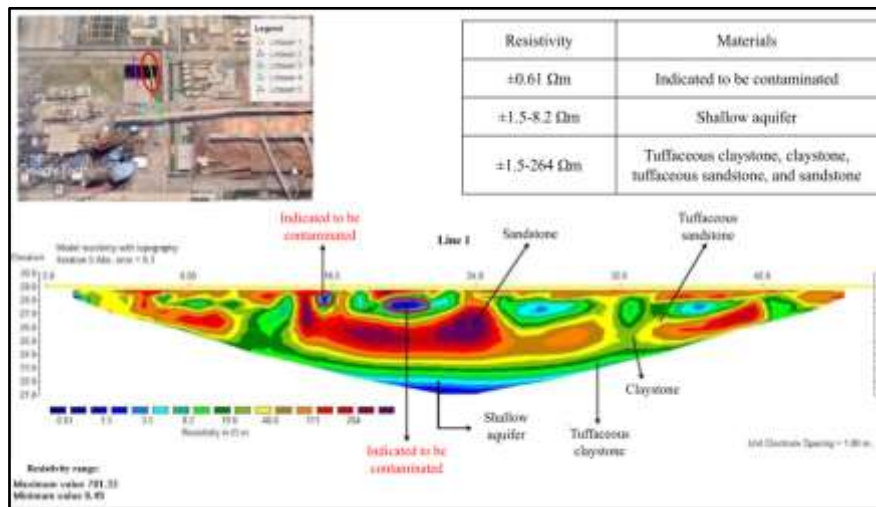


Figure 5. 2D Modeling Results in Line 1.

Based on fig. 5 the results of the 2D resistivity modelling, it can be seen that there are layers of indicated tuffaceous claystone, claystone, tuffaceous sandstone, and sandstone adjacent to each other with a resistivity range of $\pm 1.5-264 \Omega m$. In line 1, there is a material with low resistivity which indicates an anomaly, which are at a line distance of 15.5 m at a depth of 0.5-1 m and a line distance of 19-21 m at a depth of 1-1.5 m. This material with low resistivity is indicated to be contaminated by waste fluid, with a resistivity of $\pm 0.61 \Omega m$. In addition, in line 1 there are also identified shallow aquifer, with a resistivity range of $\pm 1.5-8.2 \Omega m$. Oil and gas are natural resources that are mostly used to meet daily needs and as a contributor to the country's foreign exchange. However, as human needs increase in their daily activities, the consumption of oil and gas energy increases. Meanwhile, the energy sources needed are dwindling due to uncontrolled energy exploitation. Therefore, alternative energy is needed as a substitute for fuel oil and gas, one of which is coal.

Line 2

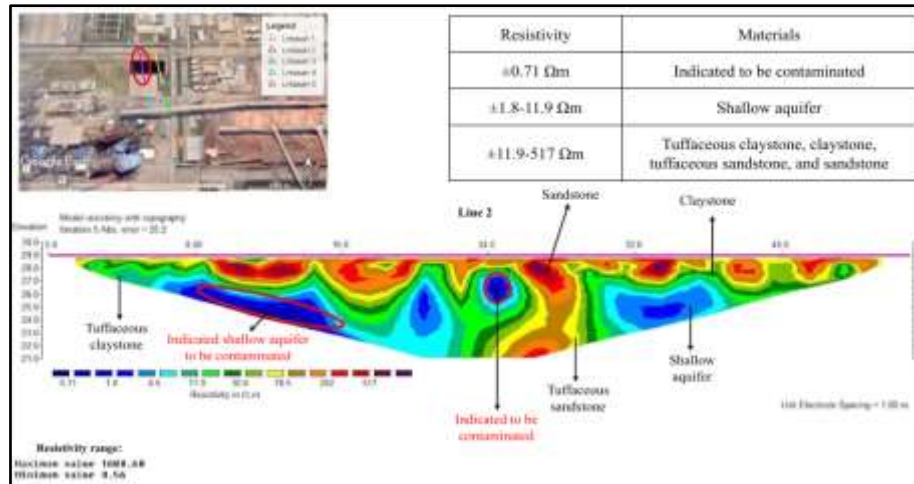


Figure 6. 2D Modeling Results in Line 2.

Based on fig. 6 the results of the 2D resistivity modelling, it can be seen that there are layers of indicated tuffaceous claystone, claystone, tuffaceous sandstone, and sandstone adjacent to each other with a resistivity range of $\pm 11.9-517 \Omega m$. In line 2, there is a material with low resistivity which indicates an anomaly, which are at a line distance of 8-15 m at a depth of 2-6 m and a line distance of 24-25 m at a depth of 1.5-2.5 m. This material with low resistivity is indicated to be contaminated by waste fluid, with a resistivity of $\pm 0.71 \Omega m$. In this contaminated layer, it is indicated that the waste contaminates the shallow aquifer which is at a line distance of 8-15 m at a depth of 2-6 m. In addition, in line 2 there is also identified another shallow aquifer with a resistivity range of $\pm 1.8-11.9 \Omega m$.

Line 3

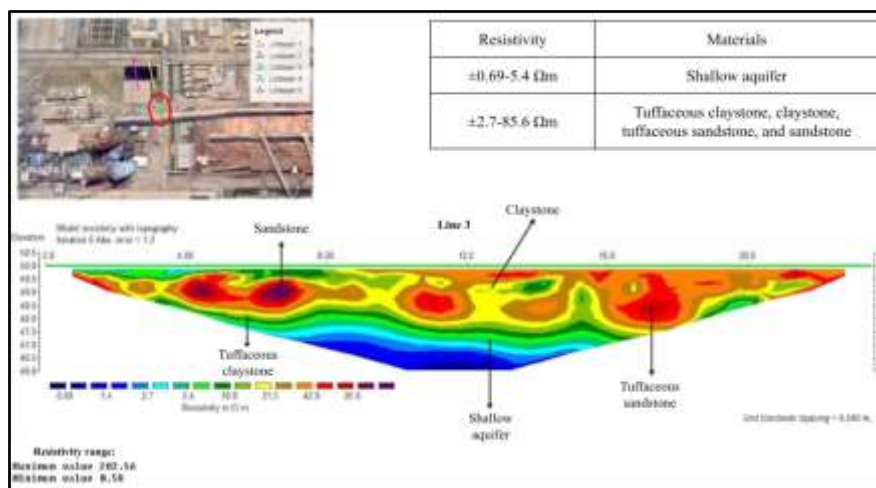


Figure 7. 2D Modeling Results in Line 3.

Based on fig. 7 the results of the 2D resistivity modelling, it can be seen that there are layers of indicated tuffaceous claystone, claystone, tuffaceous sandstone, and sandstone adjacent to each other with a resistivity range of $\pm 2.7-85.6 \Omega m$. In addition, in line 3 there are also identified shallow aquifer with a resistivity range of $\pm 0.69-5.4 \Omega m$. In

line 3, no identified subsurface material anomaly that indicates contamination by waste fluid.

Line 4

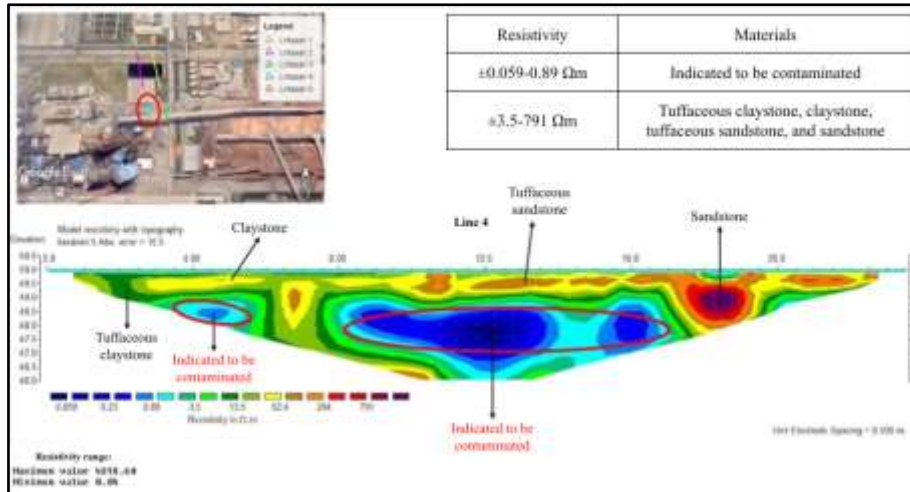


Figure 8. 2D Modeling Results in Line 4.

Based on Fig 8 the results of the 2D resistivity modelling, it can be seen that there are layers of indicated tuffaceous claystone, claystone, tuffaceous sandstone, and sandstone adjacent to each other with a resistivity range of $\pm 3.5-791 \Omega m$. In line 4, there is a material with low resistivity which indicates an anomaly, which are at a line distance of 3-5.5 m at a depth of 1-2.5 m and a line distance of 8-17 m at a depth of 1-3.5 m. This material with low resistivity is indicated to be contaminated by waste fluid with a resistivity range of $\pm 0.059-0.89 \Omega m$.

Line 5

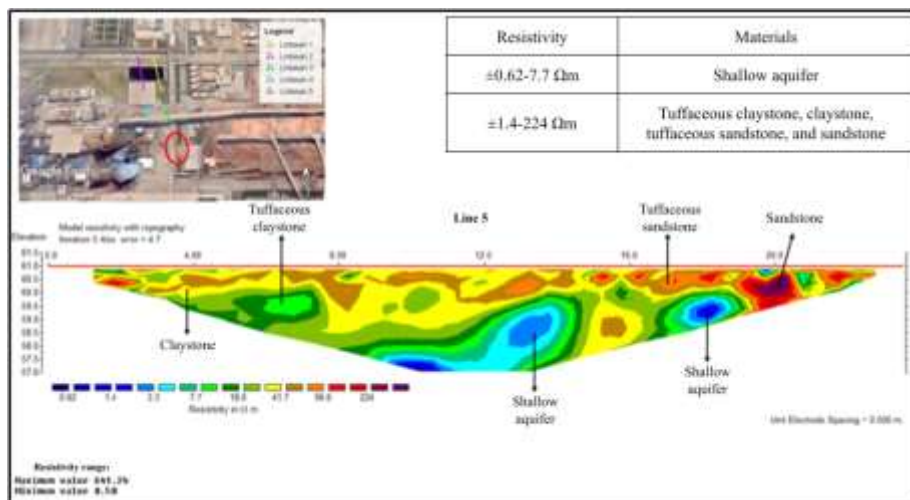


Figure 9. 2D Modeling Results in Line 5.

Based on fig. 9 the results of the 2D resistivity modelling, it can be seen that there are layers of indicated tuffaceous claystone, claystone, tuffaceous sandstone, and sandstone adjacent to each other with a resistivity range of $\pm 1.4-224 \Omega m$. In addition, in

line 5 there are also identified shallow aquifer with a resistivity range of $\pm 0.62-7.7 \Omega m$. In line 5, no identified subsurface material anomaly that indicates contamination by waste fluid.

Based on the results of the 2D modelling of the five lines, the classification of the material based on the range of resistivity of the material is presented in table 2.

Table 2. Classification of Subsurface Materials in Study Area Based on Resistivity Values.

Resistivity Range (Ωm)	Materials
$\pm 0.059-2$	Contaminated material
$\pm 0.62-11.9$	Shallow aquifer, tuffaceous claystone
$\pm 1.4-100$	Claystone, tuffaceous sandstone
$\pm 200-4318.6$	Sandstone

3D Modeling Results

The 3D modelling in Voxler only focuses on the potential of continuous contamination by waste fluid, so that the resistivity of the subsurface material is limited to only the range of 0-100 Ωm , where for materials with resistivity $> 100 \Omega m$ are marked with the same color as materials with resistivity of 100 Ωm . The 3D modelling results correlated with the 2D modelling results. From 3D modelling, to find out the potential for continuous contamination, it is divided into 6 sections for 2 lines that are parallel (line 1 and line 2, line 3 and line 4), each section is 4m apart, so that it is known at what distance there is potential for continuous contamination from each line.

Line 1 and Line 2

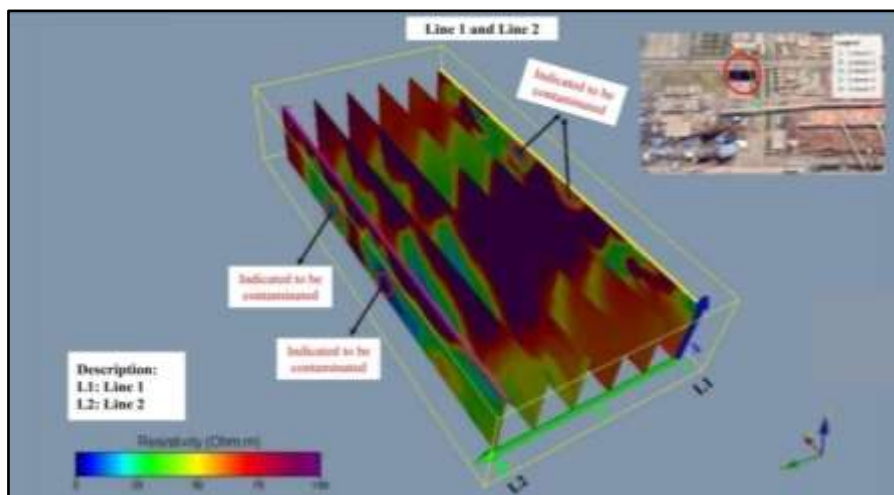


Figure 10. Line 1 and Line 2 Combined 3D Modeling.

Based on Fig 10, areas with indications of contamination are marked with dark blue color and low resistivity, which for the combination of line 1 and line 2 with a resistivity range of $\pm 0-0.71 \Omega m$. Based on Figure 10, there is a possibility of continuous contamination from line 2 to line 1 seen from the location and pattern of contamination on each line, but from the 3D modelling carried out there is no continuous contamination in the area between line 1 and line 2. This is because data processing in the area between line 1 and line 2 is done only with estimates by software, so the resulting model is less

accurate. Therefore, it is necessary to collect data in the area between line 1 and line 2 to obtain a more accurate 3D model to determine the continuity of contamination.

Line 3 and Line 4

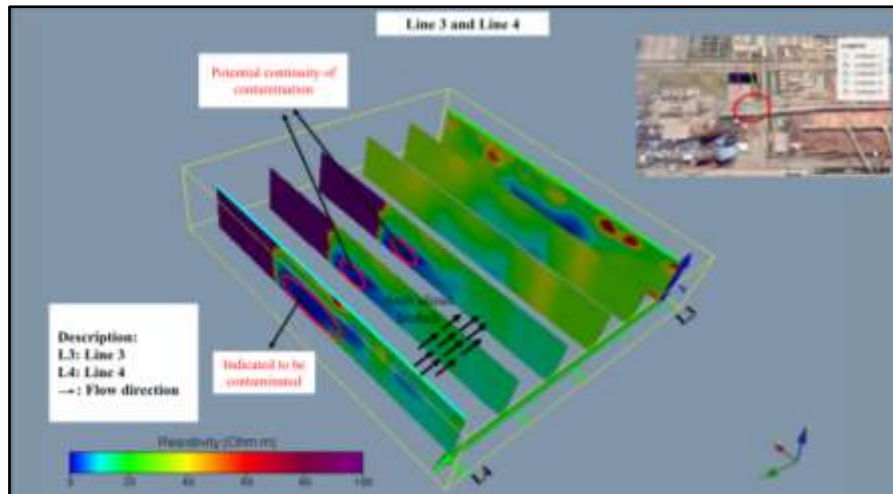


Figure 11. Line 3 and Line 4 Combined 3D Modeling.

Based on the fig. 11, areas with indications of contamination are marked with dark blue color and low resistivity, which for the combination of line 3 and line 4 with a resistivity range of $\pm 0-0.89 \Omega m$. In the 3D modelling that has been carried out for the combination of line 3 and line 4, it is found that there is a potential continuity of contamination which is indicated by a low resistivity or dark blue part between the two lines. Indications of continuous contamination by waste fluid are identified as being at a distance of 0-8 m to the east from line 4 to line 3, with the location of contamination being at a line distance of $\pm 12-14.5$ m and at a depth of $\pm 2-3.5$ m. This contamination indication is indicated to be a continuation of the contamination on line 4.

Based on the results of the 3D modelling between the 2 parallel lines, the detailed interpretation of the potential for continuous contamination based on the 3D modelling is presented in table 3.

Table 3. Interpretation of the Potential for Continuous Contamination Based on 3D Modeling.

Line	Continuity	Description
1 and 2	Indicated exists	It is indicated that there is continuity, but it is not seen in the 3D modelling results. More study is needed to determine the continuity of contamination between line 1 and line 2.
3 and 4	Exists	Continuity of contamination is found at a distance of 0-8 m from line 4 to line 3 at a line distance of $\pm 12-14.5$ m and at a depth of $\pm 2-3.5$ m.

CONCLUSION

Based on the study that has been done, the following conclusions are:

1. The results of the 2D modeling on the five lines show that under the surface of the study area there are alternating tuffaceous claystone, claystone, tuffaceous sandstone, and sandstone. In addition, shallow aquifer is identified, which on lines 1, 2, 3, and 5. In the study area, an anomaly of subsurface material that indicated contamination is identified and it has a resistivity ranging from $\pm 0.059-2 \Omega\text{m}$ which the contamination is identified to be on lines 1, 2, and 4. In addition, the 2D modeling shows that there is a certain pattern in the material that is indicated to be contaminated.
2. Based on the 3D modeling, it is identified that there is an indication of continuous contamination between line 3 and line 4. This continuity is indicated to be a continuation of the contamination on line 4, which is at a distance of 0-8 m to the east from line 4 to line 3 at a distance line of $\pm 12-14.5$ m and a depth of $\pm 2-3.5$ m.

REFERENCES

- [1] U. Syamsiatun, "Sungai Pengabuan, Urat Nadi Kehidupan," Qureta, 2019. <https://www.quireta.com/post/sungai-pengabuan-urat-nadi-kehidupan> (accessed Jan. 09, 2021).
- [2] T. O. Simandjuntak, T. Budhitrisna, Surono, S. Gafoer, and T. C. Amin. "Peta Geologi Lembar Muarabungo." 1994.
- [3] Y. Gunawan, "Peluang Penerapan Produksi Bersih Pada Sistem Pengolahan Air Limbah Domestik Waste Water Treatment Plant #48, Studi Kasus di PT Badak NGL Bontang," Universitas Diponegoro, 2006.
- [4] P. Kearey, M. Brooks, and I. Hill, An Introduction to Geophysical Exploration, 3rd ed. Blackwell Publishing, 2002.
- [5] I Nengah Simpen, "Modul Praktikum Metoda Geolistrik," 2015.
- [6] W. M. Telford, L. P. Geldart, and R. E. Sheriff, Applied Geophysics, 2nd ed. Cambridge: Cambridge University Press, 1990.
- [7] Miswar, "Metode Geolistrik Resistivitas Di Kawasan Industri Makassar (KIMA)," Universitas Islam Negeri Alauddin Makassar, 2017.
- [8] A. T. Batayneh, "2D Electrical Imaging of an LNAPL Contamination, Al Amiriyya Fuel Station, Jordan," J. Appl. Sci., vol. 5, no. 1, pp. 52–59, 2005, doi: 10.3923/jas.2005.52.59.

Correlation between Scattering Matrix, Return Loss and Interface Reflection Loss in Nicolson Rose Wear Approximation

Wakid Ali Muntoha¹, Adam B. Cahaya^{1,†}, Azwar Manaf¹

¹Department of Physics, FMIPA, University of Indonesia, Kampus UI Depok 16424 Indonesia

[†]adam@sci.ui.ac.id

Submitted: December 2021; Revised: April 2022; Approved: June 2022; Available Online: October 2022

Abstract. The phenomenon behind the absorption of electromagnetic waves by absorbing materials is resonance phenomenon. When there is a similarity between the value of the impedance of electromagnetic waves in the air and the impedance of the material, the absorption of energy by the material is maximized. The phenomenon is measured using an auxiliary instrument, namely the Vector Network Analyzer. This instrument is very effective for calculating the absorption value of electromagnetic waves. However, the Vector Network Analyzer instrument which is mostly available in Indonesian research institutions cannot directly display the reflection loss of the electromagnetic wave absorbing material. An effective method that is effective for calculating the absorption in electromagnetic wave absorbing material is Nicolson Rose Wear method. In this article, we design a computational tool based on Nicolson Rose Wear approximation to calculate the reflection loss values from scattering matrix and comparing it with return loss, which is often mistook as reflection loss.

Keywords: Nicolson-Ross-Wear, Permeability, Permittivity, Reflection Loss

DOI: [10.15408/fiziya.v5i1.22353](https://doi.org/10.15408/fiziya.v5i1.22353)

INTRODUCTION

Electromagnetic wave absorbance occurs when an electromagnetic wave from air enters a radar absorbing material. The absorption mechanism of electromagnetic waves is a resonance process between the impedance value, which are the ratio of the magnitude of electric field and magnetic field, of electromagnetic waves of the air and the impedance of the material [1]. If the impedance values of the two mediums are the same, maximum absorption will occur, known as matching impedance [2]. Since electromagnetic waves are a combination of electric and magnetic waves, the two values can vary significantly over even a small range of frequencies. If the permittivity and permeability of the complex are known at each frequency, the effect of EM waves on the material can be known [3].

In order to achieve necessary characteristics to function as an electromagnetic wave absorbing material, experimental research on radar absorbing materials involve material structure engineering of unit cell structure through partial atomic substitution [4]. The characterization of the material is carried out using an auxiliary instrument, namely the Vector Network Analyzer (VNA) [5]. However, most of the VNA instruments that are available in Indonesian research institutions only measures scattering matrix [6]

$$S = \begin{pmatrix} S_{11} & S_{12} \\ S_{21} & S_{22} \end{pmatrix}, \quad (1)$$

where $|s_{11}|^2$ and $|s_{22}|^2$ are the reflection rates of incoming waves from the opposite sides, $|s_{21}|^2$ and $|s_{12}|^2$ are the transmission rates. The return loss of a sample is simply the logarithmic value of the reflection rates in dB [7].

$$\text{return loss} = 20 \ln|s_{11}|. \quad (2)$$

This value is often misunderstood as reflection loss due to similar abbreviation [7]. Reflection loss is characterized by reflection rate Γ of the interface, which is related to the impedance of the

$$\text{reflection loss} = 20 \ln|\Gamma|, \quad (3)$$

where $|\Gamma| < 1$.

However, reflection loss is associated with the reflection of only one side of the interface only, not of the whole sample. An effective method that is effective for calculating reflection loss from the absorption in electromagnetic wave absorbing material is Nicolson Rose Weir method [8].

This research aims to analyze those physical quantities from the measured scattering matrix using Nicolson Ross Weir algorithm. Furthermore, we develop a graphical user interface for easy utilization. This interface can be expected to support research and applications in the RADAR wave area [9].

COMPUTATIONAL METHODS

NRW Algorithm

Nicolson Ross Weir (NRW) is a calculation method to get the permeability and permittivity values from the scattering matrix [10]. This technique can be used on dielectric materials. This theory is used to analyze material scattering events and is related to the permittivity and permeability of the material [11]. While this method has advantages and disadvantages compared to other methods, it has fast convergence and can be used for wide range of materials. Table 1 lists the type of materials that are often used in NRW method

Table 1. Materials that can be measured using NRW method [12].

Materials	Length	Magnetic properties	Measurement methods	Speed	Accuracy
Lossy solids	Short	Non-magnetic	Transmission/reflection line (TR)	Fast	Medium
Lossy solids	Short	Magnetic	TR	Fast	Medium
High temperature solids	Large / flat	Non-magnetic	Free space	Fast	Medium

The NRW method measure the reflection loss and reflection rate Γ

$$\Gamma = \frac{Z-Z_0}{Z+Z_0}, \quad (4)$$

from the resonance of the impedance in the air, which can be assumed to be equal to the impedance of vacuum $Z_0 \approx 377\Omega$ [13] and the impedance of the radar absorbing material $Z = Z_0\sqrt{\mu_r/\epsilon_r}$, where μ_r and ϵ_r are relative permeability and permittivity, respectively. In NRW, Γ is related to the scattering matrix

$$\Gamma = x \pm \sqrt{x^2 - 1}, \quad (5)$$

$$x = \frac{s_{11}^2 - s_{21}^2 + 1}{2s_{11}} \quad (6)$$

This computational method is the following implemented in using the flowchart in Figure 1.

Beside reflection loss, we can also obtain μ_r and ϵ_r for material with known with d and cut-off wavelength λ_c .

$$\mu_r = \frac{1+\Gamma}{\Delta(1-\Gamma)\sqrt{\frac{1}{\lambda_0^2} - \frac{1}{\lambda_c^2}}}, \quad (7)$$

$$\epsilon_r = \frac{\lambda_0^2}{\mu_r} \left(\frac{1}{\lambda_c^2} - \left(\frac{1}{2\pi d} \ln \left(\frac{1}{T} \right) \right)^2 \right), \quad (8)$$

where,

$$\frac{1}{\Delta} = -\frac{1}{2\pi d} \ln T = -\frac{1}{2\pi d} \ln \frac{s_{11} + s_{21} - \Gamma}{1 - (s_{11} + s_{21})\Gamma} \quad (9)$$

These equations are implemented in a graphical user interface that can be accessed openly in azwaradam.com in experiment mode.

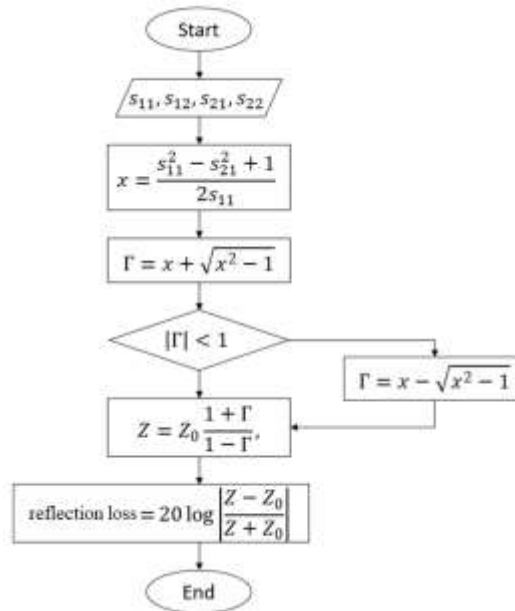


Figure 1. NRW algorithm for reflection loss computation.

RESULT AND DISCUSSION

In this experimental mode, before processing the material data that has been taken from the VNA, the program calibration is carried out first to ensure the program runs well. This calibration uses Teflon data where in this calibration the permeability and permittivity values are seen. The value of the permeability and permittivity is expected to be in accordance with the theory where the permeability value is close to $1 + 0.001i$ and the permittivity value is close to $2 + 0.001i$ [14].

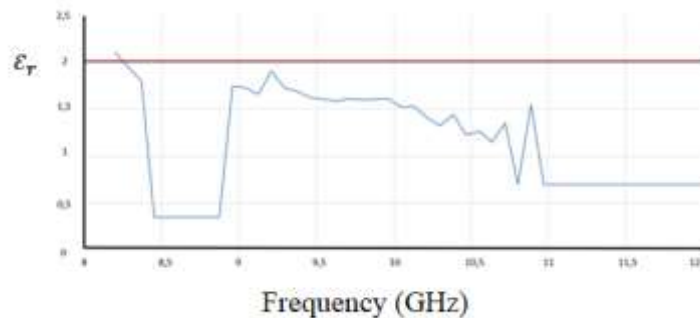


Figure 2. Teflon's permittivity curve as a function of frequency.

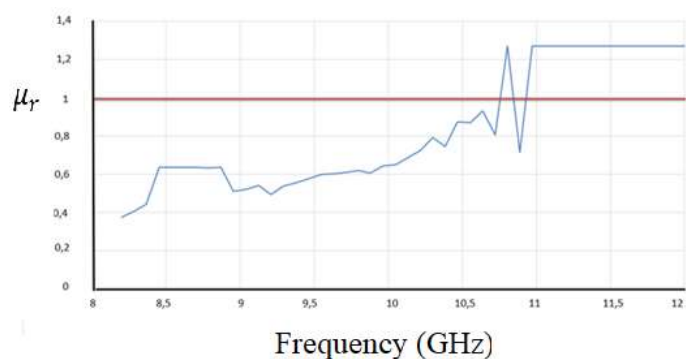


Figure 3. Teflon Permeability Curve on a frequency function.

The results of the calculation of permittivity and permeability can be seen in Figures 2 and 3, respectively. One can see that the value of relative permittivity is close to $2+0.001i$. Similarly, the relative permeability is close to around $1+0.001i$. The values are in accordance with the reference value for Teflon. At the frequency of 10 GHz to 12 GHz, it can be seen that the results of real and imaginary calculations of permittivity and permeability change. We can see that at the 12 GHz frequency there is a huge change. This happens because the value of the scattering parameter changes drastically at the peak frequency changes at 12 GHz. This is because the scattering value used by the VNA tool as the reflection loss value suddenly changes which of course will affect the calculation of permeability and permittivity.

After calibration, the interface was used to calculate the $\text{BaFe}_{12}\text{O}_{19}$ data. The measurement of the scattering parameter can be seen in Figure 4 which shows the reflection loss graph in the frequency function. It can be seen in the figure that the electromagnetic wave range of 8 GHz to 12 GHz is absorbed evenly, it is confirmed in the graph that there is a valley in the frequency range of electromagnetic waves. The frequency valley is formed, at around 9.3 GHz frequency. In this $\text{BaFe}_{12}\text{O}_{19}$ material, one peak is formed, this is similar to the wave crest in the experimental data plotted without taking into account the permeability and permittivity values first. The previous reflection loss value measurements are compared to value in Eq. (1) which is often used for rough estimate of reflection loss. Figure 4 show that our algorithm agrees well with experiment.

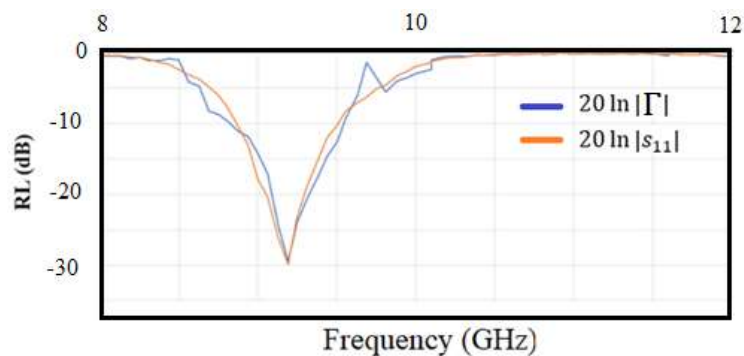


Figure 4. Reflection loss = $20 \ln |\Gamma|$ as a function of frequency of $\text{BaFe}_{12}\text{O}_{19}$. The value is compared with the value of return loss = $20 \ln |s_{11}|$ that often use for rough estimation of Reflection Loss.

We further analyze the scattering matrix parameter value obtained from VNA of a composite material $\text{BaFe}_{12-x}\text{Mn}_{x/2}\text{Ti}_{x/2}\text{O}_{19}$. The composite material has two valleys in 8 GHz, and 11.3 GHz. From the reflection loss graphics of two materials, we can see that reflection loss obtained NRW calculation are consistent with Eq. (1)

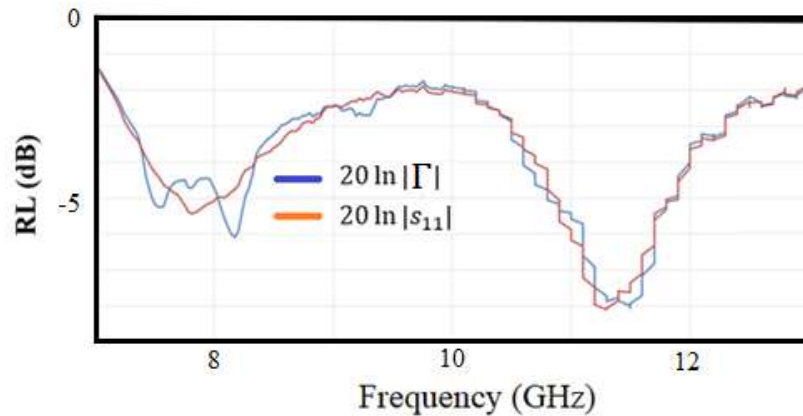


Figure 5. Reflection loss $=20 \ln|\Gamma|$ of a composite material $\text{BaFe}_{12-x}\text{Mn}_{x/2}\text{Ti}_{x/2}\text{O}_{19}$ as a function of frequency. The value is compared with the value of return loss $= 20 \ln |s_{11}|$ that often use for rough estimation of reflection loss.

CONCLUSION

To summarize, we develop a graphical user interface to calculate reflection loss of radar absorbance material using Nicolson Ross Weir algorithm. By using scattering matrix obtained from VNA instrument, we can obtain the reflection loss as a function for frequency in radar absorbance range. The value is similar but not equal to return loss. The graphical user interface can be accessed openly on in azwaradam.com in experiment mode.

The system is validated with the results of the Teflon permeability which is $1+0.001i$ and the Teflon permittivity is $2+0.001i$. The reflection loss value of the $\text{BaFe}_{12}\text{O}_{19}$ experimental data processed from the scattering data has the same graphic tendency as the program results when the frequency is in the range of 9.2 GHz.

ACKNOWLEDGEMENT

The authors thank T. Yana for fruitful discussion and insight about experimental instrument.

REFERENCES

- [1] D. Yuping, M. He, L. Xiaogang, L. Shunhua, and J. Zhijiang, "The microwave electromagnetic characteristics of manganese dioxide with different crystallographic structures," *Phys. B Condens. Matter*, vol. 405, no. 7, pp. 1826–1831, 2010, doi: <https://doi.org/10.1016/j.physb.2010.01.055>.
- [2] F. Costa, M. Borgese, M. Degiorgi, and A. Monorchio, "Electromagnetic Characterisation of Materials by Using Transmission/Reflection (T/R) Devices," *Electronics*, vol. 6, no. 4, 2017, doi: 10.3390/electronics6040095.
- [3] M. V Akhterov, M. V Akhterov, and M. V Akhterov, "Microwave Absorption in Nanostructures." 2010.
- [4] L. Yang, A. Rida, R. Vyas, and M. M. Tentzeris, "RFID Tag and RF Structures on a Paper Substrate Using Inkjet-Printing Technology," *IEEE Trans. Microw. Theory Tech.*, vol. 55, no. 12, pp. 2894–2901, 2007, doi: 10.1109/TMTT.2007.909886.
- [5] M. W. H. IV and M. J. Havrilla, "A {NONDESTRUCTIVE} {TECHNIQUE} {FOR} {DETERMINING} {COMPLEX} {PERMITTIVITY} {AND} {PERMEABILITY} {OF} {MAGNETIC} {SHEET} {MATERIALS}

- {USING} {TWO} {FLANGED} {RECTANGULAR} {WAVEGUIDES},” *Prog. Electromagn. Res.*, vol. 79, pp. 367–386, 2008, doi: 10.2528/pier07102405.
- [6] Y. Taryana, A. Manaf, N. Sudrajat, and Y. Wahyu, “Electromagnetic Wave Absorbing Materials on Radar Frequency Range,” *J. Keramik dan Gelas Indones.*, vol. 28, no. 1, p. 1, Jun. 2019, doi: 10.32537/jkgi.v28i1.5197.
- [7] T. S. Bird, “Definition and Misuse of Return Loss [Report of the Transactions Editor-in-Chief],” *IEEE Antennas Propag. Mag.*, vol. 51, no. 2, pp. 166–167, 2009, doi: 10.1109/MAP.2009.5162049.
- [8] R. B. Marks, “A multilines method of network analyzer calibration,” *IEEE Trans. Microw. Theory Tech.*, vol. 39, no. 7, pp. 1205–1215, 1991, doi: 10.1109/22.85388.
- [9] W. B. Weir, “Automatic measurement of complex dielectric constant and permeability at microwave frequencies,” *Proc. IEEE*, vol. 62, no. 1, pp. 33–36, 1974, doi: 10.1109/PROC.1974.9382.
- [10] A. M. Nicolson and G. F. Ross, “Measurement of the Intrinsic Properties of Materials by Time-Domain Techniques,” *IEEE Trans. Instrum. Meas.*, vol. 19, no. 4, pp. 377–382, 1970, doi: 10.1109/TIM.1970.4313932.
- [11] F. Schwierz, J. Pezoldt, and R. Granzner, “Two-dimensional materials and their prospects in transistor electronics,” *Nanoscale*, vol. 7, no. 18, pp. 8261–8283, 2015, doi: 10.1039/c5nr01052g.
- [12] W. T. Hatmojo, “Perhitungan Permeabilitas dan Permittivitas Kompleks sebagai Fungsi Frekuensi pada Material Penyerap Gelombang Mikro,” Universitas Indonesia, 2013.
- [13] J. Baker-Jarvis, E. J. Vanzura, and W. A. Kissick, “Improved technique for determining complex permittivity with the transmission/reflection method,” *IEEE Trans. Microw. Theory Tech.*, vol. 38, no. 8, pp. 1096–1103, 1990, doi: 10.1109/22.57336.
- [14] Suharno, “Pembuatan dan Karakterisasi Bi_{1-x}YFeO₃/C, BiFe_{1-y}Zn_yO₃/C, dan Bi_{0.88}Y_{0.12}Fe_{1-y}Zn_yO₃/C Sebagai Absorber Gelombang Mikro Pada Frekuensi X Band.,” Universitas Indonesia, 2015.

Study Of Soil Vulnerability in East Java Using Horizontal and Vertical Spectrum Ratio (Hvsr) Method from Ambient Noise Waves

Eka Nurajannah Wulandari^{1,†}, Moh Iqbal Tawakal²

¹ Tangerang Geophysics Station, Meteorology, Climatology and Geophysics Agency, Meteorologi Street No.05, Tanah Tinggi, Tangerang, Tangerang City, Banten 15119, Indonesia

² Center for Meteorology, Climatology and Geophysics Region 2, Meteorology, Climatology and Geophysics Agency, Abdul Ghani Street No.05, Cempaka Putih, Ciputat, South Tangerang, Banten 15412, Indonesia

[†wulanjanah@gmail.com](mailto:wulanjanah@gmail.com)

Submitted: September 2020; Revised: October 2021; Approved: June 2022; Available Online: October 2022

Abstract. The risk level of an earthquake is determined by the geological condition on the area. East Java has a high level of seismicity. One of the earthquake mitigation efforts is to estimate the dynamic characteristics of ground using microtremors. The purpose of this study was to determine the natural frequency distribution, amplification factor, and seismic vulnerability index. Seismic signals are obtained from stationary and temporal seismograph records from 100 measurement locations installed in the East Java and Madura regions. This study uses the horizontal and vertical spectrum ratio (HVSr) curve analysis method popularized by Nakamura (2000). The results of the study showed that the seismic vulnerability index varied from 0.25 to 54.2. Areas that have a high level of earthquake risk include Bangkalan, Gresik, Jombang, Lumajang, Malang, Mojokerto, Pasuruan, Ponorogo, Sampang, Sidoarjo, and Surabaya. Based on the history of destructive earthquakes, this area has experienced earthquake intensity ranging from V - VIII MMI.

K Keywords: East Java, Seismic vulnerability index, HVSr, earthquake, mitigation

DOI: [10.15408/fiziya.v5i1.17226](https://doi.org/10.15408/fiziya.v5i1.17226)

INTRODUCTION

The eastern part of Java Island is one of the areas in Indonesia that has a very high potential for geological disasters. The existence of a volcano that stretches in the south also increases the risk of disaster. Very active seismicity levels often result in building damage and loss of life. Tectonically, East Java is in a subduction zone, namely the boundary between two plates that collide with each other, the oceanic plate subducts the continental plate. The subduction zone in the south of the island of Java often produces large earthquakes and has the potential for tsunamis. Generally, earthquakes with large strengths originate from the megathrust zone, which is a subduction zone that has a gentle dive angle to depth.

Based on physiography, East Java is part of the Sunda arc which stretches for 5600 km from the Andamans in the northwest to the Banda arc in the east. Then the zone

continues to Maluku to North Sulawesi with different names [1]. In East Java, the Indo-Australian plate movement is relatively perpendicular to the axis of Java Island at a lower speed than in Sumatra, which is only about 4.9 cm/year to 6.0 cm/year [2]. The continuous subduction of plates causes the formation of normal and rising fault patterns that are parallel to the island arc.

Figure 1 shows that in general East Java, which is marked with a red line, is dominated by ascending fault structures such as the Kendeng fault and descending faults such as Pasuruan, Probolinggo, and Baluran. The Kendeng Fault stretches from Central Java to East Java in a west-east direction. This fault is continuous with the Semarang fault to the Baribis fault. The level of seismicity in the East Java area is quite high, which is indicated by dots of different colors indicating different depths. It can be seen that the source of earthquakes is not only from the subduction zone (black line along the Indian Ocean), but in recent times earthquakes with moderate magnitude ($3 < M < 5$) to large scale ($M > 5$) often occur in along the Kendeng fault zone [3].

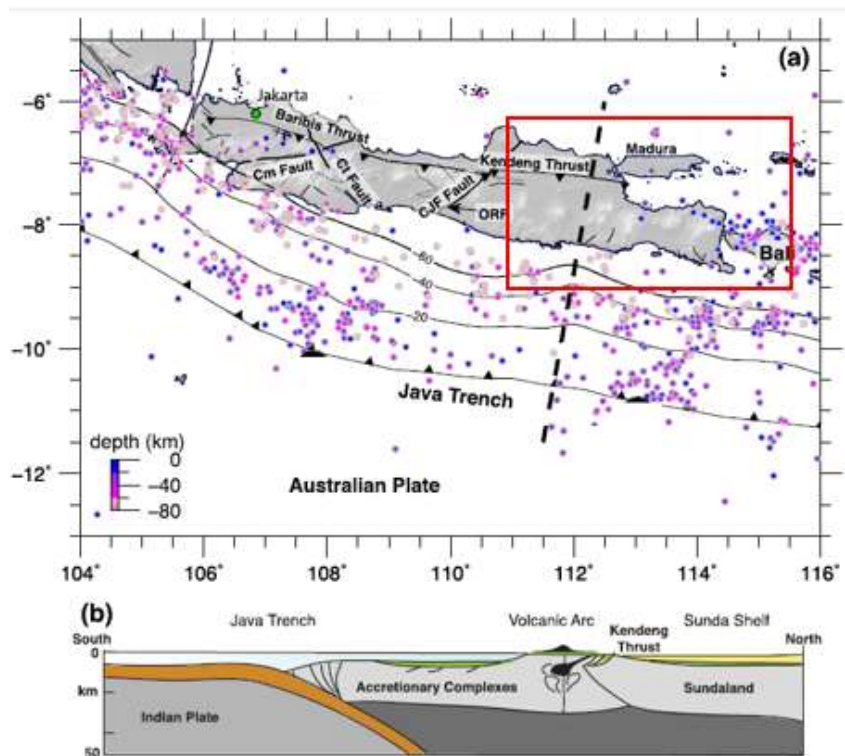


Figure 1. The Kendeng fault extends along eastern to central Java, the red line is the research area (Koulali et al, 2016).

This needs to be a concern for the community, especially those in the East Java region to continuously improve preparedness in dealing with the threat of disaster (hazard). Community preparedness in dealing with disasters is needed to reduce the risk of disasters caused. Disaster risk is influenced by external threats, vulnerabilities, and community capacities. The risk will be high when threats and vulnerabilities are high while capabilities are low.

One of the efforts to reduce disaster risk is through mitigation. Disaster mitigation can be initiated by conducting a study based on the geological conditions of the local area. Soil vulnerability studies are the first step to determine the level of disaster risk in

an area when an earthquake occurs. The purpose of this study was to determine the level of disaster risk in East Java based on the seismic vulnerability index (Kg).

METHOD

The research area is focused along East Java and Madura with coordinates 111,00 east longitude – 114,40 east longitude and 7,12 south longitude – 8,48 south longitudes. Administratively, it is included in East Java Province which has an area of 47,157,157.72 Km². It is bordered by the East Java region to the north by the Java Sea, to the east by the Bali Strait, to the south by the Indian Ocean, and to the west by the Province of Central Java.

This study uses secondary data in the form of passive seismic signal recordings (ambient noise) consisting of 27 broadband type seismometers three components CMG-3T seismograph network belonging to the Meteorology, Climatology and Geophysics Agency (BMKG), 17 short-period seismometers with three components Mark-L4- The MERAMEX (MERapi Amphibious Experiment) 3D seismograph network, and 56 trillium compact and Lennart 3D Lite portable seismographs are operated by the Australian National University (ANU) and BMKG. Each point is collected data for 24 hours.

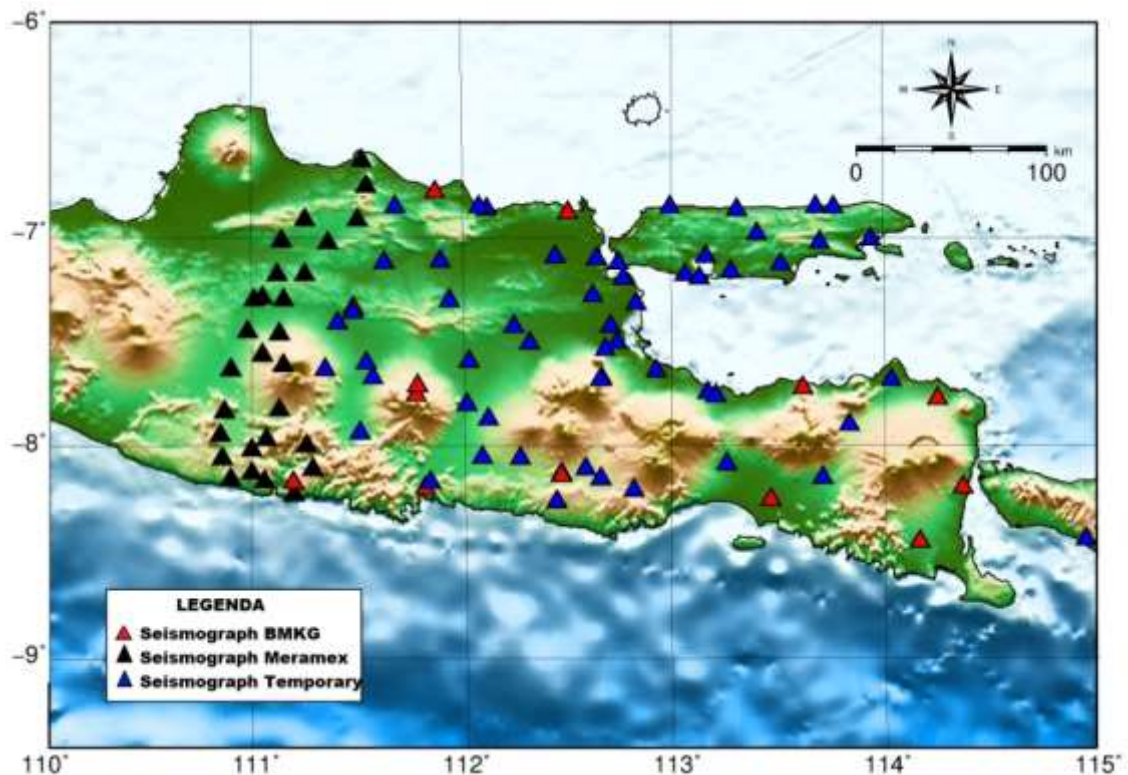


Figure 2. Seismograph network of research area, BMKG seismograph (red triangle), Meramex seismograph (black triangle), and Temporary seismograph (blue triangle).

Ambient noise analysis uses the HVSR technique, which is a comparison between the spectrum of the horizontal component to the spectrum of the vertical component. HVSR data processing using Geopsy software. Geopsy is software that is commonly used in seismic data processing. Mainly for determining the HVSR spectrum. The tools presented are very easy to understand making it easier to perform data processing. In

Geopsy, the steps in calculating HVSR in general are signal data input, parameter settings, windowing, Fourier transformation, smoothing, and h/v curves.

The determination of the peak of the h/v curve follows the criteria of the European Research Project's SESAME recommendation (2004) regarding the reliability criteria and the clear peak as a reference in determining the h/v curve [4]. Reliability criteria consist of three. First, the natural frequency is greater than 10 divided by the length of the windows (l_w). Second, the number of significant cycles is greater than 200 ($n_c(f_0) > 200$). Third, the standard deviation of the amplitude (h/v) as a function of frequency for $0.5f_0 < f < 2f_0$ is less than 2 if $f_0 > 0.5$ Hz and less than 3 if $f_0 < A_0/2$ at a frequency between $f_0/4$ and f_0 . Second, it has $A_{h/v}(f_+) < A_0/2$ at a frequency between f_0 and $4f_0$. Third, the amplification value at f_0 is more than 2. Fourth, the tolerance limit for f_0 is 5%. Fifth, the standard deviation of the frequency is smaller than the threshold limit ($\epsilon(f_0)$). Sixth, the amplification standard is smaller than the threshold limit ($\theta(f_0)$).

Furthermore, the analysis of soil characteristics is carried out by calculating the Seismic Vulnerability Index (Vulnerability Index). Nakamura (2000) provides an equation for the soil vulnerability index (K_g) as in equation (1)[5]. From the results of the analysis, the distribution of natural frequencies, soil amplification and vulnerability levels as well as their association with geological conditions in the study area will be known.

$$K_g = \frac{A_0^2}{F_0} \quad (1)$$

Where K_g is soil susceptibility index, A_0 is soil amplification and f_0 is natural frequency. From the results of the analysis, the distribution of natural frequencies, soil amplification and vulnerability levels as well as their association with geological conditions in the study area will be known.

RESULTS AND DISCUSSIONS

The natural frequency or also known as the dominant frequency is the number of vibrations or waves formed in a unit of time. According to Nakamura (2000) natural frequency is influenced by the average velocity and depth of bedrock. The natural frequency has a value that is directly proportional to the average velocity and inversely proportional to the bedrock depth. Areas that have low natural frequency values are associated with sedimentary rocks and high natural frequencies are associated with bedrock. Sato et al (2004) conducted a study on the characteristics of the natural frequency values of ambient noise recordings based on geomorphological conditions [6]. Geomorphologically, hilly areas have a higher natural frequency than the transitional areas between hills and plains. Meanwhile, alluvial plains have lower natural frequency values.

Natural frequencies in East Java and Madura range from 0.3 Hz to 5.5 Hz as shown in Figure 4.10. In general, the Kendeng Zone has a relatively lower frequency value than the Rembang and Southern Mountains zones. The highest frequency value is in the southern mountainous zone which is directly adjacent to the Indian Ocean. The Rembang zone in the north of the study area has a slightly higher frequency value than the Kendeng zone, indicated by the presence of Mount Lasem.

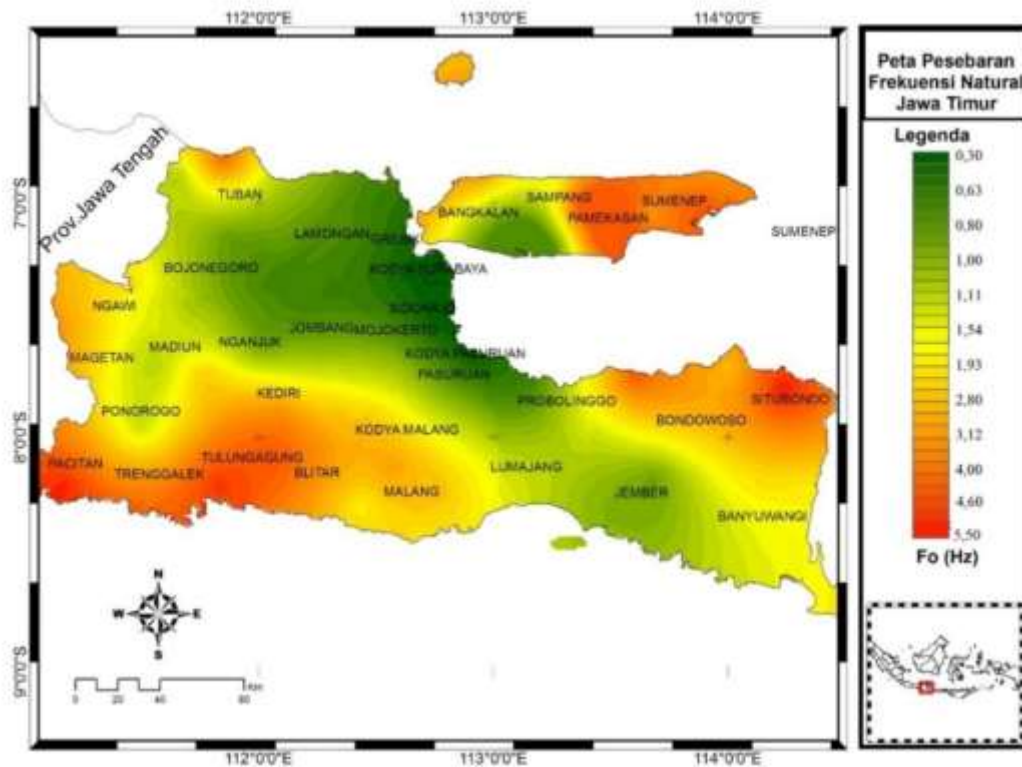


Figure 3. East Java Natural frequency distribution map.

Based on Figure 3, the natural frequency of the Kendeng zone ranges from 0.3 Hz to 1.5 Hz. The Kendeng Zone includes Magetan, Ngawi, Madiun, Bojonegoro, Nganjuk, Jombang, Surabaya City, Sidoarjo, Mojokerto, City and Regency, and Pasuruan. The natural frequency distribution is relatively lower in the east and increases towards the west and south of this zone. In general, the Kendeng zone is composed of alluvial plains in the east to the west bordering the Lawu mountains (Figure 3.1). Areas that have a natural frequency of less than 0.8 Hz are Surabaya, Sidoarjo, and Pasuruan. According to Kanai (in Subardjo, 2005) this area is classified as Type I type IV, composed of alluvial deposits formed from deltaic sedimentation, top soil and others. The thickness of the sediment layer is very thick ranging from 30 m to more than 200 m [7]. Even according to Smyth (2005) the depth of bedrock is not defined because it is covered by a very thick layer of sediment ranging from 8 km to 11 km [8].

The map of the distribution of the amplification factor in the East Java region shown in Figure 4 shows that the distribution of the highest amplification values is around Sidoarjo, Surabaya, and Gresik. While on the island of Madura, the distribution of the highest amplification factor is around Pamekasan. The value of the amplification factor in this region ranges from 3 – 5.90. High amplification factors are associated with low natural frequencies (Figure 3) and are closely related to local geological conditions. Areas that have a high amplification factor value ($A_0 > 3$), have the greatest risk of building damage during an earthquake (Nakamura, 2000) [5]. However, the amplification factor parameter is not sufficient to be able to conclude the level of vulnerability in an area, other parameters such as the vulnerability index are needed which provide information between the natural frequency and the amplification factor.

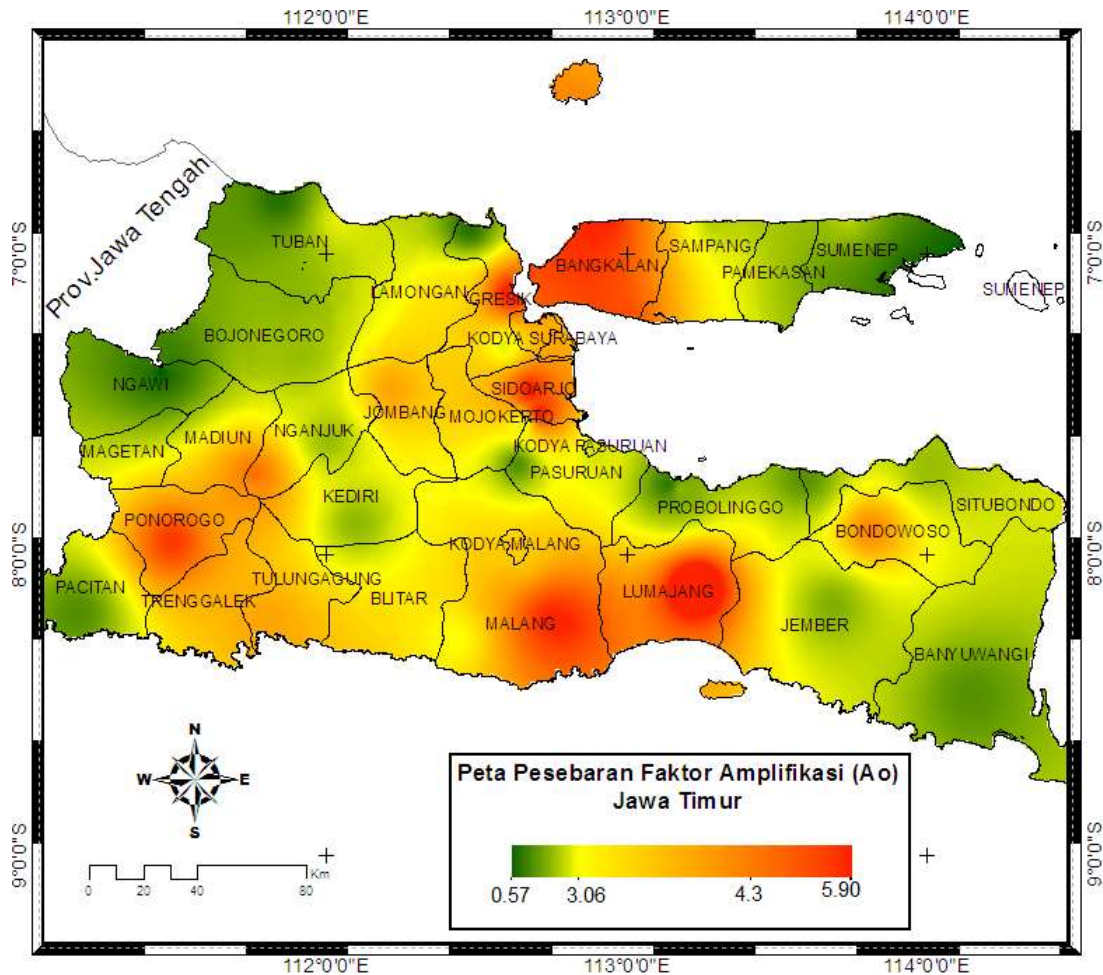


Figure 4. East Java amplification factor distribution map.

In general, hilly areas have relatively lower amplification factor values. This is in accordance with the research of Sato et al. (2004) who concluded that hilly areas have lower peaks of the h/v spectrum [6]. Areas that have a low amplification factor ($A_0 < 1$) are Pacitan, Ponorogo, Tuban, Banyuwangi, Bondowoso, and Sidobondo. On the island of Madura dominated by low amplification factor values, associated with high natural frequencies. These areas include Sumenep, Sampang, and Bangkalan.

Seismic susceptibility index is influenced by sedimentary rock lithology, age of sedimentary rock, thickness of sedimentary layer, and depth of ground water table [9]. In addition, geomorphological conditions also greatly affect the seismic vulnerability index. Coastal areas, swamps, and reclamation have a high index of seismic vulnerability, while hilly areas have a very low index of seismic vulnerability. Damage to buildings due to earthquakes has a relationship with the seismic vulnerability index. Many studies have conducted studies between the areas affected by the earthquake and the distribution of the seismic vulnerability index. The results of the study concluded that areas experiencing the worst damage had a high seismic vulnerability index, while areas experiencing minimum damage had a low seismic vulnerability index. In addition, areas with a high seismic vulnerability index are prone to liquefaction.

The results of the study show that the East Java region has a seismic vulnerability index between 0.25 to 63.82. Figure 5 shows the distribution of the high vulnerability index in the areas of Sidoarjo, Surabaya, and Gresik which are marked by red gradations.

Areas that have a seismic vulnerability index between 6 and 30 are Pasuruan, Mojokerto, Jombang, Lumajang, Kediri, Tulungagung, Blitar, Malang, Jember, Bangkalan, Pamekasan and Sampang. Meanwhile, areas with a low seismic vulnerability index include Tuban, Bojonegoro, Ngawi, Magetan, Madiun, Ponorogo, Pacitan, Trenggalek, Banyuwangi, Bondowoso, Situbondo, and Sumenep.

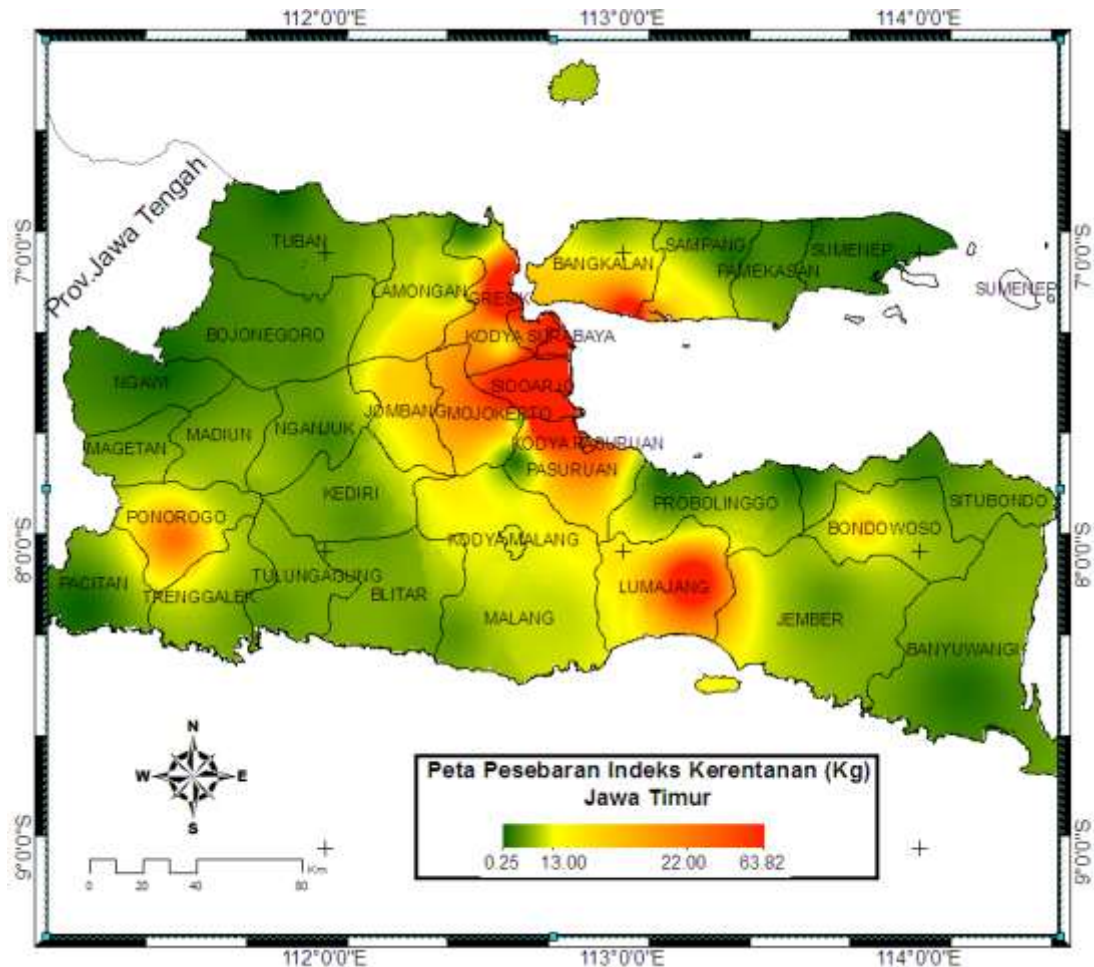


Figure 5. Map of the distribution of the East Java Soil Vulnerability Index.

Based on the history of the earthquake-affected area from 1799 – 2010 (Nguyen., N, et al., 2015) and the catalog of significant and destructive earthquakes in 1821-2017 (BMKG Earthquake and Tsunami Center, 2017) shows the strength of the intensity of earthquakes that occurred in the Java region. East ranges from III to IX MMI. This means that the level of damage caused by the earthquake is quite severe. The intensity of the earthquake with a strength of V – IX MMI indicates that the buildings of the structural and non-structural categories are damaged. In general, the earthquake-affected area is in an area of yellow to red color gradation (Figure 6). This supports the results of the study that the seismic vulnerability index is correlated with the level of earthquake risk. The higher the seismic vulnerability index, the greater the level of disaster risk. Therefore, disaster preparedness needs to be improved, especially for areas that have a high level of disaster risk.

In addition, the seismic susceptibility index greatly affects the response of rocks to the propagation of earthquake waves. The propagation of earthquake waves will

experience attenuation with respect to the propagation distance. However, when the area has a higher seismic vulnerability index, it will experience a strengthening of earthquake waves or what is known as the local site effect.

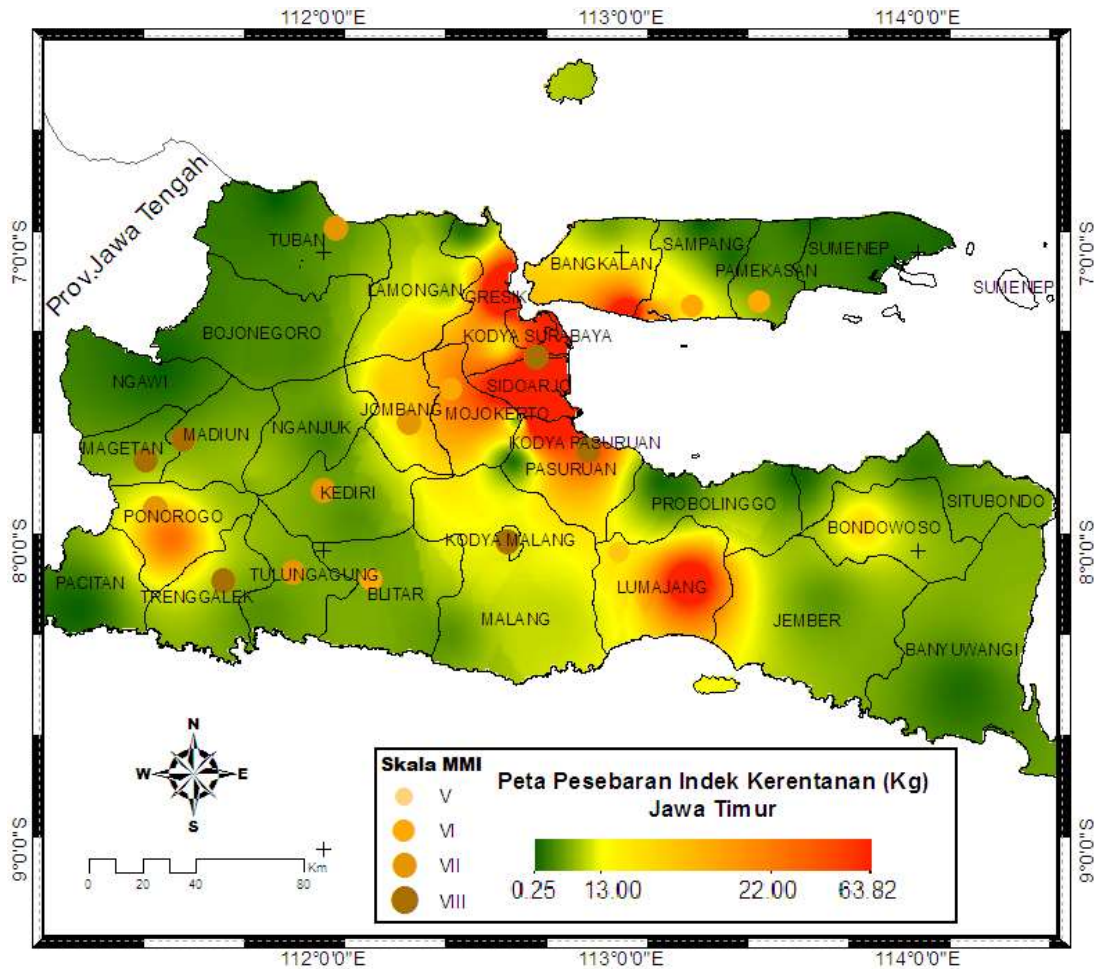


Figure 6. The history of the area affected by the earthquake and the distribution of the seismic vulnerability index in the East Java region.

CONCLUSIONS

East Java's natural frequency distribution ranges from 0.27 to 6.74 Hz, the amplification factor ranges from 0.57 to 7.18 times the wave amplification, and the seismic vulnerability index ranges from 0.23 to 64.44. Areas that have a high level of earthquake risk seen from the distribution of the seismic vulnerability index (Kg) include Lumajang, Malang, Pasuruan, Mojokerto, Sidoarjo, Surabaya, Gresik, Jombang, Ponorogo, Bangkalan, and Sampang. Areas that have a high level of earthquake risk are expected to increase preparedness, especially in regional spatial planning (RTRW) in order to reduce building damage due to earthquakes.

REFERENCES

- [1] Kertapati, E. (2006). *Aktivitas Gempabumi di Indonesia Perspektif Regional Pada Karakteristik Gembumi Merusak*. Pusat Survei Geologi Bandung, 109.

- [2] Katili, J.A.,(1973). *Volcanism and Plate Tectonics in Indonesian Island Arc*, Tectonophys., v.26.,p 165 – 188.
- [3] Tim Pusat Gempa Nasional. (2017). *Peta Sumber dan Bahaya Gempa Indonesia Tahun 2017*, Pusat Penelitian dan Pengempabagn Kementrian PUPR.Jakarta.
- [4] SESAME. (2004). *Guidelines For The Implementation Of The H/V Spectral Ratio Technique on Ambient Vibrations*. Europe: SESAME European research project.
- [5] Nakamura, Y. (2000). Clear identification of fundamental idea of Nakamura's technique and its applications. *Proc XII World Conf. Earthquake Engineering*, New Zealand,2656.
- [6] Sato, T., Nakamura, Y., and Saita, J. (2004). *Evaluation of The Amplification Characteristics of Subsurface Using Microtremor and Strong Motion: The Studies at Mexico City*.13th
- [7] Ibrahim, G., & Subardjo.(2005). *Pengetahuan Seismologi*. jakarta: Badan Meteorologi dan Geofisika.
- [8] Smyth, H., Hall, R., Hamilton, J., and Kinny, P. (2005). *East Java: Cenozoic basins, volcanos and ancient baserock*, *Proceedings of Indonesia Petroleum Association, Annual Convention 30th*, 251-266.
- [9] Daryono. (2009).*Indeks Kerentanan Seismik Berdasarkan Mikrotremor Pada Setiap Satuan Bentuklahan Di Zona Graben Bantul Daerah Istimewa Yogyakarta*, Disertasi, Universitas Gajah Mada, Yogyakarta.
- [10] Ngoc Nguyen, Jonathan Griffin, Athanasius Cipta and Phil R. Cummins. (2015). *Indonesia's Historical Earthquakes Modelled examples for improving the national hazard map*. *Record 2015/23 Geoscience Australia*. Canberra.<http://dx.doi.org/10.11636/Record.2015.023>
- [11] Pusat Gempabumi dan Tsunami BMKG. (2018).*Katalog Gempabumi Signifikan dan Merusak Tahun 1821-2017*. Badan Meteorologi Klimatologi dan Geofisika. Jakarta. ISSN 2477-0582.

Evaluation Of Coal Distribution For Alternative Energy Using Seismic Spectral Decomposition

Praditiyo Riyadi^{1,†}, Arkanu Andaru²

¹Physics Study Program, Faculty of Sciences and Technology, State Islamic University Syarif Hidayatullah Jakarta, Ir. H. Djuanda Street No.95, Cempaka Putih, Ciputat, South Tangerang, Banten 15412, Indonesia

²School of Computing, College of Engineering and Computer Science, Australian National University, 108 North Road, Acton, ACT 2601, Australia

[†]praditiyo.riyadi@uinjkt.ac.id

Submitted: September 2020; Revised: October 2021; Approved: June 2022; Available Online:
Desember 2022

Abstract. Indonesia is the largest coal producer in the world, and Sumatera is one of the contributors to Indonesia's coal production. Coal is generally widely used for industrial fuel or power plants with production directly on the surface. The technology to develop coal into alternative energy sources (Coal Bed Methane (CBM) & Underground Coal Gasification (UCG)) began to develop with various production methods in the earth without having to be exploited directly. To apply this production method, it is necessary to analyze the distribution of coal below the earth's surface. The research area is located in the South Sumatera Basin with coal targets in the Muara Enim Formation. The data consists of 3D seismic data and well data as validation. From the well data, it was identified that there was coal in two zones, with an average thickness in Zone A reaching 6 meters while in Zone B the average thickness reaching 11 meters. The results of the amplitude spectrum analysis from the seismic data, obtained three dominant frequency trends from seismic data, 26 Hz, 42 Hz, and 58 Hz. By using the calculation of $\frac{1}{4}$ wavelength, the frequency that matches the thickness of the coal is 58 Hz for Zone A and 42 Hz for Zone B coal layer. Seismic amplitudes are then separated based on their frequency using the Spectral Decomposition method, and the distribution of coal is validated with existing well data.

Keywords: Coal, Alternative Energy, Frequency, Spectral Decomposition, South Sumatera Basin

DOI: [10.15408/fiziya.v5i1.26670](https://doi.org/10.15408/fiziya.v5i1.26670)

INTRODUCTION

Coal that was originally a mining commodity began to be utilized for unconventional energy that can be used in the long term. Coal Bed Methane (CBM) and Underground Coal Gasification (UCG) is a method used to obtain alternative energy from the coal [1]. South Sumatra Basin has is one of the larges potential coals in Indonesia, as for the coal bearing formation in this basin is Muara Enim formation [6]. Muara Enim formation deposited in shallow marine to parallic and non-marine environments [4]. This formation consists of claystone's and shales intercalated by sandstone and coal layer (Figure 1). On other hand, based on analysis of well and seismic data, divided Muara Enim

formation into two depositional packages: Lower and Upper Muara Enim formation, These two depositional packages consist of three sub-environments, they are tidal mud flat, tidal mixed flat and tidal sand flat environment [12]. Knowing the distribution of coal for unconventional energy targets is an important step, in which the objective is to maximize production in the case of CBM and reduce the level of hazard in the case of UCG method in the target field [13][15]

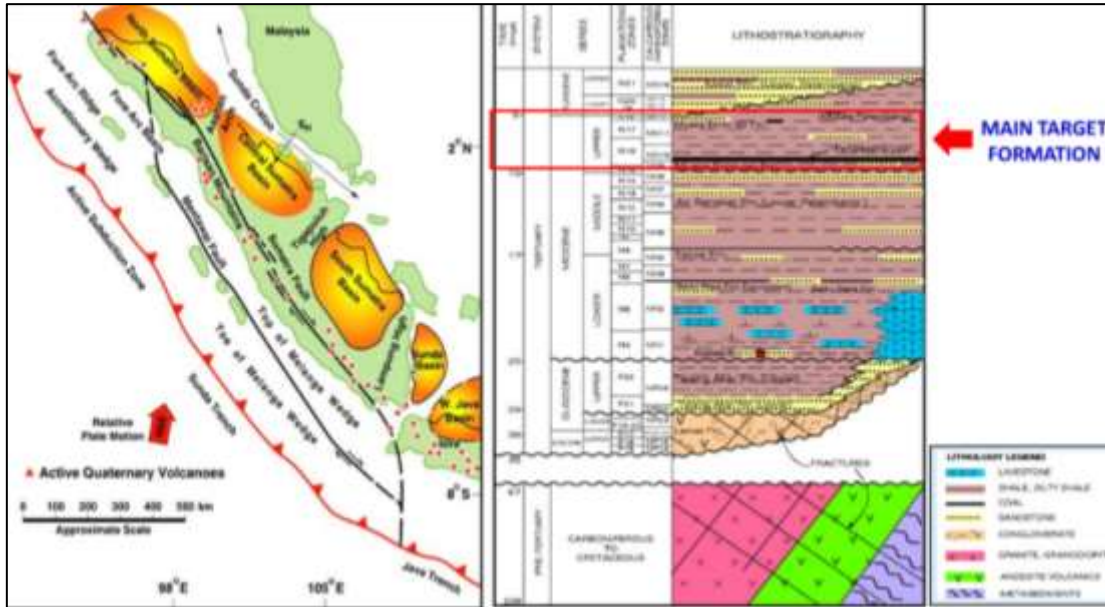


Figure. 1 Regional stratigraphy of south sumatera basin (Heidrik & Aulia, 1993)

Spectral decomposition is a method of signals processing on the seismic data [2][3]. By utilizing frequencies in seismic data, spectral decomposition is useful to distinguish the lithology of the target area vertically and laterally on the seismic data [5]. The lateral coal distribution analysis will provide geologically useful information, thereby increasing success for unconventional energy exploration on the target field [11].

DATA AND METHOD

There are 10 wells that reach the coal target, and the well data is used for the validator. The target consists of two layers of Zone A coal and Zone B coal.

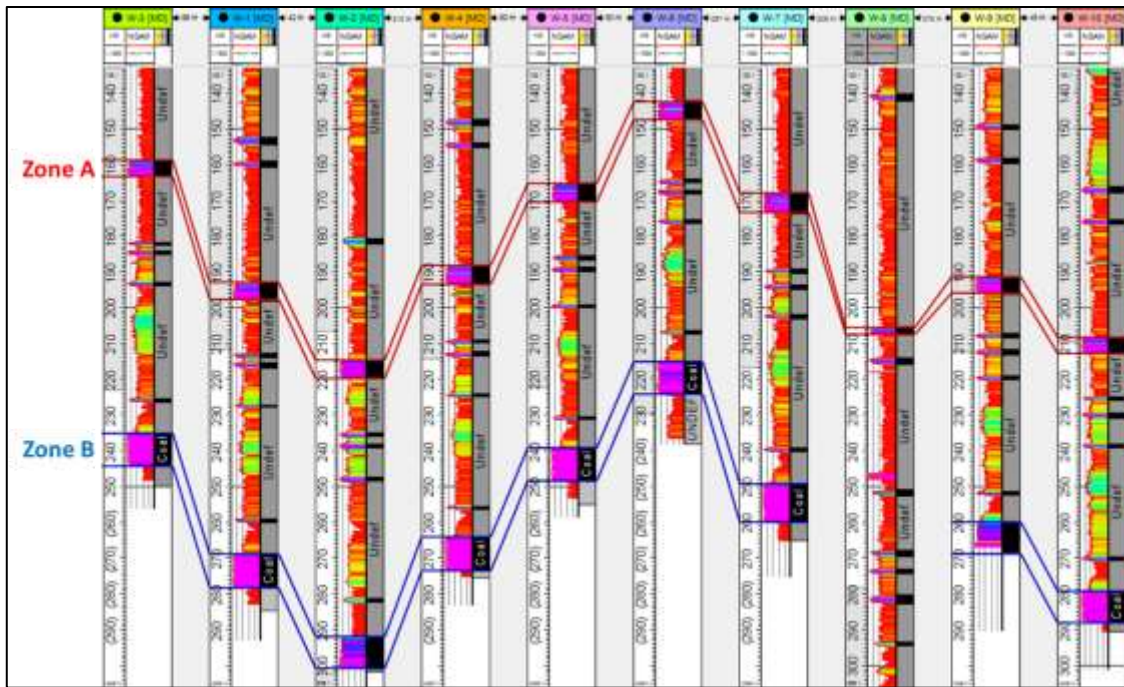


Figure. 2 Coal zone in the well correlation of study area

Coal thickness in Zone A reaches an average thickness of 6 m, whereas in Zone B coal reaches an average thickness of almost 11 m. From the result of correlation of 10 wells directed NW - SE in the study area visible thickness of coal that is consistent from Zone A and Zone B (Figure 2). There are 10 wells that reach the coal target, and the well data is used for the validator. There is also 3D seismic data in this research area, but need to do the data conditioning first in order to reduce the high frequency noise contained in the data [10][14]. The method used for conditioning is the Dip-Steering Median Filter (Figure 3). There are 10 wells that reach the coal target, and the well data is used for the validator.

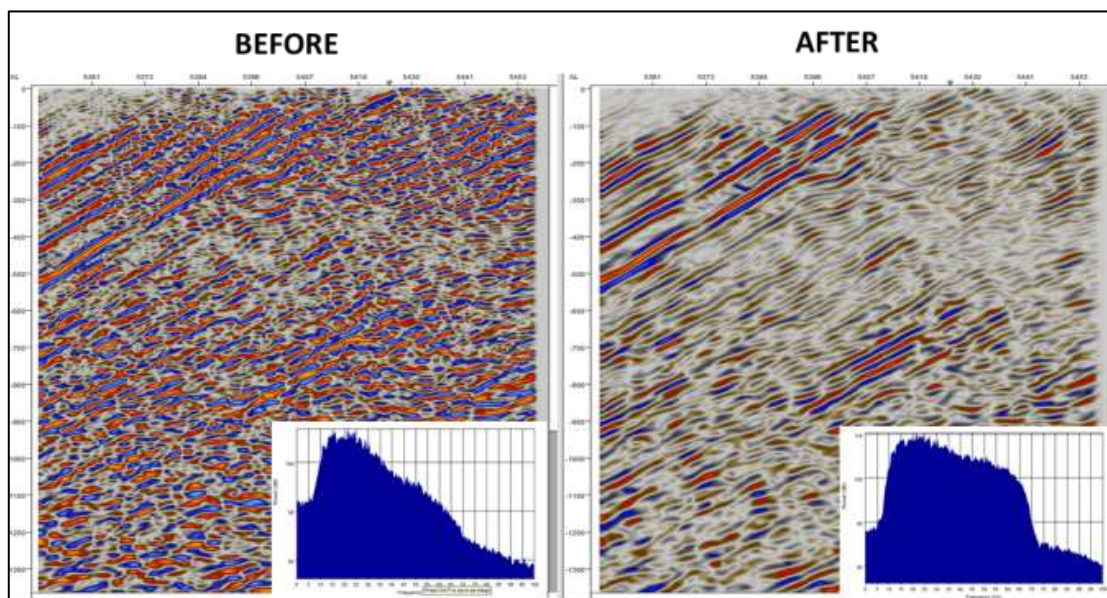


Figure. 3 Seismic 3D on target area before (left) and after (right) conditioning

There are various methods of spectral decomposition such as Short Time Fourier Transform (STFT), Continuous Wavelet Transform (CWT), and Hilbert-Huang Transform (HHT) [7], but in this research will be used continuous Wavelet Transform (CWT) method. The CWT method is principally to find a match of the input signal / wavelet provided with the seismic data, that is by stretch and squeeze (scaling) the input signal and correlate all the time to the seismic data [8][9].

RESULTS AND DISCUSSIONS

From the results of depositional coal in the target area is Muara Enim formation on Zone A and Zone B coal. Based on correlation log depositional environment the target area is lacustrine. Based on seismic and well data, trend coal structure of Zone A and Zone B is homocline structure. Amplitude spectrum analysis on the seismic data used in the target area of research, obtained of three different frequencies on the coal targets area (Figure 4). These three frequencies are generated from three maximum amplitudes in the target area (Zone A and Zone B). Using tuning thickness analysis of $\frac{1}{4}$ wavelength, the distance of the seismic scope in the vertical limit is 5.46 m at 58 Hz frequency, 9.87 m at 42 Hz frequency and 15.52 m at 26 Hz frequency. So that the value of seismic resolution that is close to the thickness of coal in Zone A which has an average thickness of 6 meters is 58 Hz, and in Zone B with an average thickness of 11 meters is 42 Hz. Spectral decomposition seismic attributes were distributed using a frequency of 58 Hz for Zone A and 42 Hz for Zone B coal zone. Strong amplitude of the Spectral Decomposition Attribute results with a high value is the correlation of the sought coal thickness. It is clear that the distribution of coal in Zone A and Zone B is validated by well data (Figure 3). The result of the Spectral decomposition attribute indicates coal Zone A and Zone B direction SE-NW, which is the main direction of coal distribution.

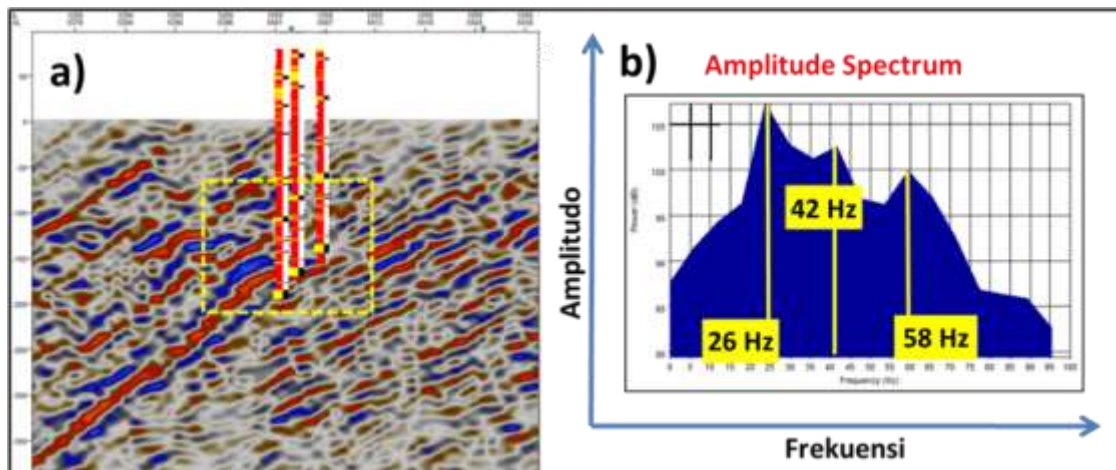


Figure. 4 (a) Area of interest in seismic (b) Seismic amplitude spectrum analysis

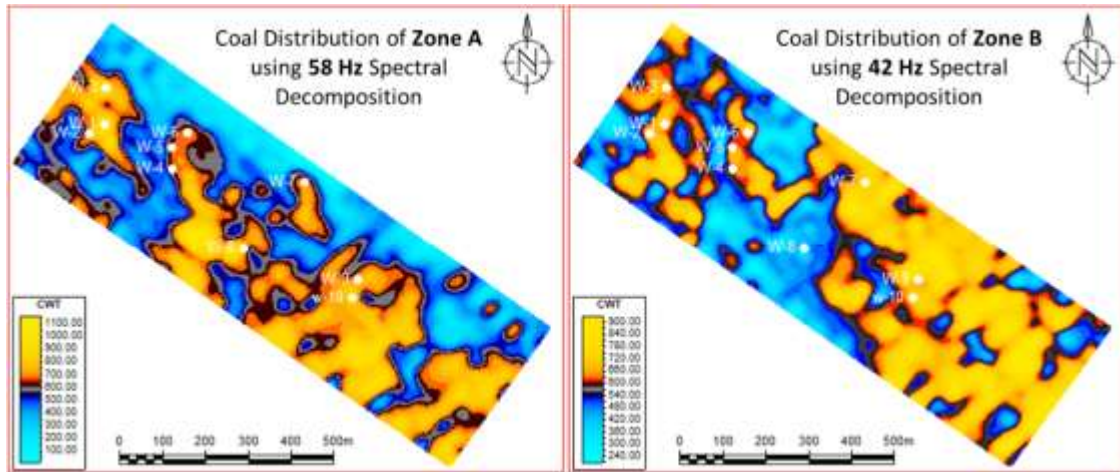


Figure. 5 Coal distribution (yellow to red) from spectral decomposition attributes at 58 Hz frequency in the Zone A (left) and 42 Hz frequency in Zone B (right)

CONCLUSIONS

Spectral decomposition method is very useful to see the distribution of coal in the target zone of Zone A and Zone B with a coal thickness around 6 to 11 m and the frequency of seismic data obtained to achieve the target zone thickness is 58 Hz for Zone A and 42 Hz for Zone B coal zone. Strong amplitude of the Spectral Decomposition Attribute results indicated by a high value is the distribution of coal which is validated by well data penetrating in the coal zone. There is a prospect area for new drilling on the Zone A and zone B coal zone in the South East of study area. This area of research is suitable for unconventional target energy methods such as CBM and UCG, due to the continuous expanse of coal extending towards the NW-SE.

REFERENCES

- [1] APEC Secretariat, 2013, APEC Energy Demand and Outlook 5th Edition, Asia Pacific Energy Research Centre, Institute of Energy Economics, Japan.
- [2] Castagna, John, and S. S, Comparison of spectral decomposition methods. *First Break*, 2006: p. 75-79.
- [3] Chopra, S. and K.J. Marfurt, Spectral decomposition and spectral balancing of seismic data. *The Leading Edge*, 2016. 35(2): p. 176-179.
- [4] Kurniawan, Erlangga., et al., 2020, Estimasi Sumberdaya Underground Coal Gasification (Ucg), Daerah Banjarsari, Tanjung Enim, Sumatera Selatan, Prosiding TPT XXIX PERHAPI 2020.
- [5] Lapins, Sacha., et al., 2020, An examination of the continuous wavelet transform for volcano-seismic spectral analysis, *Journal of Volcanology and Geothermal Research*.
- [6] Muksin, N., et al., Regional Depositional environment model of Muara Enim Formation and its significant implication for CBM prospectivity in South Sumatra Basin, Indonesia. *American Association of Petroleum Geologists, Search and Discovery Article*, 2012. 80272.
- [7] Ostrander, W. J. (1984); Plane-wave reflection coefficients for gas sands at nonnormal angles of incidence. *Geophysics*; 49 (10): 1637–1648.
- [8] Russell, B. H. (1988). *Introduction to seismic inversion methods (Vol. 2)*. Tulsa: Society of Exploration Geophysicists.

- [9] Saputro, R. A., Suprajitno Munadi, and Humbang Purba, 2012, Spectral Filtering For Removing Coal Bright Spot Effect In Seismic Interpretation, Scientific Contributions Oil & Gas, Vol. 35. No. 3: 109 - 114
- [10] Sheriff, R. E., & Geldart, L. P. (1995). Exploration seismology. Cambridge university press.
- [11] Sinha, S.K., et al. Time-frequency attribute of seismic data using continuous wavelet transform. SEG Annual Meeting. 2003. Society of Exploration Geophysicists.
- [12] Sitompul N., et al., 1992, Effects of Sea Level Drops During Late Early Miocene to The Reservoirs in South Palembang Sub Basin, South Sumatra, Indonesia, Proceedings of the Indonesian Petroleum Association, 21st, 309-324.
- [13] Sugiyono, A., Permana, A.D., Boedoyo, M.S dan Adiarso, 2013, Outlook energi Indonesia 2013, Pusat Teknologi Pengembangan Sumberdaya Energi, Badan Pengkajian dan Penerapan Teknologi.
- [14] Yilmaz, Ozdogan. (2001). Seismic Data Analysis: Processing, Inversion, and Interpretation of Seismic Data (Volume 1). Society of Exploration Geophysics. Volume 1.
- [15] Zheng, Wenbo., et al., 2020, Study on the Coalbed Methane Development under High In Situ Stress, Large Buried Depth, and Low Permeability Reservoir in the Libi Block, Qinshui Basin, China, Advances in Civil Engineering, 10.1155/2020/6663496.

Evaluation Of Coal Distribution For Alternative Energy Using Seismic Spectral Decomposition

Praditiyo Riyadi ^{1,†}, Arkanu Andaru²

¹Physics Study Program, Faculty of Sciences and Technology, State Islamic University Syarif Hidayatullah Jakarta, Ir. H. Djuanda Street No.95, Cempaka Putih, Ciputat, South Tangerang, Banten 15412, Indonesia

²School of Computing, College of Engineering and Computer Science, Australian National University, 108 North Road, Acton, ACT 2601, Australia

[†]praditiyo.riyadi@uinjkt.ac.id

Submitted: September 2020; Revised: October 2021; Approved: June 2022; Available Online:
Desember 2022

Abstract. Indonesia is the largest coal producer in the world, and Sumatera is one of the contributors to Indonesia's coal production. Coal is generally widely used for industrial fuel or power plants with production directly on the surface. The technology to develop coal into alternative energy sources (Coal Bed Methane (CBM) & Underground Coal Gasification (UCG)) began to develop with various production methods in the earth without having to be exploited directly. To apply this production method, it is necessary to analyze the distribution of coal below the earth's surface. The research area is located in the South Sumatera Basin with coal targets in the Muara Enim Formation. The data consists of 3D seismic data and well data as validation. From the well data, it was identified that there was coal in two zones, with an average thickness in Zone A reaching 6 meters while in Zone B the average thickness reaching 11 meters. The results of the amplitude spectrum analysis from the seismic data, obtained three dominant frequency trends from seismic data, 26 Hz, 42 Hz, and 58 Hz. By using the calculation of $\frac{1}{4}$ wavelength, the frequency that matches the thickness of the coal is 58 Hz for Zone A and 42 Hz for Zone B coal layer. Seismic amplitudes are then separated based on their frequency using the Spectral Decomposition method, and the distribution of coal is validated with existing well data.

Keywords: Coal, Alternative Energy, Frequency, Spectral Decomposition, South Sumatera Basin

DOI: [10.15408/fiziya.v5i1.81374](https://doi.org/10.15408/fiziya.v5i1.81374)

INTRODUCTION

Coal that was originally a mining commodity began to be utilized for unconventional energy that can be used in the long term. Coal Bed Methane (CBM) and Underground Coal Gasification (UCG) is a method used to obtain alternative energy from the coal. South Sumatra Basin has is one of the larges potential coals in Indonesia, as for the coal bearing formation in this basin is Muara Enim formation. Muara Enim formation deposited in shallow marine to paralic and non-marine environments. This formation consists of claystone's and shales intercalated by sandstone and coal layer (Figure 1). On other hand, based on analysis of well and seismic data, divided Muara Enim formation

into two depositional packages: Lower and Upper Muara Enim formation [3], These two depositional packages consist of three sub-environments, they are tidal mud flat, tidal mixed flat and tidal sand flat environment. Knowing the distribution of coal for unconventional energy targets is an important step, in which the objective is to maximize production in the case of CBM and reduce the level of hazard in the case of UCG method in the target field.

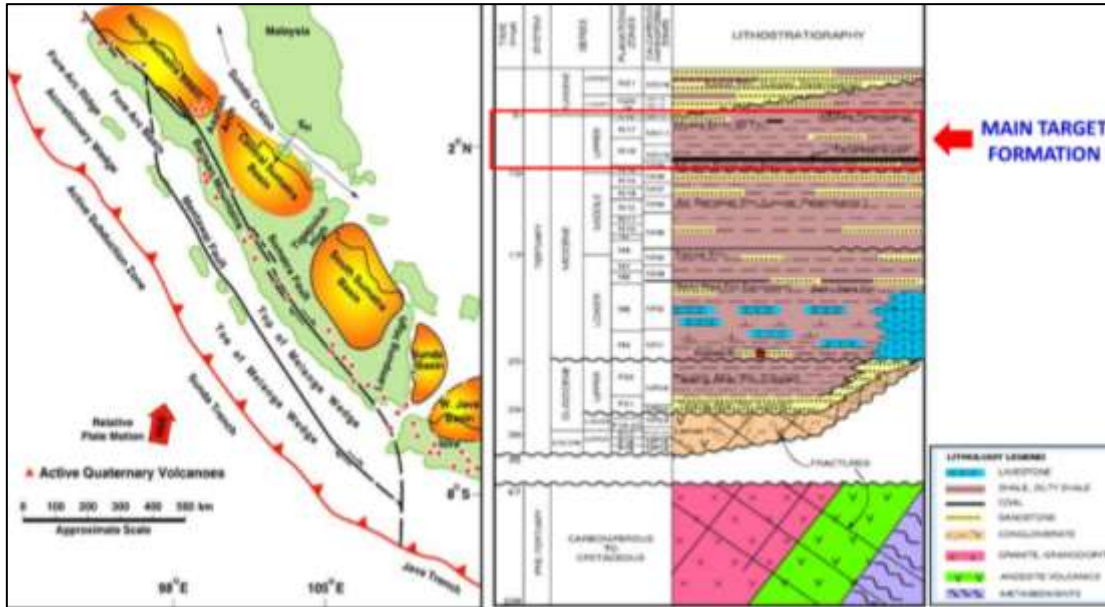


Figure. 1 Regional stratigraphy of south sumatera basin (Heidrik & Aulia, 1993)

Spectral decomposition is a method of signals processing on the seismic data. By utilizing frequencies in seismic data, spectral decomposition is useful to distinguish the lithology of the target area vertically and laterally on the seismic data. The lateral coal distribution analysis will provide geologically useful information, thereby increasing success for unconventional energy exploration on the target field.

DATA AND METHOD

There are 10 wells that reach the coal target, and the well data is used for the validator. The target consists of two layers of Zone A coal and Zone B coal.

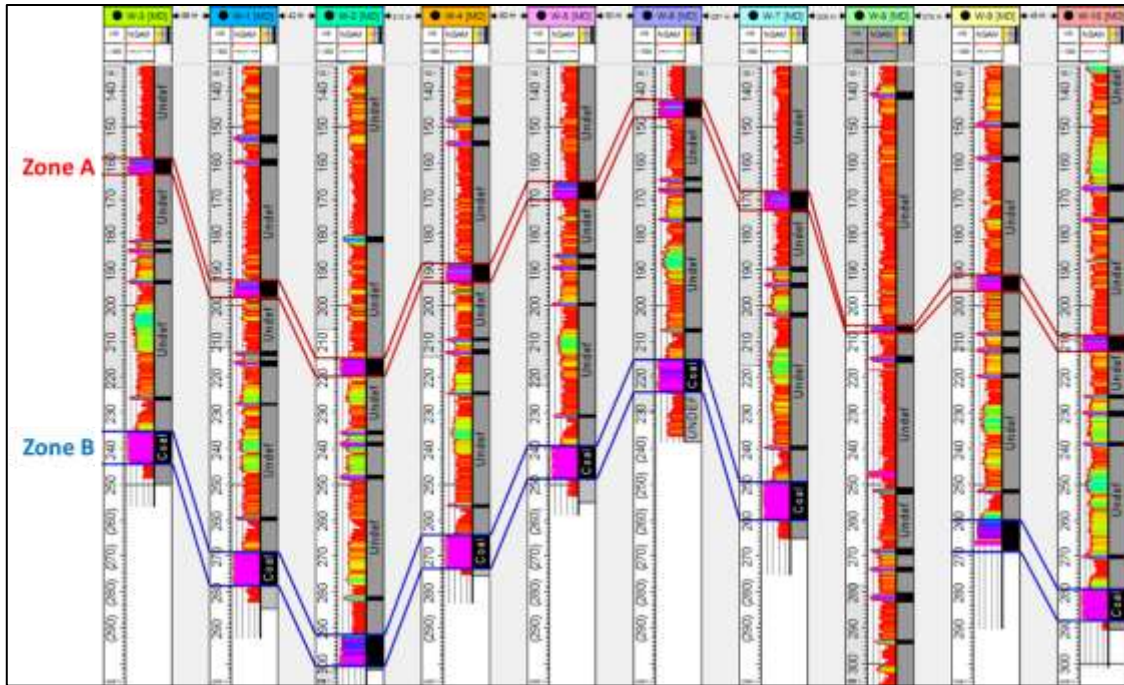


Figure. 2 Coal zone in the well correlation of study area

Coal thickness in Zone A reaches an average thickness of 6 m, whereas in Zone B coal reaches an average thickness of almost 11 m. From the result of correlation of 10 wells directed NW - SE in the study area visible thickness of coal that is consistent from Zone A and Zone B (Figure 2). There are 10 wells that reach the coal target, and the well data is used for the validator. There is also 3D seismic data in this research area, but need to do the data conditioning first in order to reduce the high frequency noise contained in the data. The method used for conditioning is the Dip-Steering Median Filter (Figure 3). There are 10 wells that reach the coal target, and the well data is used for the validator.

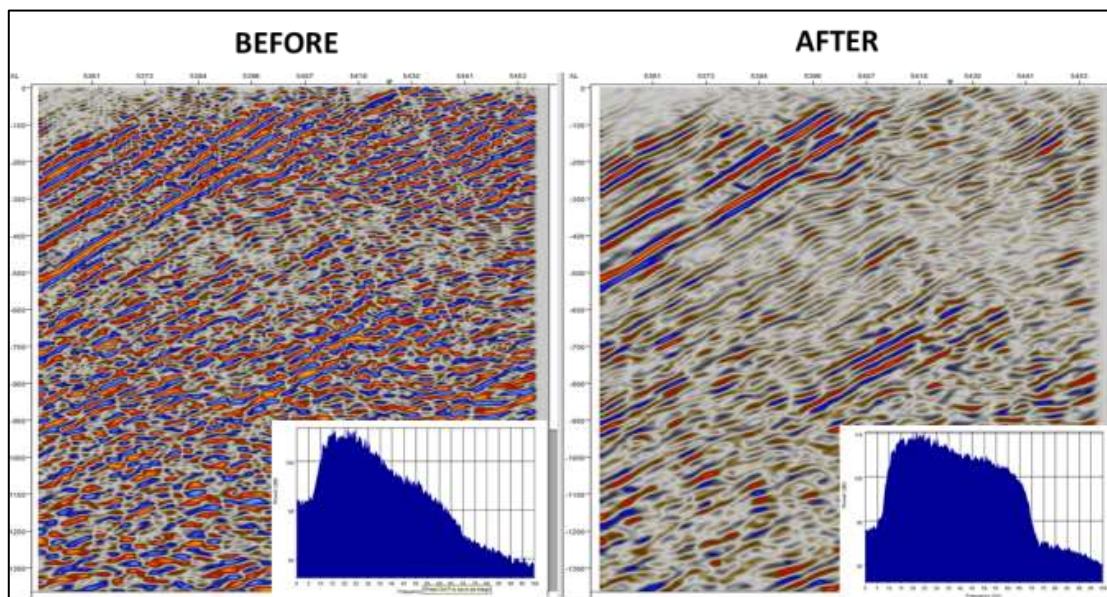


Figure. 3 Seismic 3D on target area before (left) and after (right) conditioning

There are various methods of spectral decomposition such as Short Time Fourier Transform (STFT), Continuous Wavelet Transform (CWT), and Hilbert-Huang Transform (HHT) [1, 2], but in this research will be used continuous Wavelet Transform (CWT) method. The CWT method is principally to find a match of the input signal / wavelet provided with the seismic data, that is by stretch and squeeze (scaling) the input signal and correlate all the time to the seismic data [4].

RESULTS AND DISCUSSIONS

From the results of depositional coal in the target area is Muara Enim formation on Zone A and Zone B coal. Based on correlation log depositional environment the target area is lacustrine. Based on seismic and well data, trend coal structure of Zone A and Zone B is homocline structure. Amplitude spectrum analysis on the seismic data used in the target area of research, obtained of three different frequencies on the coal targets area (Figure 4). These three frequencies are generated from three maximum amplitudes in the target area (Zone A and Zone B). Using tuning thickness analysis of $\frac{1}{4}$ wavelength, the distance of the seismic scope in the vertical limit is 5.46 m at 58 Hz frequency, 9.87 m at 42 Hz frequency and 15.52 m at 26 Hz frequency. So that the value of seismic resolution that is close to the thickness of coal in Zone A which has an average thickness of 6 meters is 58 Hz, and in Zone B with an average thickness of 11 meters is 42 Hz. Spectral decomposition seismic attributes were distributed using a frequency of 58 Hz for Zone A and 42 Hz for Zone B coal zone. Strong amplitude of the Spectral Decomposition Attribute results with a high value is the correlation of the sought coal thickness. It is clear that the distribution of coal in Zone A and Zone B is validated by well data (Figure 3). The result of the Spectral decomposition attribute indicates coal Zone A and Zone B direction SE-NW, which is the main direction of coal distribution.

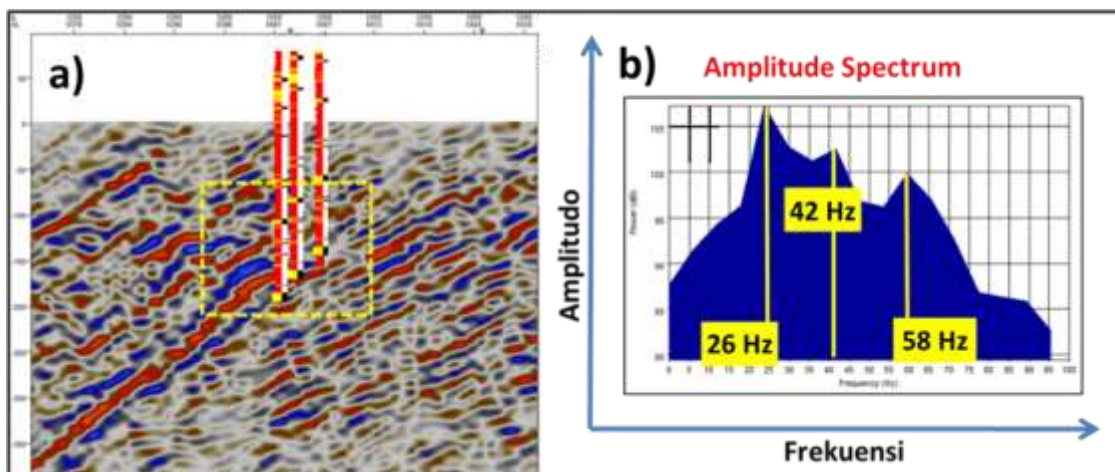


Figure. 4 (a) Area of interest in seismic (b) Seismic amplitude spectrum analysis

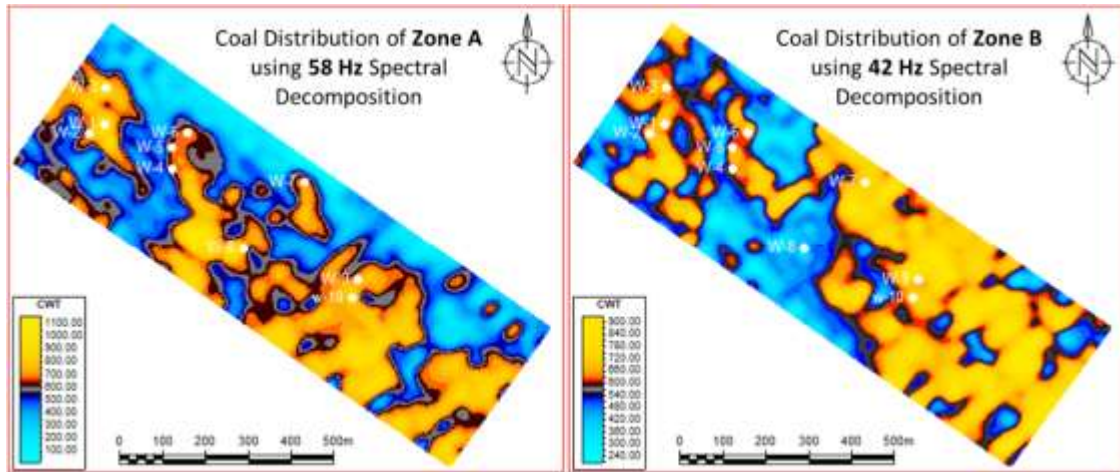


Figure. 5 Coal distribution (yellow to red) from spectral decomposition attributes at 58 Hz frequency in the Zone A (left) and 42 Hz frequency in Zone B (right)

CONCLUSIONS

Spectral decomposition method is very useful to see the distribution of coal in the target zone of Zone A and Zone B with a coal thickness around 6 to 11 m and the frequency of seismic data obtained to achieve the target zone thickness is 58 Hz for Zone A and 42 Hz for Zone B coal zone. Strong amplitude of the Spectral Decomposition Attribute results indicated by a high value is the distribution of coal which is validated by well data penetrating in the coal zone. There is a prospect area for new drilling on the Zone A and zone B coal zone in the South East of study area. This area of research is suitable for unconventional target energy methods such as CBM and UCG, due to the continuous expanse of coal extending towards the NW-SE.

REFERENCES

- [1] Castagna, John, and S. S, Comparison of spectral decomposition methods. *First Break*, 2006: p. 75-79.
- [2] Chopra, S. and K.J. Marfurt, Spectral decomposition and spectral balancing of seismic data. *The Leading Edge*, 2016. 35(2): p. 176-179.
- [3] Muksin, N., et al., Regional Depositional environment model of Muara Enim Formation and its significant implication for CBM prospectivity in South Sumatra Basin, Indonesia. *American Association of Petroleum Geologists, Search and Discovery Article*, 2012. 80272.
- [4] Sinha, S.K., et al. Time-frequency attribute of seismic data using continuous wavelet transform. in 2003 SEG Annual Meeting. 2003. Society of Exploration Geophysicists.

